This chapter embellishes the characterization of prepared materials, their efficiency evaluation and interpretation in arsenic remediation and comparison of their efficiency with previously reported method. Keeping an eye on the main objectives of the thesis, three bio based polymeric systems viz. chitosan, starch and E. crassipes root powder were chosen for the whole study. Availability of raw materials, their cost, biocompatibility and biodegradability, etc. were the major important issues for this choice. On the other hand, while choosing the nanomaterials, along with their efficiency and reusability, special focus was given to their toxicity/biocompatibility. For systematic study the chapter is subdivided into three major sections. This division was done on the basis of the pristine polymeric material taken for the study. In section A, the findings obtained for chitosan bio polymer based materials were considered. Magnetic iron oxide particles and MMT clay were stabilized over chitosan biopolymer for stabilization and enhanced sorption. Section B deals with the immobilization of highly efficient arsenic adsorber viz. $TiO_2$ and iron oxyhydroxide/clay over cheap starch biopolymer. In section C, unused, widely abandoned water hyacinth root powder based materials are successfully utilized for arsenic sorption. Each of these prepared materials has their own advantages of good efficiency for arsenic sorption, easy separation (for magnetic particles), reusability, cost effectiveness (WHRP is associated with zero cost) etc. the findings of the studies are systematically described as-

**Section A: Chitosan Based Composite in Arsenic Remediation**

Chitosan represents an excellent biopolymer which can be employed as adsorbents for successful remediation of arsenic from water. It is largely available in nature, bio-compatible, non-toxic and bio-degradable as compared to the synthetic polymers due to the presence of chemically reactive functional groups such as hydroxyl, acetamido, amino etc., which makes chitosan an edge over others [1, 2]. Besides the sorption ability, this biopolymer can be used in the stabilization of several nanomaterials; the later are excellent scavenger of water contaminants including arsenic. Many reports are available pertaining to the use of chitosan either alone or in combination with other materials for adsorption of heavy metal ions or other contaminants from water [3]. In this section, two different types of composite materials of montmorillonite clay and magnetic iron particles were prepared using chitosan bio polymer and their efficacy in arsenic adsorption were studied.

## 3.1 Comparative Study on Sorption of Arsenate Ions from Water by Crosslinked Chitosan and Crosslinked Chitosan/MMT Nanocomposite

Natural clay minerals are abundantly available low-cost material which are nontoxic to ecosystem and show good sorption efficiency in the purification of water. Use of MMT, organoclay etc. in different nanocomposites for effective removal of different dye material is well explored [4, 5]. These clay minerals in their normal or modified form can be successfully utilized in the sorption of different forms of arsenic and heavy metals from water [6, 7]. But its separation after water treatment may be quite expensive and difficult to perform. Some turbidity may be developed if clay is used alone in the treatment of water. This limits its acceptability in drinking water.

Delamination of clay in presence of polymer matrix followed by stabilization with crosslinking agent may enhance its uses over a broad chemical environment. Arida et al. has investigated the removal of As(V) from groundwater using Chitosan coated bentonite clay [8]. These materials can play a vital role in improving synergistically the properties of the composites. The present work aims to develop a suitable nanocomposite of chitosan with MMT clay mineral and study its efficacy for removal of As(V) contaminants from water.

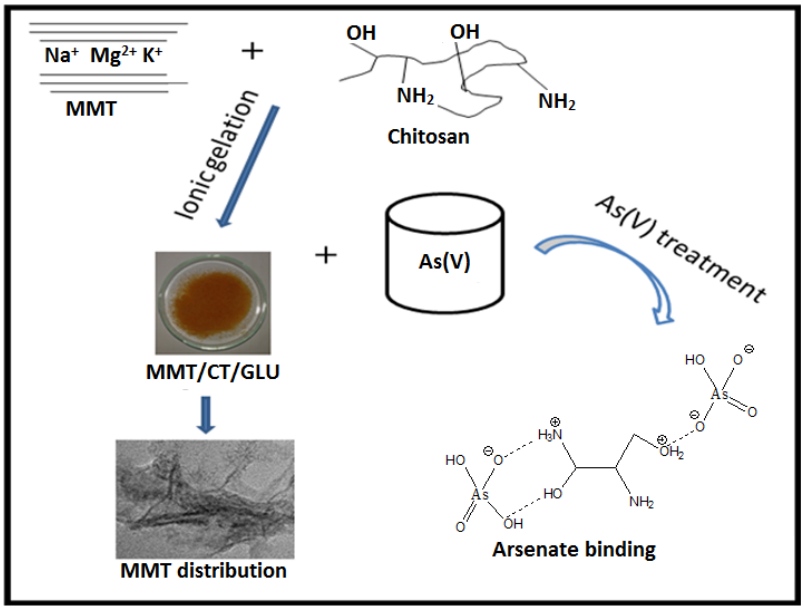


**Scheme 3.1.1** Schematic representation of chitosan-MMT nanocomposite and its binding with As (V)

## *3.1.1 Results and Discussion*

### *3.1.1.1 Characterization*

#### *3.1.1.1.1 FT-IR Analysis*

FT-IR study was done to verify different interactions among the component materials during the preparation of nanocomposite and to predict the binding of arsenic with it. Figure 3.1.1 represents the FTIR spectra for chitosan (curve-a), MMT (curve-b), Ct/Glu (curve-c) and MMT/Ct/Glu curve-d). FT-IR spectrum of CT showed absorption bands at 3430 $cm^{-1}$ (–OH stretching), 2925 $cm^{-1}$(–$CH_2$ stretching), 1650 (amide-I band), 1412 (C-H bending), 1086 (C-N stretching corresponding to ammine). These data were in accordance with the data obtained from literature [9]. MMT was characterized by the presence of bands at 3438 $cm^{-1}$ for –OH stretching, 1642 $cm^{-1}$ for –OH bending, 1035 $cm^{-1}$, 530 $cm^{-1}$ and 470 $cm^{-1}$ for oxide band of metals (Al, Mg, Si, etc.) [8, 10]. From the spectrum of Ct/Glu, it was observed that the band assigned for –OH stretching was broadened.

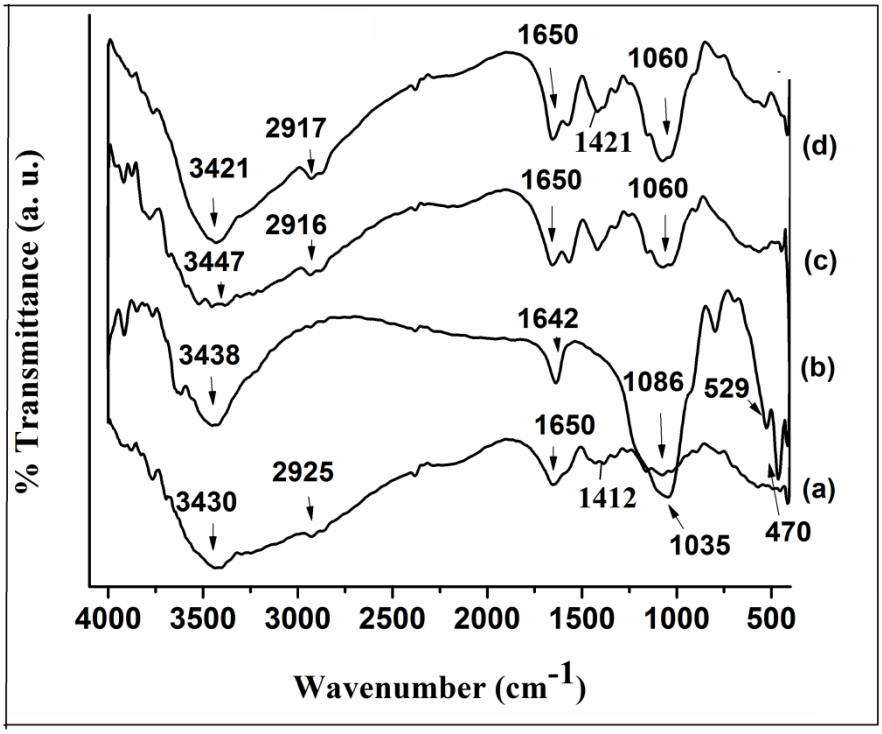


**Figure 3.1.1** FT-IR spectra of (a) CT, (b) MMT, (c) Ct/Glu and (d) MMT/Ct/Glu

This may be due to the involvement of the hydroxyl groups in crosslinking with glutaraldehyde. However, in MMT/Ct/Glu the peak intensities of –OH stretching and

metal oxide bands were increased. The increase in peak intensity as mentioned above might be due to incorporation of clay in to the system. Another important band near 2925 $cm^{-1}$ in the polymer, characteristic of $-NH_3^+$ overlap with –CH stretching (2917 $cm^{-1}$) , showed a red shift in both the cases. Intensity of the band appearing at 1412 $cm^{-1}$ (in polymer) was also found to increase. The intensity further increased after incorporation of clay in to the system. Moreover, the peak intensity at 1086 $cm^{-1}$ enhanced compared to that of Ct/Glu suggesting interaction of clay with polymer.

Figure 3.1.2 shows FT-IR spectra of MMT/Ct/Glu and As(V) adsorbed MMT/Ct/Glu. From the figure, it was observed that the bands at 3421 $cm^{-1}$, 1650 $cm^{-1}$, 1060 $cm^{-1}$ of the MMT/Ct/Glu became sharp after treatment with As(V) solution. Along with an increase in intensity, the band at 1060 $cm^{-1}$ also showed a red shift to 1123 $cm^{-1}$ when treated with As(V) solution. Existence of characteristic band near 618 $cm^{-1}$ may be due to As-O asymmetric vibrations [11, 12]. All these changes in FTIR band indicated the chemical interaction of the metal ion with the nanocomposite.

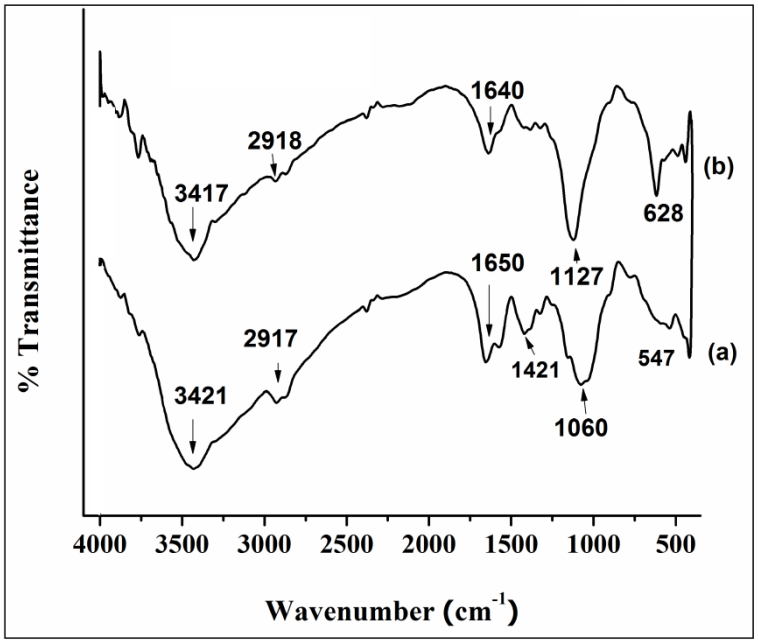


**Figure 3.1.2** FT-IR spectra of MMT/Ct/Glu (a) before & (b) after adsorption of As(V)

*3.1.1.1.2 X-Ray Diffractometeric Analysis*

The XRD patterns of MMT (curve-a), CT (curve-b), Ct/Glu (curve-c) and MMT/Ct/Glu (curve-d) are shown in Figure 3.1.3. It was observed that the XRD

pattern of the MMT showed peaks near 2θ=9.1° and 26.8 (curve-a) corresponding to basal spacing's of 10.39A° and 3.13 A°, respectively [13, 14]. The XRD pattern of CT showed the characteristic peaks at 2θ =10° and 20.13°, respectively, which corresponds to the literature data (curve-b) [15]. XRD pattern of the Ct/Glu (curve-c) showed that intensities of the peaks present in the pristine polymer significantly reduced and shifted slightly towards the lower angle. This might be an indication of structural changes (change in crystallinity) occurred in chitosan due to cross linking by glutaraldehyde. CT has a large number of hydroxyl functional groups and also its cationic structure in acidic medium may facilitate good miscibility with MMT. Hence, it could easily intercalate inside the silicate layers by cationic exchange. It is reflected in the XRD spectrum of MMT/Ct/Glu (curve-d). In this case, the intensity of the characteristic peaks for CT appearing approximately at 2θ=10° and 20°, decreased as well as shifted compared to those of Ct/Glu. Moreover, the crystal diffraction peak of clay (2θ=9.1°) almost disappeared in MMT/Ct/Glu. The reduced peak intensities as compared to the pristine polymer and MMT indicated decrease in crystallinity in the MMT/Ct/Glu. This suggested a partial delamination of polymer intercalated clay layers.

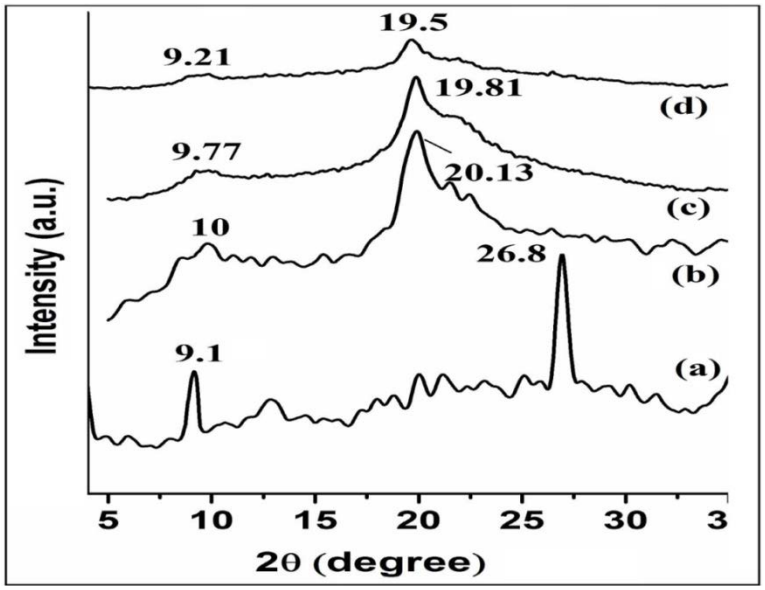


**Figure 3.1.3** XRD spectra of (a) MMT (b) CT (c) Ct/Glu & (d) MMT/Ct/Glu

*3.1.1.1.3 Transmission Electron Microscopy (TEM) Study*

Figure 3.1.4 (a-c) shows the TEM images of Ct/Glu (a), MMT/Ct/Glu, respectively. Micrograph (a) appeared smooth and there were no any foreign materials

present in the MMT free crosslinked polymer. After loading MMT clay into the material Figure 3.14 b) & c), random distribution of layered silicate structures in the form of dark lines were appeared. Micrograph b) and c) represented the images of MMT clay loaded crosslinked polymer at two different magnifications. The dark lines reflected the well delaminated clay layers which were stabilized within crosslinked polymer matrix. These results supported the finding obtained from XRD study.

*3.1.1.1.4 Scanning Electron Microscopy (SEM) Study*

SEM images of MMT/Ct/Glu before and after As (V) adsorption are shown in Figure 3.1.4. From the micrographs it was seen that MMT/Ct/Glu had an agglomerated structure and the surface roughness was prominent. Kousalya et al. [11] studied the morphological changes of the modified chitosan beads before and after chromium adsorption. They concluded that morphological changes occurring at the surface as an indication of sorption of chromium ion on the surface. In present study, also, clear morphological changes were observed after adsorption of As(V) on MMT/Ct/Glu. The irregularity on surface decreased little bit after sorption of As(V).

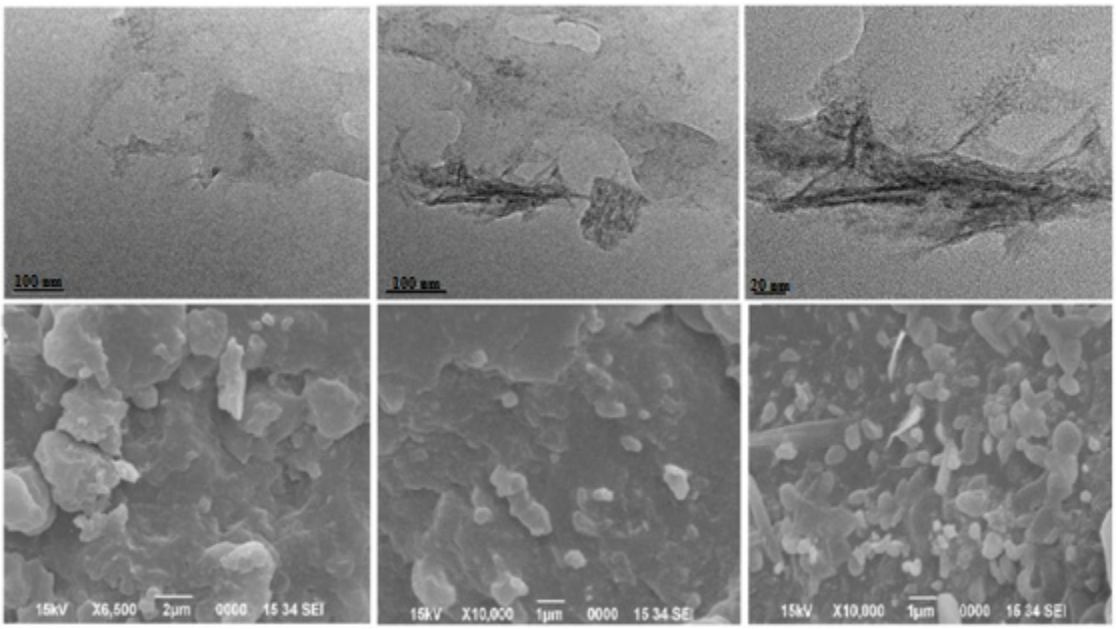


**Figure 3.1.4** TEM images (a) of Ct/Glu and (b, c) MMT/Ct/Glu and SEM images of MMT/Ct/Glu (d-e) before and (f) after arsenic adsorption

TEM images of chitosan clay nanocomposite clearly confirmed the nanosize distribution of clay layers within the polymer matrix. It is being a composite; hence no

further size analysis was carried out. Also, good interactions among the components were well predicted by FT-IR, XRD and TEM collectively. Hence TGA was not performed

### *3.1.1.2 Batch Adsorption Experiment for As(V)*

#### *3.1.1.2.1 Effect of Material Dose*

Figure 3.1.5 (A) shows the effect of material dose on removal rate (%) of As(V). at a fixed initial As(V) concentration of 0.4 mg/L. The adsorption study was carried out using different doses of the two materials (viz. Ct/Glu and MMT/Ct/Glu) ranging from 0.25 to 3 g/L. It was found that for MMT/Ct/Glu, a dose of 2 g/L of solution was sufficient for bringing down As(V) concentration below 0.01mg/L. For Ct/Glu system, the optimum dose was found to lie in the range of 2-2.5 g/L of solution. Better removal in the former case was due to participation of MMT in arsenate binding process.

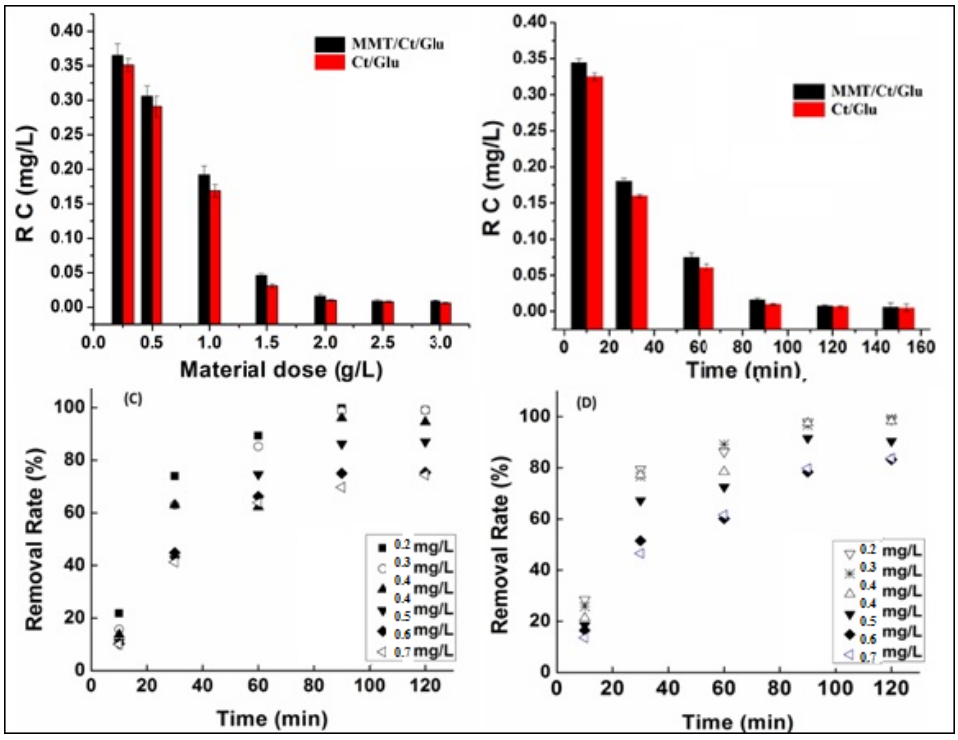


**Figure 3.1.5** Effect of (A) material dose, (B) Treatment time and (C), (D) initial ion concentration on removal rate of As(V) [R C: residual concentration]

It was also observed that the removal rate increased up to certain adsorbent dose beyond that no significant improvement was observed. As sorption being an equilibrium process, the discrepancy in behavior was due to non availability of sufficient arsenate ions in solution to bind with the increasing active sites upon increasing the sorbent dose.

*3.1.1.2.2 Effect of Contact Time on As(V) Removal*

Figure 3.1.5 (B) shows the variation of removal rate (%) of As(V) with time for MMT/Ct/Glu and Ct/Glu. In order to study the effect of time and clay content, the concentration of As(V) solution and material dose were kept fixed at 0.4 mg/L and 2 g/L respectively. A significant improvement in As(V) adsorption was obtained due to the loading of clay. This improvement in removal rate may be due to high sorption capability, ability to expand and ion exchange property of the clay. Sorption of different oxyanions of arsenic along with oxyanions of Se on MMT and Kaolinite clay has been represented/compared by Frost et al. Different mechanisms of sorption due to ion exchange were cited in this study assuming that the anion exchange sites were initially occupied by some anions such as $OH^-$ [16]. Usuki et al have presented a quantitative approach of ability of Na-MMT clay for exchanging ammonium cations of different ε-amino acids. They have also studied the spacing of clay layers with the help XRD analysis, before and after cation exchange and reported an increase in interlaminar spicing, after ion exchange [17]. In the removal rate (%) vs time curve, it was found that removal rate increased initially with the increase in contact time up to 90 min, beyond that the curve almost leveled off. This might be due to the establishment of equilibrium between the active sites on material surface and arsenate ions from the aqueous phase. Pandey and Mishra explained the sorption of Cr(VI) onto Organic–inorganic hybrid of chitosan/organoclay bionanocomposites [18].

*3.1.1.2.3 Effect of Initial Ion Concentration*

The effect of initial ion concentration on removal rate (%) of As(V) was studied in the concentration range of 0.2-0.7 mg/L. The agitation time and material dose were kept fixed as optimized earlier. Figure 3.1.5 [(C), (D)] shows the variation of removal rate (%) of As(V) with change in initial As(V) concentration for Ct/Glu and MMT/Ct/Glu, respectively. In both the cases, the percent removal of As(V) decreased with the increase in initial metal ion concentrations. This may be due to the delayed establishment of equilibrium. Moreover, at higher concentrations, the numbers of active sites on the adsorbent material were not sufficient to bind all the arsenate ions due to saturation of adsorption sites on the material. As the amount of material is same for all the concentrations under interest, hence number of active sites is also fixed. Thus, with increase in concentration, the binding sites got saturated and no longer remain available to adsorb more arsenate ions. But the arsenate uptake capacity of the adsorbent (mg/g) increased. The increase in uptake capacity with the increase in initial ion concentration

might be due to the increase in concentration gradient of arsenate ions between the adsorbent and that in solution. Also, MMT/Ct/Glu system exhibited higher removal rate (%) due to the presence of clay.

*3.1.1.1.2.4 Effect of pH on As (V) Removal*

Batch tests were carried out for MMT/Ct/Glu under different pH conditions {(Figure 3.1.6 (A)}. The point of zero charge (pzc) for MMT/Ct/Glu (~6.5) was determined from Figure 3.1.6 (B). Thus, below pH=6.5, the material undergoes protonation in solution, hence, increases the removal rate of arsenate ions. Also arsenate ions exist in different oxidation states viz. $H_3AsO_4$, $H_2AsO_4^-$, $HAsO_4^{2-}$ and $AsO_4^{3-}$ at different pH conditions of 2.0, 2.0-7.0, 7.0-12.0, and ›12.0, respectively [19]. At lower pH, AlOH groups, arise due to the rupture of clay edge, might get protonated and thus improving the binding of arsenate. The maximum removal rate was observed at pH~3-4. Below that pH, the material loosed its stability and swelled.

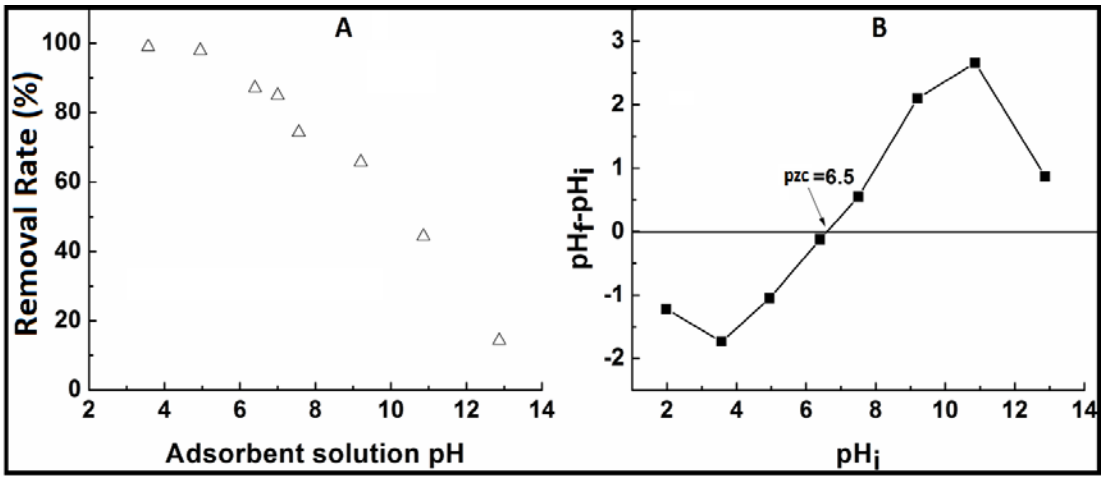


**Figure 3.1.6** Effect of (A) pH on percent removal of As(V), (B) Zero point charge curve

*3.1.1.2.5 Mechanism of Arsenic Binding*

Above discussion showed that the arsenic binding process by MMT/Ct/Glu mainly involved electrostatic interaction between arsenate ions and active sites on the material. Moreover, pKa values of arsenic acid ($H_3AsO_4$ are $pK_1$=2.20, $pK_2$=6.97, and $pK_3$=11.53) also showed the favorability of arsenate sorption in the range 5.5-7.5 which is also in support of the electrostatic type interaction between the sorbent and arsenate ions [20]. A probable mechanism of binding of As(V) is schematically shown below

(scheme 3.1.2). The major components of MMT clay were oxides of Si and Al along with Fe, Mg and Ca ions replacing some of the Al atoms in octahedral Sheet [21]. Ions of Ca, Na and K were also present in between the clay layers as exchangeable cations. The major adsorption of arsenate on MMT/Ct/Glu, might take place through the $NH_2$ groups on MMT/Ct/Glu, Lewis acid sites viz. $Al^{3+}$ and $AlOH_2^+$, which arised due to the rupture of edge over Si-O-Al bonds in clay. Li and Bowman mentioned the sorption of $CrO_4^{2-}$ ions on to clay minerals through the $AlOH_2^+$ groups [18]. Bhattacharyya and Gupta reported the $Al^{3+}$ sites as anion binding groups in clay minerals. They also mentioned that the $H^+$ ions present at the surface of clay were also responsible for arsenate binding [7]. These $H^+$ ions formed due to the complexation of the exchangeable cations with water as shown by the following equation-

$$[M(H_2O)x]^{n+} \longrightarrow [M(OH)(H_2O)_{x-1}]^{(n-1)+} + H^+ \quad (1)$$

Some amount of hydrogen bonding and also iron (not shown in scheme) which were present due to the isomorphic substitution of Al from octahedral sites may contribute to the arsenate binding process [22].

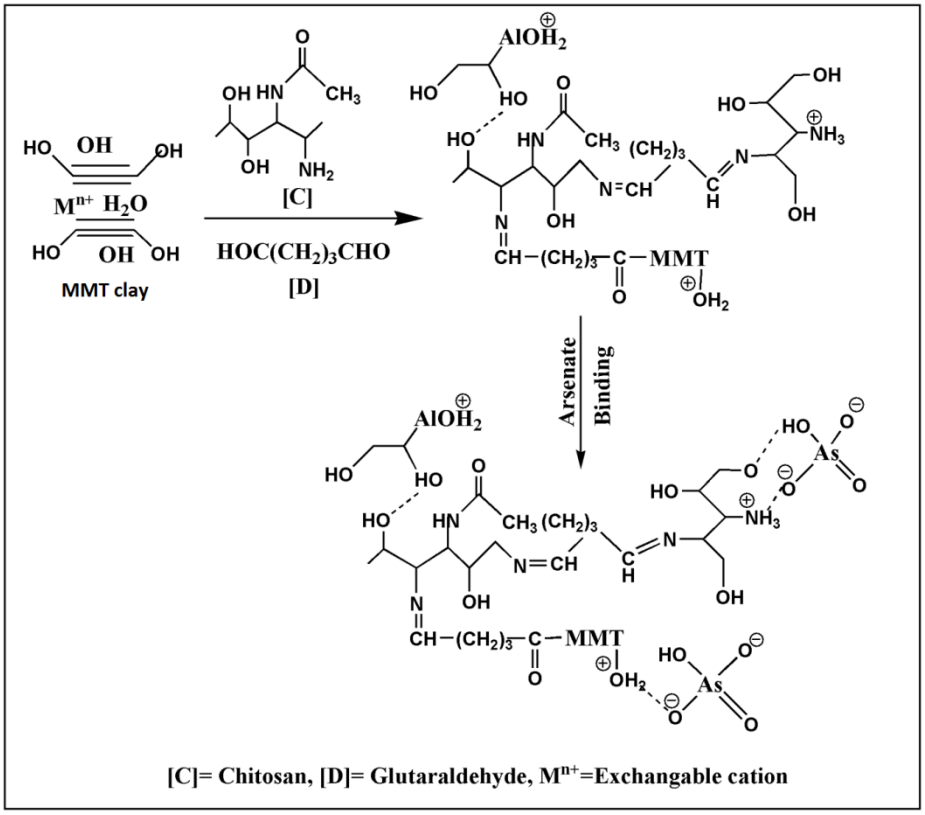


**Scheme 3.1.2** Possible binding mechanism of MMT/Ct/Glu with arsenate ions

### *3.1.1.3 Adsorption Isotherm Study*

The isotherm study was performed at equilibrium time i.e. 90 min, with six different initial concentrations of As(V) from 0.2 to 0.7 mg/L for a material dose of 2.0 g/L. Langmuir and Freundlich models were applied to investigate the sorption pattern and different constants were generated. The linear plots of $1/Q_e$ vs. $1/C_e$ showed that adsorption followed the Langmuir isotherm model [Figure 3.1.7 (A) & (B)]. The correlation coefficients were found to be 0.979 and 0.972 Ct/Glu and MMT/Ct/Glu, respectively. $Q_o$ and 'b' were determined from the slope and intercept of the plot. From Table 3.1.1, it was found that the sorption was favorable for both the material as $R_L$ values occurred between 0 and 1 for each case.

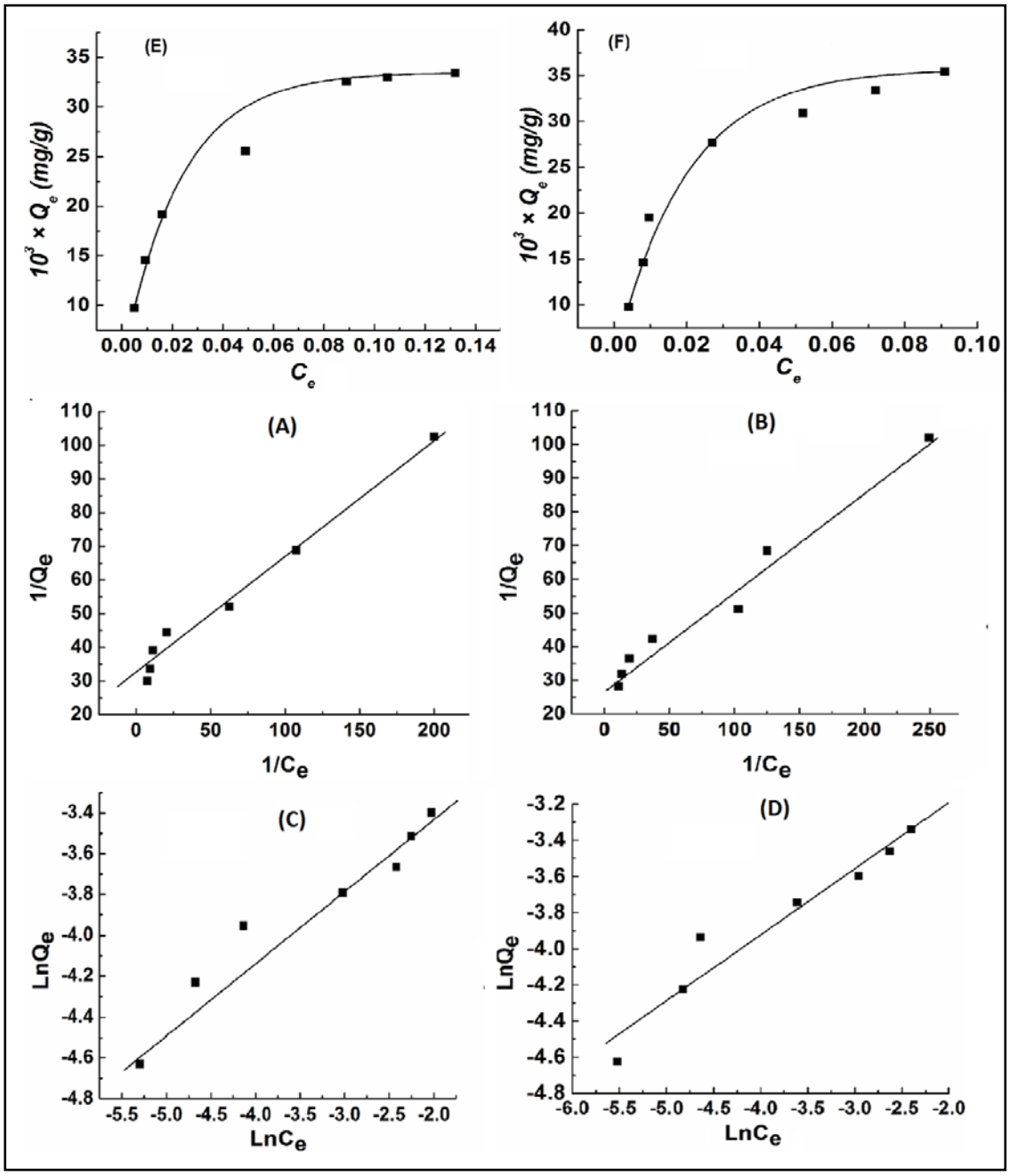


**Figure 3.1.7** Langmuir isotherm for (A) Ct/Glu & (B) MMT/Ct/Glu, Freundlich isotherm for (C) Ct/Glu & (D) MMT/Ct/Glu and $Q_e$ vs $C_e$ graph for (E) Ct/Glu & (F) MMT/Ct/Glu

A linear plot of ln$Q_e$ vs ln$C_e$ is drawn {Figure 3.1.7 (A) & (B)}. From the slope and the intercept of the graph, the adsorption capacity and Freundlich constant were obtained. $R^2$ value showed the fitting of the data obtained with the isotherm.

**Table 3.1.1** Isotherm parameters for Ct/Glu and MMT/Ct/Glu for different models

| Isotherm model | Parameters | Ct/Glu | MMT/Ct/Glu |
|---|---|---|---|
| Langmuir | $Q_o$ (mg/g) | 2.855 | 3.403 |
| | B | 0.0109 | 0.0105 |
| | $R_L$ | 0.996 | 0.995 |
| | $R^2$ | 0.979 | 0.972 |
| Freundlich | $k_f$ (mg/g) | 0.0615 | 0.085 |
| | N | 3.106 | 2.752 |
| | $R^2$ | 0.932 | 0.927 |

Table 3.1.1 shows the isotherm parameters for Langmuir and Freundlich models obtained at room temperature. It was observed that the $R^2$ values for both Langmuir and Freundlich isotherms showed good co-relations of the data. Thus, the sorption could be reasonably explained with both the isotherms. It is a situation when both Langmuir and Freundlich isotherms adequately describe the same set of liquid-solid adsorption data at certain concentration ranges, in particular if the concentration is small. This happens when the adsorption capacity of the solid is large enough to make both isotherm equations approach a linear form.

However, Langmuir isotherm showed better fitting ($R^2$=0.979 & 0.973) as compared to Freundlich ($R^2$=0.937 & 0.927). These information implied that a monolayer chemisorption pattern of As(V) on adsorbent surface was preferred.

**Table 3.1.2** Comparison of efficiency with other reported adsorbent

| **Material** | **Arsenic species** | ***Q<sub>o</sub>* (mg/g)** | **Remark** |
|---|---|---|---|
| MMT | As(V) | 0.64 | Desorption percent is very less |
| Illite | | 0.86 | |
| Kaolinite | | 0.52 | |
| Ct/Glu | As(V) | 2.855 | Easy processing, reclyable |
| MMT/Ct/Glu | As(V) | 3.403 | |
| CTAB-MMT | As(III) | 46.25 | Reusability was lacking |

A comparison of the efficiency ($Q_o$) of Ct/Glu and MMT/Ct/Glu was made with some other reported adsorbents of similar kind [23] as shown in Table 3.1.2. Different

clay as presented in the table has been reported to show good sorption ability. Mobilization of adsorbed arsenic from those materials were also studied and found that very less percent of arsenic got desorbed from the material. Thus, efficiency might decrease in consecutive regeneration cycle. Anjum et al. demanded many fold increase in sorption capacity of MMT clay on modification with CTAB and also lesser time establishment of equilibrium. But in this case also reusability experiment was lacking and also very high concentration of arsenic was taken [24]. Material under present investigation showed sufficiently good results and cyclic run was also successfully carried out for several times.

#### *3.1.1.4 Adsorption Kinetics*

Kinetic study on the basis of sorption data was carried out to understand the mechanism of sorption. The experimental conditions were kept similar to that of isotherm study.

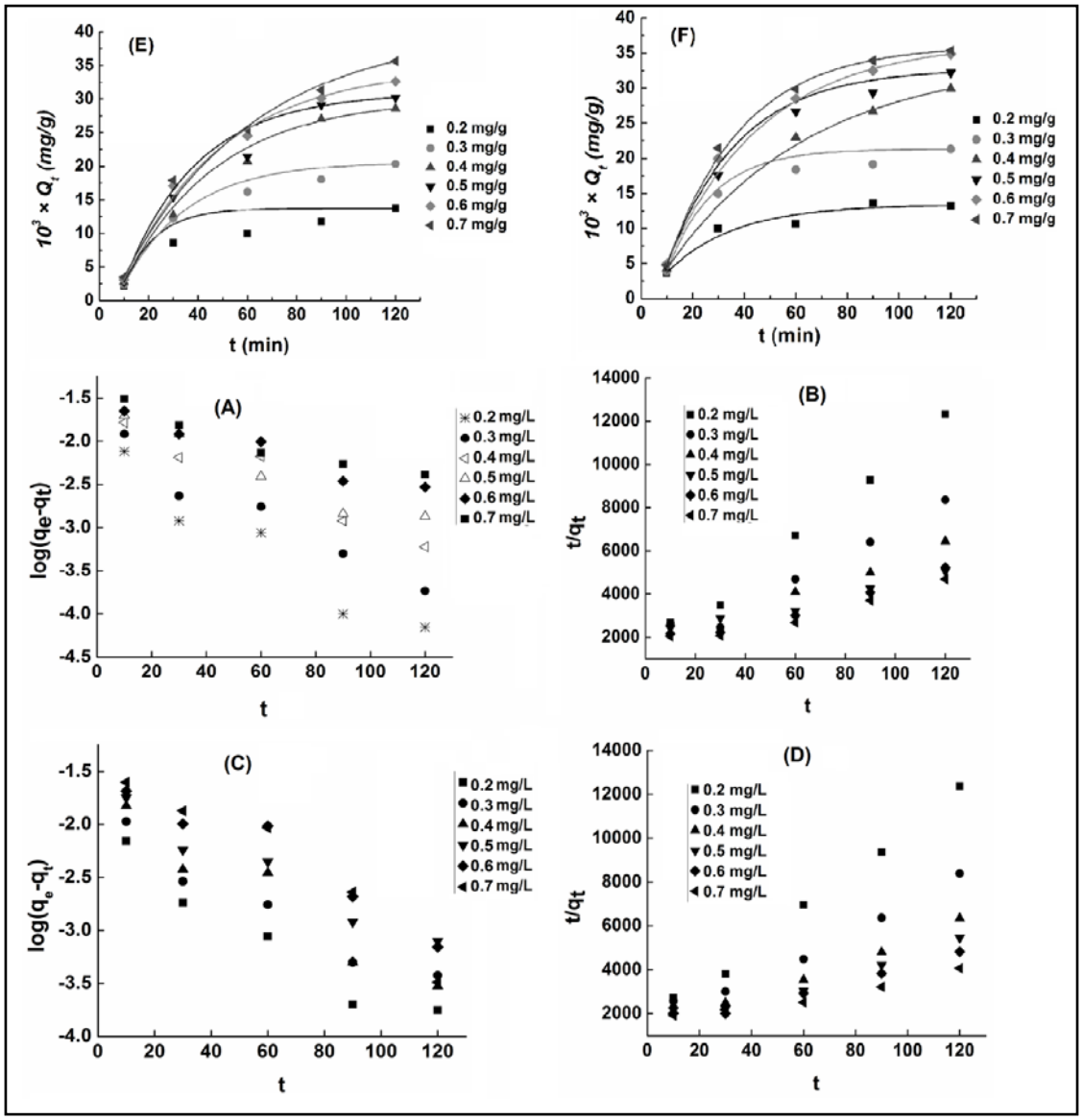


**Figure 3.1.8** First order kinetics for **(A)** Ct/Glu & **(C)** MMT/Ct/Glu, second order kinetics for **(B)** Ct/Glu & **(D)** MMT/Ct/Glu and time evolution of $Q_t$ for (E) Ct/Glu & (F) MMT/Ct/Glu

The values of different kinetic parameters viz. first order and second order were determined from the corresponding curves as shown in Figure 3.1.8 and presented in table 3.1.3 and table 3.1.4, respectively. The $q_e$ values were found to increase with the increase in the initial As(V) concentrations.

**Table 3.1.3** First order kinetic parameters for Ct/Glu and MMT/Ct/Glu

| $C_o$ (mg/ L) | Kinetic parameters | | | | | |
|---|---|---|---|---|---|---|
| | MMT/Ct/Glu | | | Ct/Glu | | |
| | $q_e$ | $K_{ad}$ X $10^2$ | $R^2$ | $q_e$ | $K_{ad}$ X $10^2$ | $R^2$ |
| 0.2 | 0.114 | 3.37 | 0.913 | 0.119 | 4.19 | 0.903 |
| 0.3 | 0.136 | 2.97 | 0.922 | 0.146 | 3.49 | 0.933 |
| 0.4 | 0.171 | 3.49 | 0.910 | 0.190 | 2.97 | 0.909 |
| 0.5 | 0.177 | 2.76 | 0.933 | 0.196 | 2.66 | 0.925 |
| 0.6 | 0.223 | 2.99 | 0.912 | 0.201 | 1.89 | 0.923 |
| 0.7 | 0.269 | 3.76 | 0.907 | 0.214 | 1.78 | 0.902 |

The curve for pseudo second order kinetic model exhibited higher correlation co-efficient compared to pseudo first order kinetic model. Moreover, the experimental $q_e$ values were found to be more closure to the $q_e$ values calculated from second order kinetics. The sorption was predominantly explained by a second order kinetics.

**Table 3.1.4** Second order kinetic parameters for Ct/Glu and MMT/Ct/Glu

| $C_o$ (mg /L) | Kinetic parameters | | | | | | | |
|---|---|---|---|---|---|---|---|---|
| | MMT/Ct/Glu | | | | Ct/Glu | | | |
| | $h$ X $10^4$ | $q_e$ | $K$ | $R^2$ | $h$ X $10^4$ | $q_e$ | $K$ | $R^2$ |
| 0.2 | 6.61 | 0.011 | 5.26 | 0.993 | 7.63 | 0.011 | 1.135 | 0.988 |
| 0.3 | 6.15 | 0.018 | 1.79 | 0.973 | 6.78 | 0.018 | 0.158 | 0.950 |
| 0.4 | 62.4 | 0.027 | 0.87 | 0.957 | 5.61 | 0.027 | 0.105 | 0.936 |
| 0.5 | 6.67 | 0.032 | 0.64 | 0.944 | 4.76 | 0.042 | 0.043 | 0.964 |
| 0.6 | 6.88 | 0.037 | 0.49 | 0.956 | 6.41 | 0.035 | 0.052 | 0.946 |
| 0.7 | 6.27 | 0.052 | 0.23 | 0.949 | 6.75 | 0.039 | 0.084 | 0.935 |

### *3.1.1.5 Reusability Experiment*

The reusability experiment was carried out for four consecutive cyclic runs. The materials used for the treatment with arsenate water, were separated after each cyclic

run and desorption was done with 0.05 M HCl. Figure 3.1.9 shows the percent loss of material and removal rate after each cyclic run.

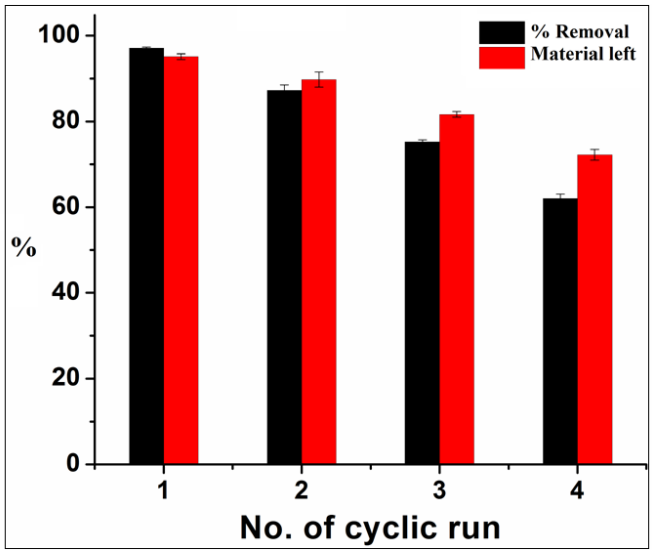


**Figure 3.1.9** Reusability after cyclic run of MMT/Ct/Glu (Arsenate concentration: 0.4 mg/L)

From the figure, it was clear that after each cyclic run some amount of material got lost. This might be due to loss of surface integrity of the coated polymeric material upon treatment with acid. Again after each cyclic run, the removal rate of arsenate ions decreased and this decrease in removal rate was more prominent after more number of cyclic runs. The decrease in removal rate could be attributed to the partial desorption of arsenate ions from the adsorbent surface by HCl and also due to the loss in integrity of the material on acid treatment.

## 3.2 Adsorption of As(V) From Contaminated Water over Chitosan Coated Magnetite Composite: Equilibrium and Kinetics Study

This part of the study focused on the evaluation of efficacy of a composite of chitosan and magnetite nanoparticles for remediation of pentavalent arsenic from water and tests its long term usability.

Iron based nanoparticles are excellent adosorber of arsenic and other metal contaminants. Iron can act as an efficient material for arsenic remediation in its different oxidation states such as zero valent iron, iron oxide hydroxide, magnetite, maghemite, etc. [25, 26]. Out of these different states, magnetic nanoparticles can be employed as a convenient tool to explore magnetic separation techniques due to its specific magnetic characteristics. But magnetite particles are very much sensitive to air oxidation and readily get oxidised to other oxides of iron and also aggregated in aqueous system. The different oxides of iron like hematite, goethite, etc. are reported to have lower sorption ability than magnetite [27]. Therefore, it is necessary to modify surface of the nanoparticles for better selectivity, aqueous stability, and prevention of leaching and reusability as these are the most important concerns for using these materials effectively in water treatment process [28]. It can be tailored by using some polymeric materials or other supports. Chitosan bio polymer is a good choice in this purpose due to the large number of functional groups present in it. In many literatures, chitosan has been cited as polymeric material to coat nanomaterials used for water treatment, where the former also took part in sorption [8, 29].

Present study aimed to modify the surface of magnetite particles by chitosan polymer for effective use in As(V) removal and also for a long term usability. The study also aims at comparing removal efficiency with some of the established material. The effect of several competition ions on the removal efficiency has also been focused in this experiment.

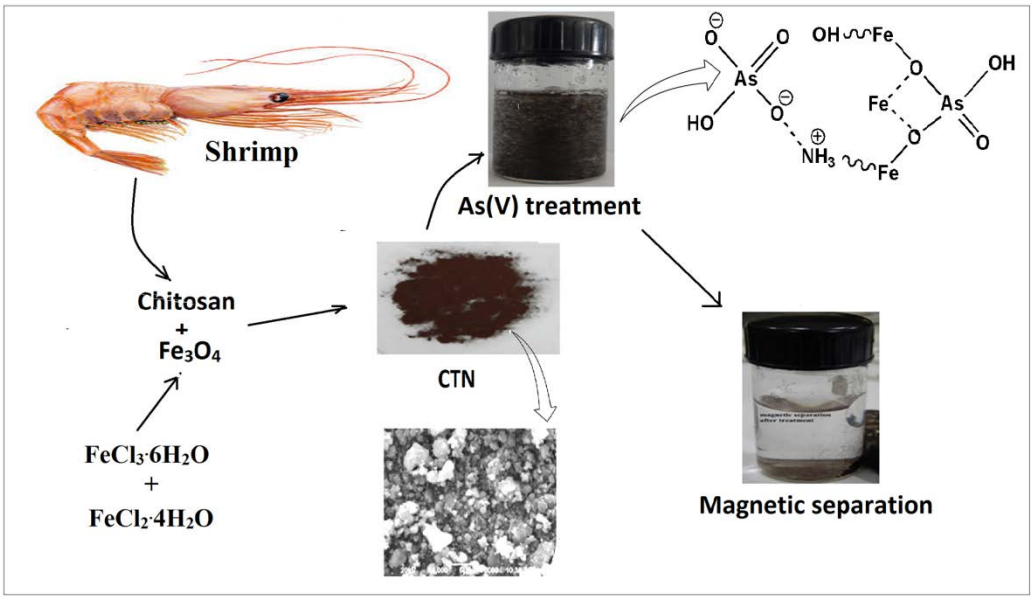


**Scheme 3.2.1** Ex-situ preparation of $Fe_3O_4$ magnetic particles and stabilization over chitosan

### 3.2.1 Results and Discussion

#### *3.2.1.1 Characterization*

*3.2.1.1.1* FT-IR Analysis

Figure 3.2.1(A) shows the FT-IR spectra of CT, bare FeN particles and CTN. Chitosan polymer (curve c) was characterized by the absorption bands appearing near 3350-3450 $cm^{-1}$ (-NH stretching), 2359 $cm^{-1}$ (–$CH_2$ stretching), 1650 $cm^{-1}$ (amide I band), 1406 $cm^{-1}$ (C-H bending) and 1059 $cm^{-1}$ (C-N stretching corresponding to amine) [30]. In the spectrum for FeN (curve b), three characteristics bands appeared at 574, 1622 and 3409 $cm^{-1}$. The band at 574 $cm^{-1}$ resembles the vibration of the Fe-O bonds in the crystalline lattice of $Fe_3O_4$ as reported by Akin et al. [31]. Bands at 1622 and 3409 $cm^{-1}$ might be due to the hydroxyl groups which were accumulated on the surface of the nanoparticles during the preparation of FeN by the chemical co-precipitation method. In the spectrum of CTN (curve a), the presence of FeN core could be identified by the strong stretching absorption band at 550 $cm^{-1}$, which corresponded to the Fe–O bond. The absorption band appeared in the 550 $cm^{-1}$ region suggested the formation of FeN particles. Presence of band around 1545 $cm^{-1}$, assigned to the -$NH_2$

group bend scissoring, in CTN spectrum confirmed the successful coating of magnetite particles by chitosan polymer [32].

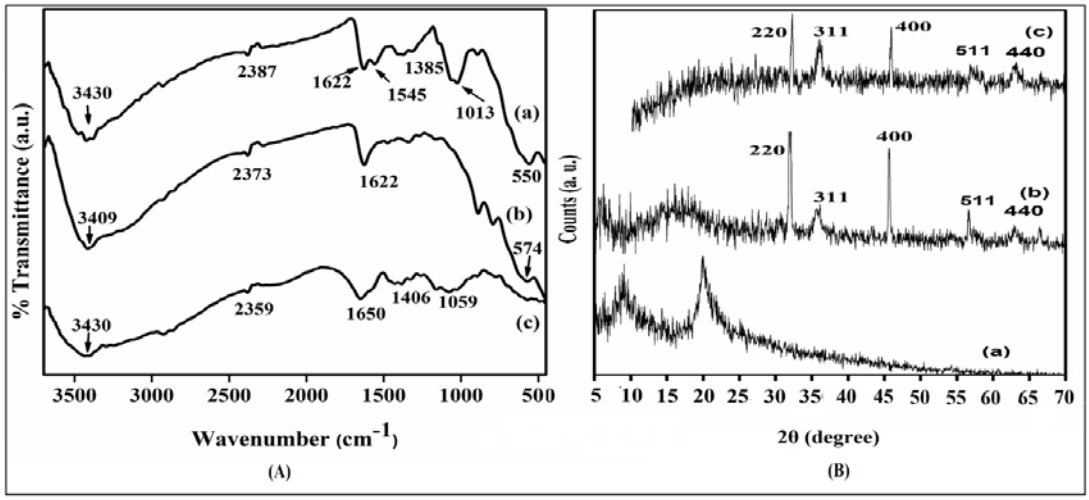


**Figure 3.2.1** (A) FT-IR spectra of (a) CTN, (b) FeN and (c) CT and (B) XRD spectra of (a) CT, (b) FeN and (c) CTN

*3.2.1.1.2 X-Ray Diffraction (XRD) Study*

Crystal structures of chitosan, FeN and CTN were studied using XRD. The diffractograms are shown in Figure 3.2.1(B). The XRD spectrum of chitosan shows peaks with low intensity values around 2θ = 9° and a broad peak at around 2θ= 20°. Similar results were reported by Ming-chun et al. and Lu et al. Diffraction peaks appeared at 2θ of 32°, 36°, 45°, 57° and 63.5° due to their corresponding indices (220), (311), (400), (511) and (440), were observed in FeN particles [33, 34]. These were the characteristic peaks of the magnetite ($Fe_3O_4$) crystal having an inverse cubic spinel structure [30]. In the diffractogram of CTN, the peak positions assigned for FeN crystals remained unchanged. This suggested that the chitosan binding process did not result in the phase change of FeN. The disappearance of the peaks at 2θ=9° and 20° was due to decrease in crystallinity of the chitosan polymer on incorporation of iron particles into it. The iron particles are well dispersed in between the polymeric chain resulting into decrease in crystallinity of the polymer and hence the peaks in the XRD spectrum disappeared.

*3.2.1.1.3 TGA Analysis*

The thermograms for Chitosan (CT), bare FeN and CTN are shown in Figure 3.2.2 (A). All the three samples exhibit their own distinctive TGA curves. The initial weight loss observed in all the samples at around 100 °C was due to the evaporation of the small amount of moisture present in the samples. The TGA curve for Chitosan (curve a) showed the highest weight loss in the temperature range ~250 °C - 320 °C; whereas, the bare FeN particles had hardly shown (curve c) any weight loss in that region, except the initial loss of water. Chitosan coated $Fe_3O_4$ (curve b) showed less weight loss compared to bare chitosan [31]. It may be due to the increasing stability of chitosan achieved through interaction with FeN. Moreover, since no two separate degradation patterns were observed for the TGA curve of CTN particles, it indicated that the mixing of chitosan and FeN did not form a blend. Rather, chitosan properly interacted with FeN particles.

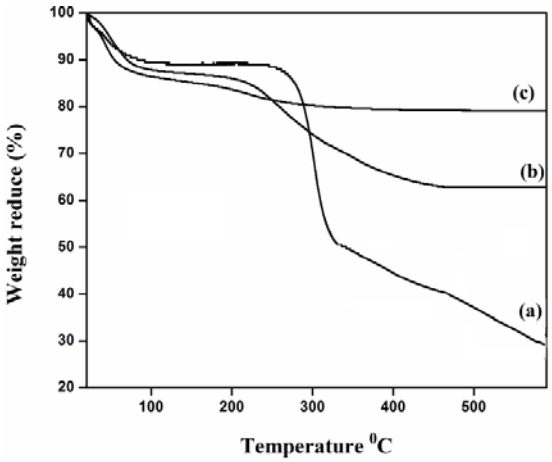


**Figure 3.2.2** (A) Thermal degradation pattern of (a) CT, (b) CTN, (c) FeN,

There was no significant weight loss for FeN particles from 100 °C to 600 °C. For the CTN, the weight loss in the range 220–400 °C was mainly due to degradation of cross-linked chitosan component present in the CTN. Appearance of intergradation in the range of 374-458 ºC in TGA thermogram could be attributed to the presence of chitin content in the partially deacetylated chitosan polymer. Degradation observed in the above range was due to presence of chitin fraction in the biopolymer. Kim et al. [35] characterized chitin biopolymer by TGA analysis and observed similar degradation pattern starting from 250 ºC which leveled off near 400 ºC. Further,

increase in polymer amount caused loss in magnetic properties of the material. A percent loading of approx. 15 % of $Fe_3O_4$ was found using equation 2.1.

*3.2.1.1.4 Magnetic Phase Transition Study*

Figure 3.2.2 (B) shows the magnetic phase transitions of iron oxide and polymer coated iron oxide particles as a function of temperature. Curve (a) represents the transition of FeN and (b) is for CTN. By increasing temperature, the susceptibility decreased and ultimately became zero. In the derivative curves {Figure 3.2.2 (C)} for susceptibility vs temperature, few intergradations were observed where the magnetic samples showed minimal points. In the curve for FeN (curve a), significant transition ranges appeared viz. in the regions 246-312 °C and 424-502 °C, respectively. Minimum observed in the range 246-312 °C might be due to the phase transition of magnetite to meghemite [36]. Similarly, the second transition occurred in the region 424-502 °C might be due to the phase transition of the later to hematite [37]. In the curve for CTN (curve b), the intergradations in the range 246-312 °C was found to diminish. This might be attributed to the stabilization of FeN particles by the coated polymer and hence no prominent phase transition of magnetite to super paramagnetic maghemite appeared in the range.

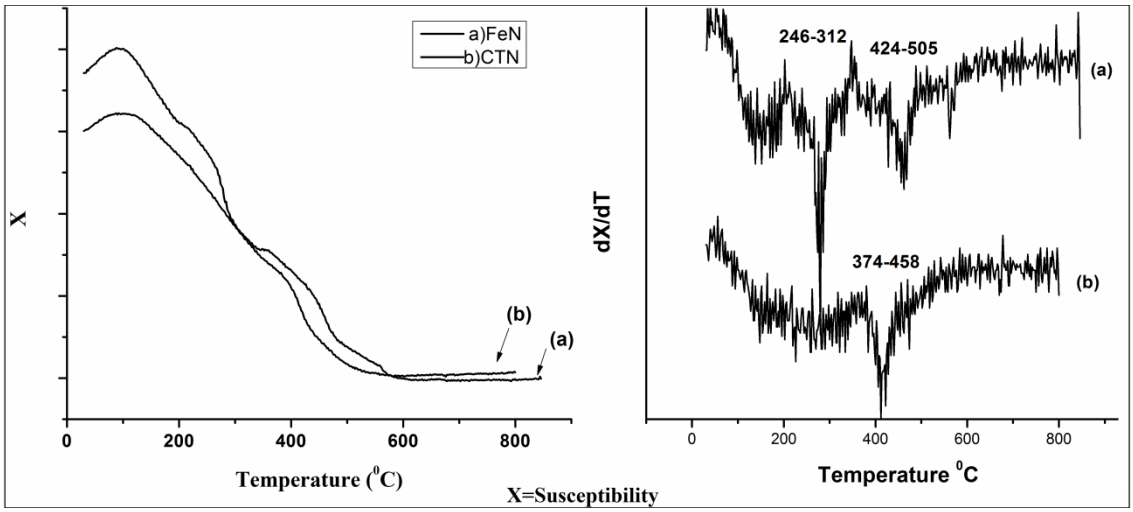


**Figure 3.2.2 (B)** Susceptibility vs temperature of (a) FeN (b) CTN, & First derivative of susceptibility vs temperature (a) FeN (b) CTN

*3.2.1.1.5 Scanning Electron Microscopy and Energy Dispersive X-Ray Analysis*

Figure 3.2.2 (A) shows the SEM images of chitosan, bare magnetite particles and CTN composite. From the SEM micrographs, it was observed that chitosan has an agglomerated surface (a). The agglomeration was less in bare FeN(b) particles. The agglomeration was least and the surface of the particles was smooth in CTN(c). Chitosan formed a coating over FeN particles and prevented them from agglomeration. The size of the agglomerates for FeN was smaller than those for CTN. But the amount of agglomeration is more in FeN than CTN. It is quantitatively depicted in the inset in Figure 3.2.3. The number of particles in FeN was found more compared to CTN over the same area and hence appeared more agglomerated. The size of the CTN particles was large and well separated from each other due to coating of chitosan on FeN particles. The hydrodynamic diameter of CTN determined by dynamic light scattering was also found to be more than bare FeN particles (Figure 3.2.5). The larger particle observed was of polymer over FeN due to coating

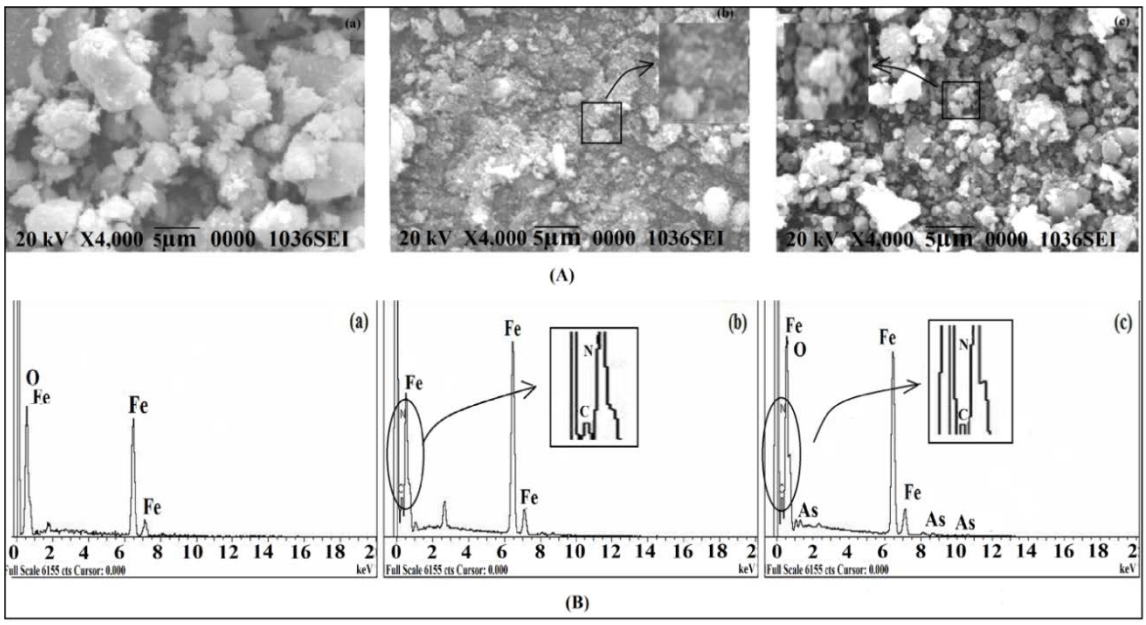


**Figure 3.2.3** (A) SEM micrographs of (a) CT,( b) FeN, (c) CTN, (B) Elemental compositions of (a) FeN, (b) CTN before adsoption and (c) CTN after adsorption

Figure 3.2.3 (B) shows the relative compositions of different components of FeN, CTN before and after arsenic adsorption. The EDX data showed the distribution

of different components in the composite individually and as a whole. It was confirmed that As(V) was well adsorbed on the surface of CTN (c).

### *3.2.1.2 Batch Adsorption Experiment*

*3.2.1.2.1 Effect of Adsorbent (CTN) Dose on Removal Efficiency of As(V)*

The effect of adsorbent dose at a fixed As(V) solution concentration (0.6 mg/L) and near neutral pH on percent removal of As(V) is shown in Figure 3.2.4 (A). The dose of material was varied from 0.2-2.0 g/L of solution and the treatment was carried out for 4 h. It was observed that for this solution under investigation, the removal efficiency increased up to 1 g/L adsorbent dose, beyond that remained almost unchanged. At low adsorbent dose, the available active sites were not sufficient to adsorb the required As(V) from its solution. With the increase in adsorbent dose, the availability of more active sites facilitated the removal efficiency. It was observed that for a solution of 0.6 mg/L, a dose of 1 g/L CTN was sufficient to bring down the As(V) concentration below 10 µg/L. However, at higher adsorbent dose no significant improvement in percent removal was observed. It might be due to decrease in As(V) concentration gradient of between As(V) in solution and active sites of the adsorbent.

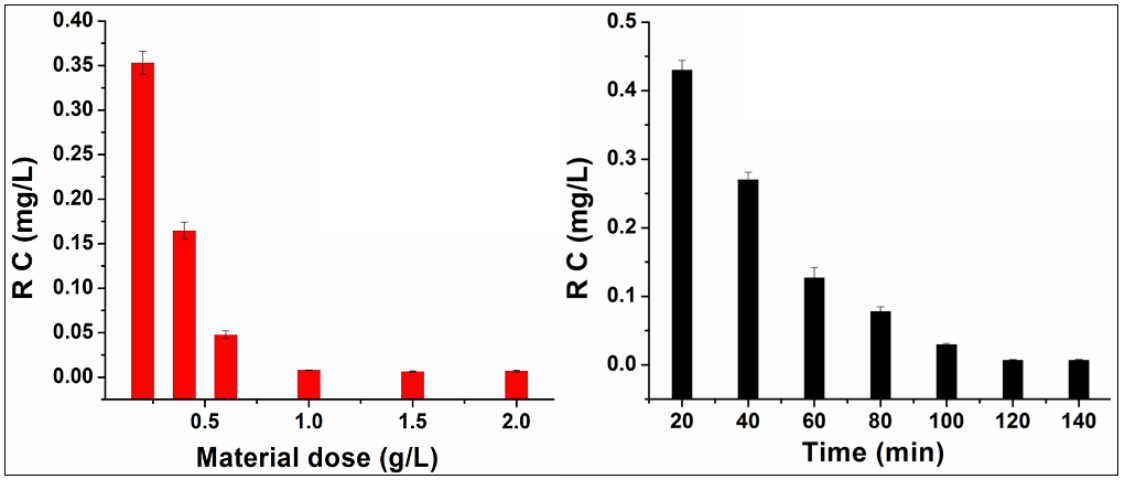


**Figure 3.2.4** Effect of (A) adsorbent dose and (B) Agitation time on removal of As(V) [R C: Residual concentration of As(V)]

*3.2.1.2.2 Influence of Agitation Time on Removal Efficiency of As(V)*

Figure 3.2.4 (B) shows the effect of agitation time on percent removal of As(V) ion. To study the effect of time on removal efficiency, concentration of As(V) solution and

adsorbent dose were kept at 0.6 mg/L and 1g/L respectively and the experiment was carried out near neutral pH. The rate of removal of As(V) was found to increase initially with increase in contact time up to 120 min, beyond that it almost flatten off. This was due to the establishment of equilibrium between the active sites on CTN surface and arsenate ions from the aqueous phase. Kwok et al. [38] studied the sorption of As(V) onto chitosan flakes and reported an achievement in equilibrium after certain contact time. Comparison of efficiency of CTN was also carried out with CT and FeN for the optimized time and dose for the targeted solution of 0.6 mg/L. Studies indicated that CTN showed better removal efficiency (~98%) than CT alone (~49%) and bare FeN particle (~93%). This suggested the formation of more sorption sites caused by the increase in surface area of resultant composite due to stabilization by chitosan and also due to synergistic effect of both the materials. The hydrodynamic diameters of FeN and CTN particles measured by dynamic light scattering are shown in Figure 3.2.5. The diameter was not evaluated for Chitosan, as in all the experiments it is used in the soluble form and can't be determined by dynamic light scattering. The hydrodynamic diameter of CTN was measured and found to be more than bare FeN particles. This was due to the coating of FeN particles by chitosan. These results were further confirmed by judging the settling time of the two materials in aqueous medium.

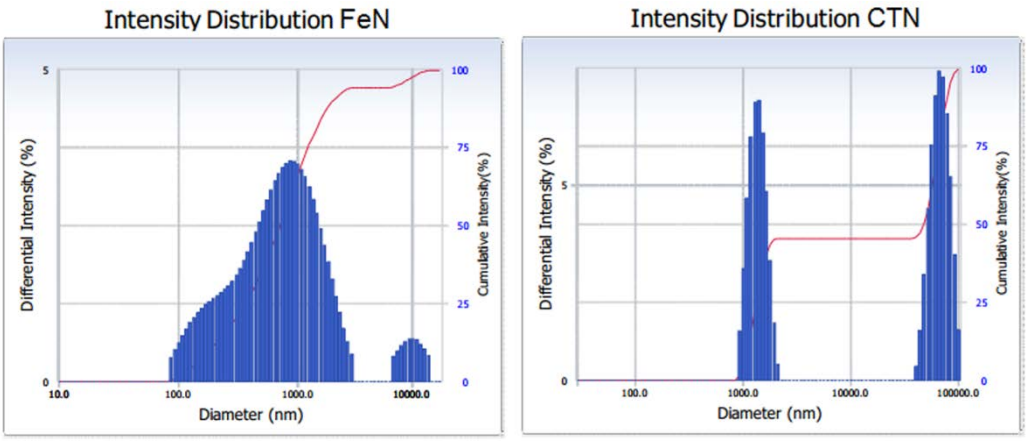


**Figure 3.2.5** Hydrodynamic diameters of FeN and CTN particles

It was observed that once the shaking was stopped during the treatment process, particles of FeN started forming large sized particles and some of the particles got settled earlier as compared to the CTN particles, indicating more tendency of it to agglomerate. Zhang et al. [39] used starch stabilized nanoscale magnetite particles

towards the remediation of arsenate contaminated soils and reported an improvement in adsorption affinity of nanoparticles towards arsenic. An et al. [40] also reported that starch coated magnetite nanoparticles removed arsenic more efficiently than bare magnetite nanoparticles from spent ion exchanged brine.

*3.2.1.2.3 Effect of Initial As(V) Concentration on Removal Efficiency*

The effect of initial ion concentration on removal efficiency of As(V) was studied in the concentration range of 0.4-4 mg/L. At first, for a targeted concentration of 0.6 mg/L the different influencing factors like treatment time, material dose etc. were optimized. These optimized conditions were also adopted for other concentrations to study the isotherm pattern. Mohan et al. [41] optimized the treatment time and material dose for a particular concentration and applied those optimized conditions in studying the sorption pattern of arsenic, cadmium and lead.

Figure 3.2.5 (A) shows the variation of removal efficiency as well as equilibrium adsorption capacity as a function of initial As(V) concentration. It was observed that the percent removal of As(V) decreased with the increase in initial metal ion concentration. This might be attributed to delayed establishment of equilibrium between adsorbent sites and the As(V) ions in aqueous phase due to increase in initial As(V) concentrations. But amount of metal ion uptake per unit weight of adsorbent (mg/g) increased. This discrepancy in behavior is due to increase in concentration gradient of arsenate ions between sorption sites and in aqueous phase.

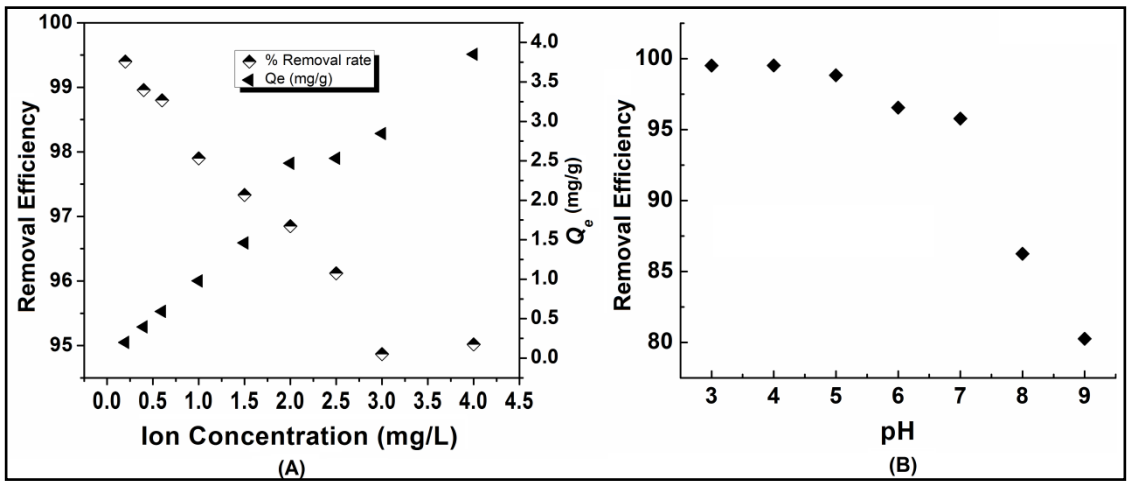


**Figure 3.2.6** Effect of (A) initial ion concentration, (B) pH on removal rate of As(V)

*3.2.1.2.4 Effect of pH on Removal Efficiency*

Figure 3.2.6 (B) shows the variation of arsenate removal efficiency as a function of initial pH of the solution. The removal efficiency was found to be higher when pH was low. This type of pH dependency of e As(V) can be explained both in terms of adsorbent and adsorbate response towards hydrogen ion concentration. Arsenate ions exist in different oxidation states viz. $H_3AsO_4$, $H_2AsO_4^-$, $HAsO_4^{2-}$ and $AsO_4^{3-}$ at different pH conditions 2.0, 2.0-7.0, 7.0-12.0, and ›12.0, respectively [39]. The $Q_e$ vs $C_e$ curve {Figure 3.2.7 (A)} indicated an electrostatic type of interaction between the adsorbent and As(V) in solution at lower ion concentrations. Again, in acidic pH the proton generated was utilized to remove the $OH^-$ ions from the coordinating layer of the adsorbent providing sites for anion binding. Moreover, active sites like -OH, $-NH_2$, etc. present on the adsorbent surface get protonated in acidic pH, thus, can bind readily with anions from solution. These implied the favorability of the sorption process at low pH (2.0-7.0). When pH was increased, $OH^-$ ion concentrations in solution increases. This causes competition between Arsenate ions and hydroxide ions for the binding sites resulting into lower removal efficiency. Although chitosan formed a nice coat over FeN surfaces and crosslinking was used to immobilize the magnetite particles, yet the breakage of some binding sites might took place in presence of acid. Also, some of polymeric units might get degraded due to the effect of acid and thus, iron particles present on those sites might get leached. Moreover, the amount of crosslinker used might not be sufficient to immobilize all the iron particles on the polymer. The loss of FeN in the composite was tested by analyzing the presence of iron (AAS analysis) in the aliquot after first sorption-desorption experiment. Iron present in deionized water as well as the aliquot after first sorption experiment was also determined for comparison purpose. It was found that the amount of iron in the deionized water was negligible. In the aliquot after first sorption test a substantial amount of iron (~0.32 mg/L) was found which might be due to leaching of some iron particles, whereas, it was ~2.2 mg/L after combining treatment of sorption and desorption. This can be further reduced by simple sand filtration in a secondary treatment process. Therefore, a pH value near 3-4 is considered as the optimum one for best removal of arsenate ions from solution.

***3.2.1.3 Adsorption Kinetics***

Figure 3.2.7 represents different kinetic model for sorption of As(V) on CTN. The correlation coefficients ($R^2$) were computed and all the values are shown in Table 3.2.1. The $Q_e$ values were found to increase with increase in initial As(V) concentrations. The correlation coefficient for pseudo second order model was higher compared to pseudo first order model.

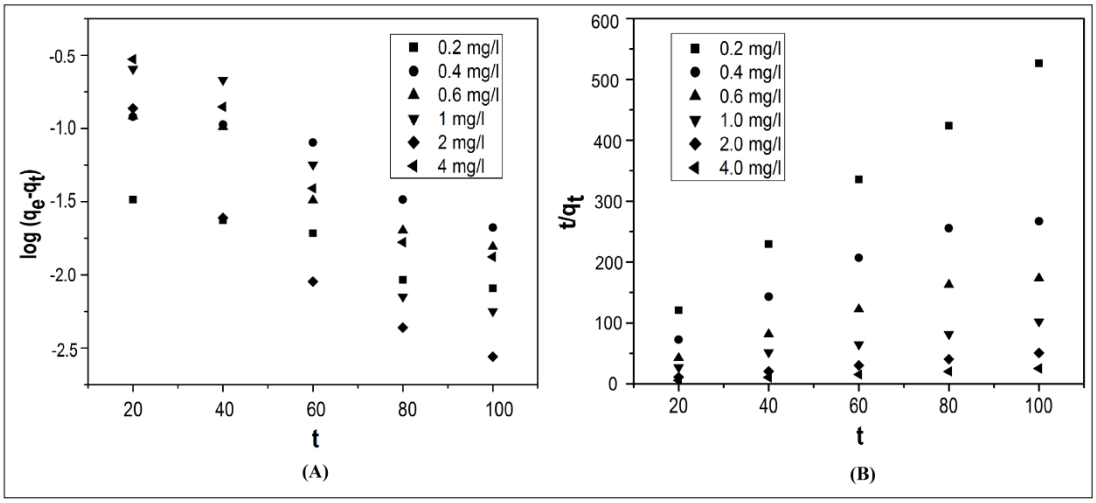


**Figure 3.2.7** First order (A) and Second order (B) kinetic model for sorption of As(V) on CTN

Better fitting of the experimental data with the pseudo second order model indicated a monolayer chemisorption pattern in the concentration range under investigation. This pointed out chemical interaction between the adsorbent and arsenate ions in solution as mentioned earlier.

**Table 3.2.1** Parameters for different kinetic models for sorption of As(V) on CTN

| $C_o$ (mg/L) | First order kinetic model | | Second order kinetic model | | | |
|---|---|---|---|---|---|---|
| | $K_1$ ($min^{-1}$) | $R^2$ | $K_2$ $gmg^{-1}min^{-1}$ | $Q_e$ (Cal) (mg/g) | $H$ | $R^2$ |
| 0.2 | 1.86 | 0.935 | 0.992 | 0.198 | 0.039 | 0.998 |
| 0.4 | 2.33 | 0.896 | 0.162 | 0.398 | 0.026 | 0.932 |
| 0.6 | 2.86 | 0.913 | 0.216 | 0.582 | 0.073 | 0.962 |

| | | | | | | |
|---|---|---|---|---|---|---|
| 1.0 | 5.51 | 0.896 | 0.069 | 0.971 | 0.086 | 0.988 |
| 2.0 | 4.76 | 0.919 | 0.368 | 2.08 | 1.480 | 0.999 |
| 4.0 | 4.17 | 0.946 | 0.125 | 4.03 | 2.030 | 0.999 |

### *3.2.1.4 Adsorption Isotherm*

The correlation coefficient was found to be 0.976. $Q_0$ and 'b' were found to be 10.81 mg/g and 0.025 L/mg, respectively, as determined from the slope and intercept of the plot of $1/Q_e$ vs $1/C_e$.

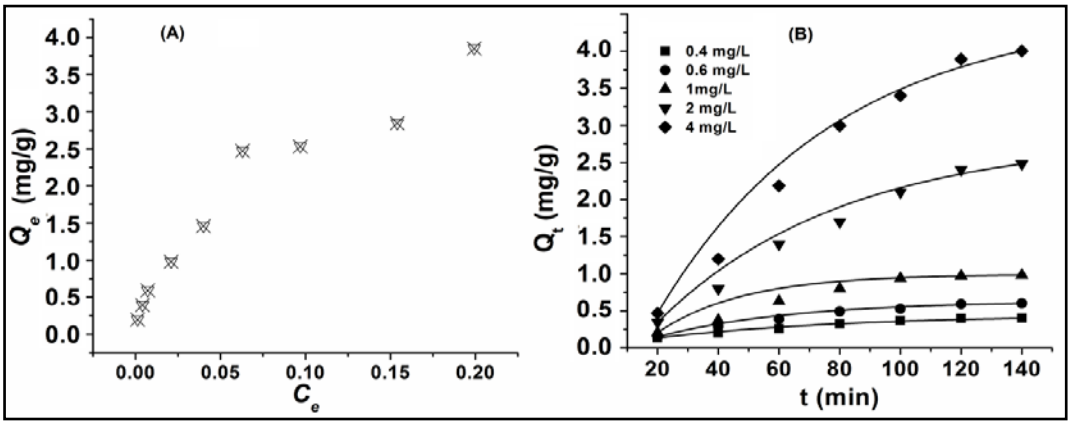


**Figure 3.2.8 (A)** Qe vs Ce curve and **(B)** Qt vs t curve for the sorption of As(V) on CTN

$R^2$ value showed fitting of data obtained with the isotherm. Due to the heterogeneity in sorption process appearing at higher concentration, $Q_{max}$ value was calculated using Langmuir pattern at lower concentrations. Cozmuta et al. [42] derived the maximum adsorption capacity for the adsorption of lead on Na-clinoptilolite using Langmuir model although the sorption was taking place in a heterogeneous surface.

**Table 3.2.2** Parameters of different isotherm models for sorption of As(V) on CTN

| **Isotherm model** | **Parameters** | **Value** |
|---|---|---|
| **Langmuir** | $Q_o$ (mg/g) | 10.81 |
| | $b$ | 0.025 |
| | $R_L$ | 0.985 |
| | $R^2$ | 0.976 |
| **Freundlich** | $k_f$ (mg/g) | 0.883 |
| | $n$ | 1.786 |
| | $R^2$ | 0.995 |

Table 3.2.2 shows the Langmuir and Freundlich isotherm parameters obtained at room temperature. It was observed that the $R^2$ values for both Langmuir and Freundlich isotherms showed good co-relations of the data. Moreover, the $R_L$ (~0.985, for Langmuir) and n (~1.786, for Freundlich) values also indicated good fitting of the experimental data. Thus, the sorption could be reasonably explained with both the isotherms. It is a complicated situation when both the Langmuir and Freundlich isotherms adequately describe the same set of liquid-solid adsorption data at certain concentration ranges, in particular if the concentration is small. This happens when the adsorption capacity of the solid is large enough to make both isotherm equations approach a linear form

But the correlation coefficient values showed that Freundlich isotherm showed better fitting ($R^2$=0.995) as compared to Langmuir ($R^2$=0.976) model in the concentration range under investigation. These ($R_L$ and n) implied a multilayer physisorption pattern of As(V) on adsorbent surface. In the $Q_e$ vs $C_e$ curve, two types of behaviors were observed.

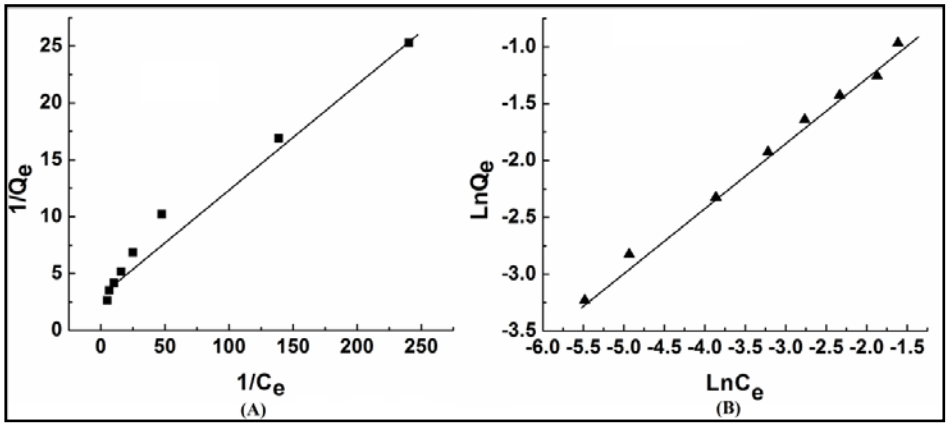


**Figure 3.2.9** (A) Langmuir (B) Freundlich isotherm models for sorption of As(V) on CTN

In low concentration range a monolayer type of coverage was appeared. This might be due to formation of strong electrostatic type of binding (amine functionally on chitosan which may exist as $–NH_3^+$) or complex covalent bonds (Fe-O-As) between the adsorbent and arsenate ions in solution. Boddu et. al [43] cited the interaction of As(V) with chitosan coated biosorbents as electrostatic one and the sorption was governed by Langmuir adsorption isotherm. The monolayer chemisorption pattern was observed at

only low concentrations of arsenate ions. At low concentration, number of active binding sites on adsorbent was sufficient to bind arsenate ions. But at higher concentrations, the binding sites involved in chemisorption became saturated and then weak van der Waals forces might arise in bond formation. Wit et al. [44] explained the heterogeneity involve in adsorption model for proton binding by humic substances.

**Table 3.2.3** Comparison of efficiency with other established material

| Material | Arsenic species | $Q_o$ (mg/g) | *Remark* |
|---|---|---|---|
| $Fe_3O_4$-NPs [45] | As(V) | 0.4 | - |
| MICB [46] | As(III)<br>As(V) | ~35 for both | Preparation is not simple |
| FMO [23] | As(V)<br>As(III) | 15.38<br>0.5367 | Desorption of arsenic is difficult |
| Material under investigation | As(V) | 10.81 | Simple preparation technique |

A comparative study of the maximum adsorption capacity ($Q_o$) calculated from Langmuir model was shown in Table 3.2.3, with some other established material. Ferruginous manganese ore (FMO) had a high adsorption capacity as shown in table, but arsenic did not get desorbed easily even on varying the pH. Similar material MICB reported by Wang et al. [44] showed very high sorption capacity for both As(III) and As(V). But the sorption experiments were carried out with very high initial arsenic concentration, limiting the practical applicability of the material. Moreover, the material preparation step was much more complicated as compared to the present case. Material under present investigation was quite easy to prepare and processing and showed sufficiently good results and cyclic run was also carried out for several times.

### *3.2.1.5 Effect of Competing Ions on As(V) Removal*

The effect of competing ions viz. phosphate and chloride ions, on arsenate removal by CTN in synthetic water was investigated. Figure 3.2.10 A) shows the variation of the sorption rate of arsenate ions with the elevated concentration of

phosphate and chloride ions. The experiments were carried out with prepared solutions containing arsenate/phosphate and arsenate/chloride ions at neutral pH. The change in removal efficiency was monitored with elevated concentration of phosphate and chloride ions in two separate experiments.

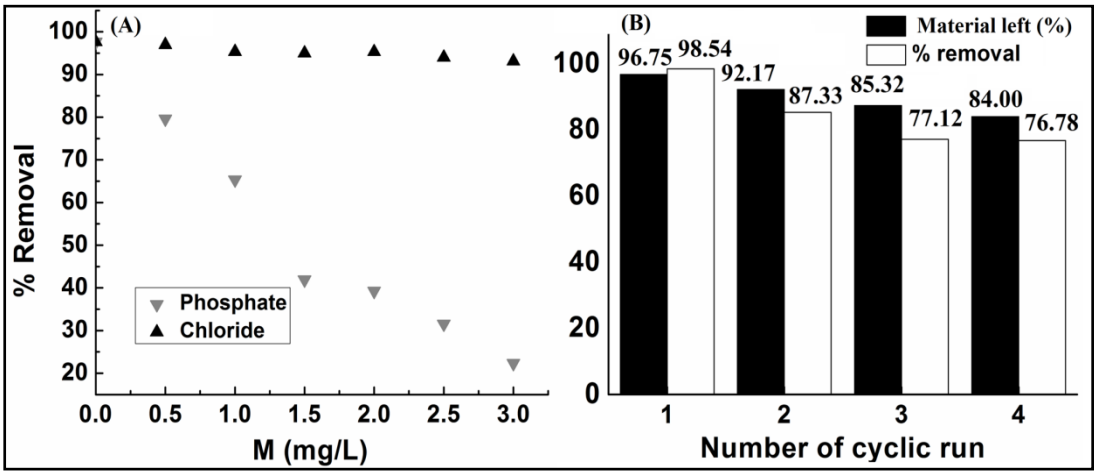


**Figure 3.2.10** A) Effect of co-ions on removal rate B) Reusability after cyclic run of CTN (Arsenate concentration: 0.6 mg/L)

No significant effect of chloride on the removal efficiency was observed. Similar observation was reported by Youngran et al. [47] while studying the effect for $Fe_2O_3$. But it was notably affected by the increase in concentration of phosphate ions present in the solution. This decrease in removal efficiency of arsenate ions from solution was due to the formation phosphate surface complex with CTN. Daou et al. [48] studied the formation of monoprotonated binuclear phosphate complex on magnetite surface. Thus, competition of arsenate and phosphate ions took place for the sorption sites resulting into a decrease in removal efficiency.

### *3.2.1.6 Reusability Experiment*

To study the advantage of using the combined system, reusability test was carried out for four cyclic runs. In each cyclic run, after treatment with of the Arsenate water the material used were separated by tiny magnet and desorbed with 0.1 M HCl solution and again subjected to arsenate water treatment. Figure 3.2.10 (B) shows the percent loss of material and removal efficiency after each cyclic run.

From the figure it was clear that after each cyclic run some amount of material were lost. This might be due to the leaching of some $Fe^{2+}$ and $Fe^{3+}$ ions on acid treatment. Also, the polymeric material coated over FeN might also lose its surface integrity on acid treatment. Again, after each cyclic run, the removal efficiency of arsenate ions decreased and this decrease in removal efficiency was more prominent after more number of cyclic runs. The decrease in removal efficiency could be attributed to the partial desorption of arsenate ions from the adsorbent surface and also due to loss in integrity of material on acid treatment.

**References**

[1] Gandhi, M. R., Viswanathan, N. and Meenakshi, S. Preparation and application of alumina/chitosan biocomposite. *International journal of biological macromolecules*, 47:146-154, 2010.

[2] Yanfang, S., Yun, L., Yun, Y. and Jianjun, L. Enhancing adsorption of Pb (II) and Cu (II) ions onto chitosan using tri-sodium citrate and epichlorohydrin as cross-linkers. *Desalination and Water Treatment*, 52:6430-6439, 2014.

[3] Ngaha, W. W., Teong, L. C. and Hanafiah, M. A. K. M. Adsorption of dyes and heavy metal ions by chitosan composites: A review. *Carbohydrate polymers*, 83:1446-1456, 2011.

[4] Nagy, N. M., Konya, J., Beszeda, M., Beszeda, I., Kalman, E., Keresztes, Z. and Cserny, I. Physical and chemical formations of lead contaminants in clay and sediment. *Journal of colloid and interface science*, 263:13-22, 2003.

[5] Hosseinzadeh, H., Zoroufi, S. and Mahdavinia, G. R. Study on adsorption of cationic dye on novel kappa-carrageenan/poly (vinyl alcohol)/montmorillonite nanocomposite hydrogels. *Polymer Bulletin*, 72:1339-1363, 2015.

[6] Lenoble, V., Bouras, O., Deluchat, V., Serpaud, B. and Bollinger, J. C. Arsenic adsorption onto pillared clays and iron oxides. *Journal of Colloid and Interface Science*, 255:52-58, 2002.

[7] Bhattacharyya, K. G. and Gupta, S. S. Adsorption of a few heavy metals on natural and modified kaolinite and montmorillonite: a review. *Advances in colloid and interface science*, 140:114-131, 2008.

[8] Arida, C. V. J., de Luna, M. D. G., Futalan, C. M. and Wan, M. W. Optimization of As (V) removal using chitosan-coated bentonite from groundwater using Box–Behnken design: effects of adsorbent mass, flow rate, and initial concentration. *Desalination and Water Treatment*, 57:18739-18747, 2016.

[9] Nayak, P. S. and Singh, B. K. Instrumental characterization of clay by XRF, XRD and FTIR. *Bulletin of Materials Science*, 30:235-238, 2007.

[10] Madejová, J. FTIR techniques in clay mineral studies. *Vibrational spectroscopy*, 31:1-10, 2003.

[11] Kousalya, G. N., Gandhi, M. R. and Meenakshi, S. Sorption of chromium (VI) using modified forms of chitosan beads. *International Journal of Biological Macromolecules*, 47:308-315, 2010.

[12] Liu, J. and Zhao, F. Characterization of arsenate adsorption on amorphous Al gels with Keggin structure by Fourier transformed infrared spectroscopy and MAS 27 Al NMR. *Chinese Journal of Geochemistry*, 28:61-69, 2009.

[13] Kherroub, D. E., Belbachir, M., Lamouri, S., Bouhadjar, L. and Chikh, K. Synthesis of polyamide-6/montmorillonite nanocomposites by direct in-situ polymerization catalysed by exchanged clay. *Oriental Journal of Chemistry*, 29:1429-1436, 2014.

[14] Zhang, Z., Liu, B., Lv, K., Sun, J. and Deng, K. Aerobic oxidation of biomass derived 5-hydroxymethylfurfural into 5-hydroxymethyl-2-furancarboxylic acid catalyzed by a montmorillonite K-10 clay immobilized molybdenum acetylacetonate complex. *Green Chemistry*, 16:2762-2770, 2014.

[15] Rhim, J. W., Hong, S. I., Park, H. M. Ng, P. K. Preparation and characterization of chitosan-based nanocomposite films with antimicrobial activity. *Journal of agricultural and food chemistry*, 54:5814-5822, 2006.

[16] Frost, R. R., and Griffin, R. A. Effect of pH on Adsorption of Arsenic and Selenium from Landfill Leachate by Clay Minerals *Soil Science Society of America Journal*, 41:53-57, 1977.

[17] Usuki, A., Kawasumi, M., Kojima, Y., Okada, A., Kurauchi, T., and Kamigaito, O. Swelling behavior of montmorillonite cation exchanged for ω-amino acids by∈-caprolactam. *Journal of Materials Research*, 8:1174-1178, 1993

[18] Pandey, S. and Mishra, S. B. Organic–inorganic hybrid of chitosan/organoclay bionanocomposites for hexavalent chromium uptake. *Journal of colloid and interface science*, 361:509-520, 2011.

[19] Mohan, D., Pittman, C. U., Bricka, M., Smith, F., Yancey, B., Mohammad, J. and Gong, H. Sorption of arsenic, cadmium, and lead by chars produced from fast pyrolysis of wood and bark during bio-oil production. *Journal of colloid and interface science*, 310:57-73, 2007.

[20] Li, Z. and Bowman, R. S. Retention of inorganic oxyanions by organo-kaolinite. *Water Research*, 35:3771-3776, 2001.

[21] Lin, Z. and Puls, R. W. Adsorption, desorption and oxidation of arsenic affected by clay minerals and aging process. *Environmental Geology*, 39:753-759, 2000.

[22] Moreno-Jiménez, E., Esteban, E. and Peñalosa, J. M. The fate of arsenic in soil-plant systems. In Reviews of environmental contamination and toxicology 1-37, 2012, Springer New York.

[23] Mohapatra, D., Mishra, D., Chaudhury, G. R. and Das, R. P. Arsenic (V) adsorption mechanism using kaolinite, montmorillonite and illite from aqueous medium. *Journal of Environmental Science and Health Part A*, 42:463-469, 2007.

[24] Anjum, A., Lokeswari, P., Kaur, M., & Datta, M. (2011). Removal of As (III) from aqueous solutions using montmorillonite. Journal of Analytical Sciences, Methods and Instrumentation, 1(02), 25.

[25] Gupta, A., Yunus, M. and Sankararamakrishnan, N. Zerovalent iron encapsulated chitosan nanospheres–A novel adsorbent for the removal of total inorganic Arsenic from aqueous systems. *Chemosphere*, 86:150-155, 2012.

[26] Khodabakhshi, A., Amin, M. M. and Mozaffari, M. Synthesis of magnetite nanoparticles and evaluation of its efficiency for arsenic removal from simulated industrial wastewater. *Iranian Journal of Environmental Health Science & Engineering*, 8:189, 2011.

[27] Mamindy-Pajany, Y., Hurel, C., Marmier, N. and Roméo, M. Arsenic (V) adsorption from aqueous solution onto goethite, hematite, magnetite and zero-valent iron: effects of pH, concentration and reversibility. *Desalination* 281:93-99, 2011.

[28] Zhang, L., He, R. and Gu, H. C. Oleic acid coating on the monodisperse magnetite nanoparticles. *Applied Surface Science*, 253:2611-2617, 2006.

[29] Chang, Y. C. and Chen, D. H. Preparation and adsorption properties of monodisperse chitosan-bound Fe3O4 magnetic nanoparticles for removal of Cu (II) ions. *Journal of Colloid and Interface Science*, 283:446-451, 2005.

[30] Ratnaike, R. N. Acute and chronic arsenic toxicity. *Postgraduate medical journal*, 79:391-396, 2003.

[31] Akin, I., Arslan, G., Tor, A., Ersoz, M. and Cengeloglu, Y. Arsenic (V) removal from underground water by magnetic nanoparticles synthesized from waste red mud. *Journal of hazardous materials*, 235:62-68, 2012.

[32] Unsoy, G., Yalcin, S., Khodadust, R., Gunduz, G. and Gunduz, U. Synthesis optimization and characterization of chitosan-coated iron oxide nanoparticles produced for biomedical applications. *Journal of Nanoparticle Research*, 14:964, 2012.

[33] Li, M. C., Liu, C., Xin, M. H., Zhao, H., Wang, M., Feng, Z. and Sun, X. L. Preparation and characterization of acylated chitosan. *Chem Res Chinese U*, 21:114-116, 2005.

[34] Lu, G., Kong, L., Sheng, B., Wang, G., Gong, Y. and Zhang, X. Degradation of covalently cross-linked carboxymethyl chitosan and its potential application for peripheral nerve regeneration. *European Polymer Journal*, 43:3807-3818, 2007.

[35] Kim, S. S., Kim, S. J., Moon, Y. D. and Lee, Y. M. Thermal characteristics of chitin and hydroxypropyl chitin. *Polymer*, 35:3212-3216, 1994.

[36] Li, J. H., Hong, R. Y., Li, H. Z., Ding, J., Zheng, Y. and Wei, D. G. Simple synthesis and magnetic properties of Fe3O4/BaSO4 multi-core/shell particles. *Materials Chemistry and Physics*, 113:140-144, 2009.

[37] Jafari, A., Shayesteh, S. F., Salouti, M. and Boustani, K. Effect of annealing temperature on magnetic phase transition in Fe3O4 nanoparticles. *Journal of Magnetism and Magnetic Materials*, 379:305-312, 2015.

[38] Kwoka, K. C. M., Leea, V. K. C., Gerenteb, C. and McKay G. Novel model development for sorption of arsenate on chitosan, *Chemical Engineering Journal* 151:122-133, 2009.

[39] Zhang, M., Pan, G., Zhao, D. and He, G. XAFS study of starch-stabilized magnetite nanoparticles and surface speciation of arsenate. *Environmental pollution*, 159:3509-3514, 2011.

[40] An, B., Liang, Q. and Zhao, D. Removal of arsenic (V) from spent ion exchange brine using a new class of starch-bridged magnetite nanoparticles. *Water research*, 45:1961-1972, 2011.

[41] Mohan, D. and Pittman, C. U. Arsenic removal from water/wastewater using adsorbents—a critical review. *Journal of hazardous materials*, 142:1-53, 2007.

[42] Cozmuta, L. M., Cozmuta, A. M., Peter, A., Nicula, C., Nsimba, E. B. and Tutu, H. The influence of pH on the adsorption of lead by Na-clinoptilolite: kinetic and equilibrium studies. *Water Sa*, 38:269-278, 2012.

[43] Boddu, V. M., Abburi, K., Talbott, J. L., Smith, E. D. and Haasch, R. Removal of arsenic (III) and arsenic (V) from aqueous medium using chitosan-coated biosorbent. *Water research*, 42:633-642, 2008.

[44] De Wit, J. C., van Riemsdijk, W. H. and Koopal, L. K. Proton binding to humic substances. 2. Chemical heterogeneity and adsorption models. *Environmental science & technology*, 27:2015-2022, 1993.

[45] Chakravarty, S., Dureja, V., Bhattacharyya, G., Maity, S. and Bhattacharjee, S. Removal of arsenic from groundwater using low cost ferruginous manganese ore. *Water research*, 36:625-632, 2002.

[46] Wang, J., Xu, W., Chen, L., Huang, X., & Liu, J. (2014). Preparation and evaluation of magnetic nanoparticles impregnated chitosan beads for arsenic removal from water. Chemical Engineering Journal, 251, 25-34.

[47] Youngran, J., Maohong, F. A. N., Van Leeuwen, J. and Belczyk, J. F. Effect of competing solutes on arsenic (V) adsorption using iron and aluminum oxides. *Journal of Environmental Sciences*, 19:910-919, 2007.

[48] Daou, T. J., Begin-Colin, S., Greneche, J. M., Thomas, F., Derory, A., Bernhardt, P. and Pourroy, G. Phosphate adsorption properties of magnetite-based nanoparticles. *Chemistry of Materials*, 19:4494-4505, 2007.

**Section B: Starch Based Nanocomposites in Arsenic Remediation**

Starch is one of the cheapest, nontoxic polymers, which is abundantly available in nature. The processing of starch for stabilizing nanomaterials is quite easy. Starch can be easily solubilized in hot water and reprecipitated by simply adding acetone or ethanol. Starch also can be functionalized on reacting with suitable reagents. Nanomaterials can be stabilized over starch/modified starch which causes less agglomeration of the former and improves the sorption along with its stability. Coating of nanomaterial by starch can be done in aqueous medium without using any other toxic chemicals. Two starch based nanocomposites were developed using titanium and iron based nanomaterials for remediation of arsenic as follows-

## 3.3 Equilibrium and kinetics study on Removal of Arsenate Ions from aqueous solution by CTAB/$TiO_2$ and Starch/CTAB/$TiO_2$ nanoparticles: A Comparative Study

$TiO_2$ and its modified forms are prominent scavenger of different arsenic species from contaminated water. But dispersibility, reusability and leaching of particles are the major concerns for the utility of $TiO_2$ in water purification. Nanoparticles have very high surface energy. Therefore, they tend to agglomerate to reduce surface area and thus, get stabilized [1]. Certain modifications are necessary in order to overcome these limitations. Adequate surface functionalization, coating with polymeric materials, etc., are some of bright aspects regarding selectivity and aqueous stability of this material.

Use of surfactant like CTAB increases stability of $TiO_2$ nanoparticles in water by forming micelle around them and thus, can enhance dispersibility of the particles in aqueous medium [2]. CTAB contains a hydrophilic end also. This might enhance solubility of modified $TiO_2$ particles in aqueous medium. Thus, some amount of particles may get leached in water during wastewater treatment. This difficulty may be avoided by the use of some supporting materials or by coating nanoparticles with polymeric materials.

Keeping all these into consideration, the work has been undertaken. The aim of this work is to prepare CTAB modified $TiO_2$ nanoparticles, stabilize by coating with starch and finally use it in treatment of As(V) contaminated water. A comparative study

was made among unmodified $TiO_2$ (UTi), CTAB modified $TiO_2$ (CMT) and starch coated CMT (SPC). Low concentrations of arsenic solutions were taken in the experiments considering practical applicability of the material.

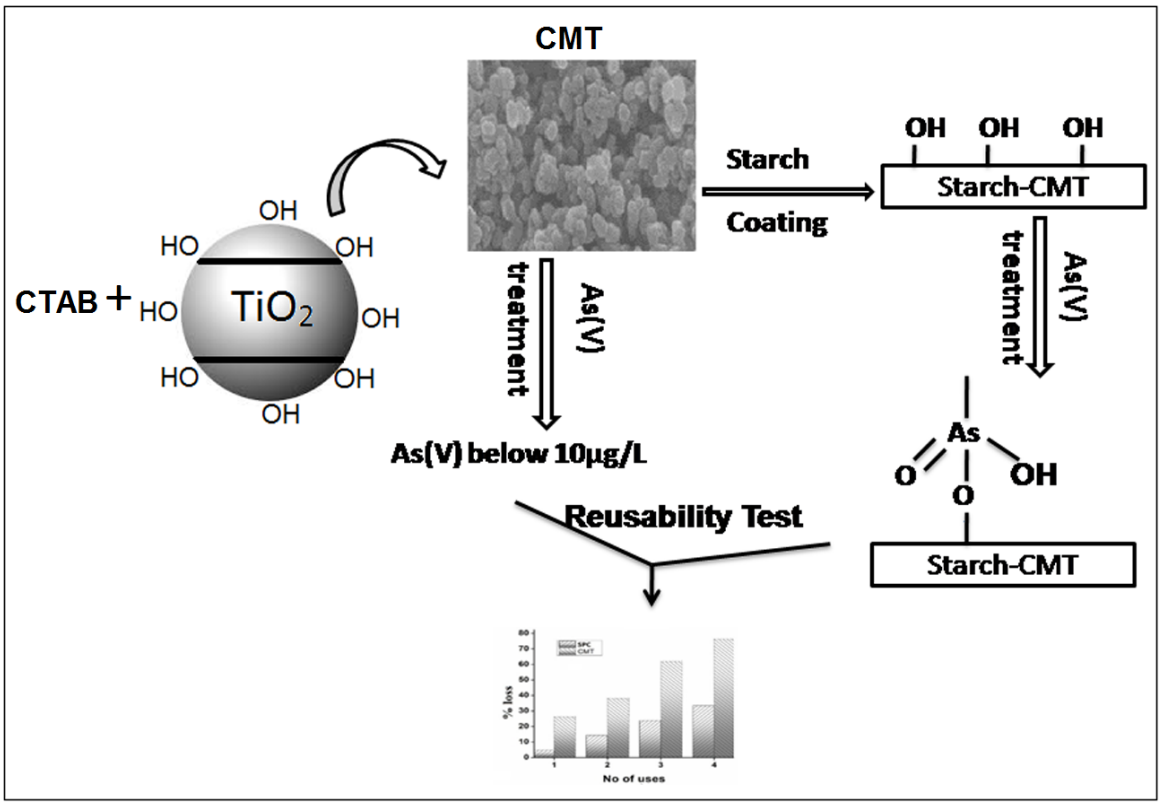


**Scheme 3.3.1** Schematic representation of preparation of the nanocomposite and use in arsenic treatment

### 3.3.1 Results and Discussion

#### *3.3.1.1 Characterisation*

*3.3.1.1.1 FT-IR analysis*

FT-IR spectra of CTAB, UTi and CMT are shown in Figure 3.3.1 A. FT-IR spectrum of UTi nanoparticles is shown in Figure 3.3.1 A(a). Strong absorbance near 500 $cm^{-1}$ was attributed to the Ti-O-Ti stretching of $TiO_2$. The absorbance at 3436-3490 (-OH stretching) and 1636 $cm^{-1}$ (-OH bending) were assigned to surface hydroxyl groups of $TiO_2$ [3].

In the spectrum of CTAB [{Figure 3.3.1 A(b)}], absorption bands appeared at 2916 $cm^{-1}$ and 2848 $cm^{-1}$ were assigned to asymmetric and symmetric modes of $–CH_2$

stretching in methylene chains, respectively [4]. Band near 1474 $cm^{-1}$ may be due to symmetric stretching of $CH_3^+$-N bond [5].

Presence of bands near 2916 $cm^{-1}$, 2850 $cm^{-1}$and 1463 $cm^{-1}$ (corresponding to CTAB) along with bands at 1636 $cm^{-1}$ and near 530 $cm^{-1}$ (corresponding to $TiO_2$) in the CMT spectrum indicate the probable interactions between the individual components (Figure 3.3.1 A(c)).

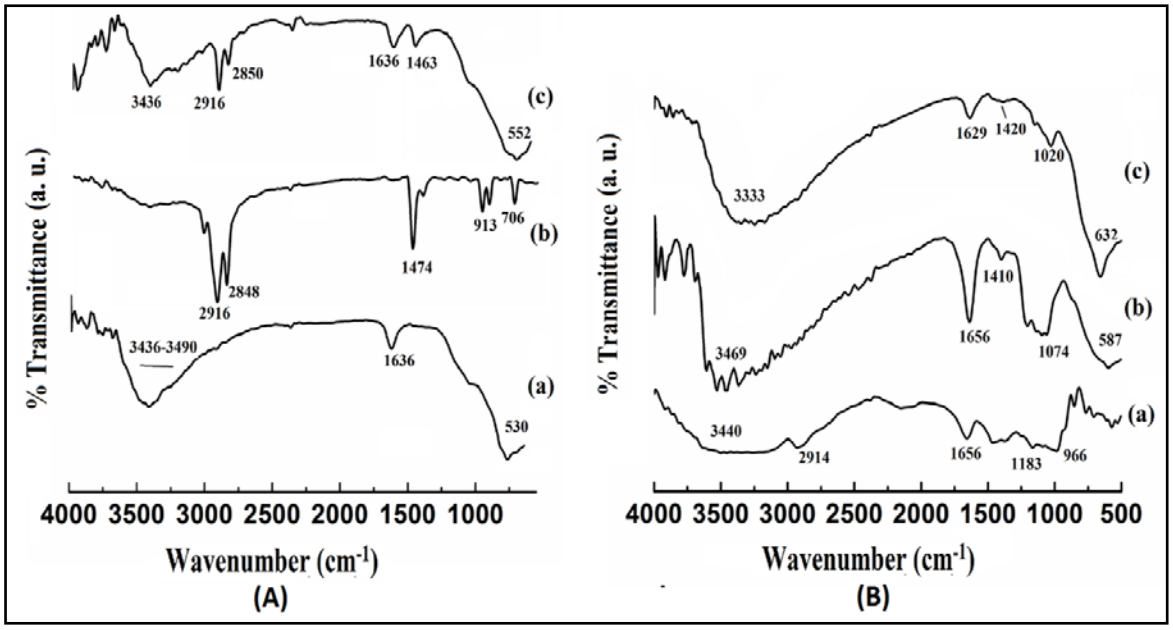


**Figure 3.3.1** FTIR spectra of A-(a) UTi, (b) CTAB, (c) CMT and B-(a) starch, (b) SPC and (c) ATC

Figure 3.3.1 B shows FTIR spectra of starch, SPC and arsenic treated SPC (ATC). Spectrum for starch [{Figure 3.3.1 B(a)}] showed the presence of broad band near 3440 $cm^{-1}$ for -OH stretching, 2914 $cm^{-1}$ for -CH stretching and 1656 $cm^{-1}$ for –OH bending. The two peaks in the region 1183-966 $cm^{-1}$ could be assigned to C-O bond stretching of C-O-H group [6]. Incorporation of CMT into starch could be well predicted from the curve (b). Increase in intensities of bands corresponding to -OH stretching and -OH bending as well as appearance of a new band near 1410 $cm^{-1}$ ($CH_3$-$N^+$ of CMT) was an indication for interaction between the two components.

In the FT-IR spectrum of ATC [{Figure 3.3.1 B(c)}], it was observed that intensity of bands assigned for hydroxyl groups and C-N stretching in SPC decreased prominently. This might be due to participation of those groups in arsenic binding. The

band appearing near 632 $cm^{-1}$ could be attributed to the adsorbed arsenate ions on to the material [7].

*3.3.1.1.2 SEM Analysis*

Figure 3.3.2 shows SEM micrographs of bare $TiO_2$ (a), CTAB modified $TiO_2$ (b) and starch coated modified $TiO_2$ (c). SEM micrographs of arsenic sorbed starch coated $TiO_2$ is shown in (d). The sorption and desorption of arsenic for both starch coated modified $TiO_2$ and CTAB modified $TiO_2$ were done for four times and then micrographs were taken. Figure 3.3.2 (e) and (f) are micrographs of used starch coated modified $TiO_2$ and CTAB modified $TiO_2$.

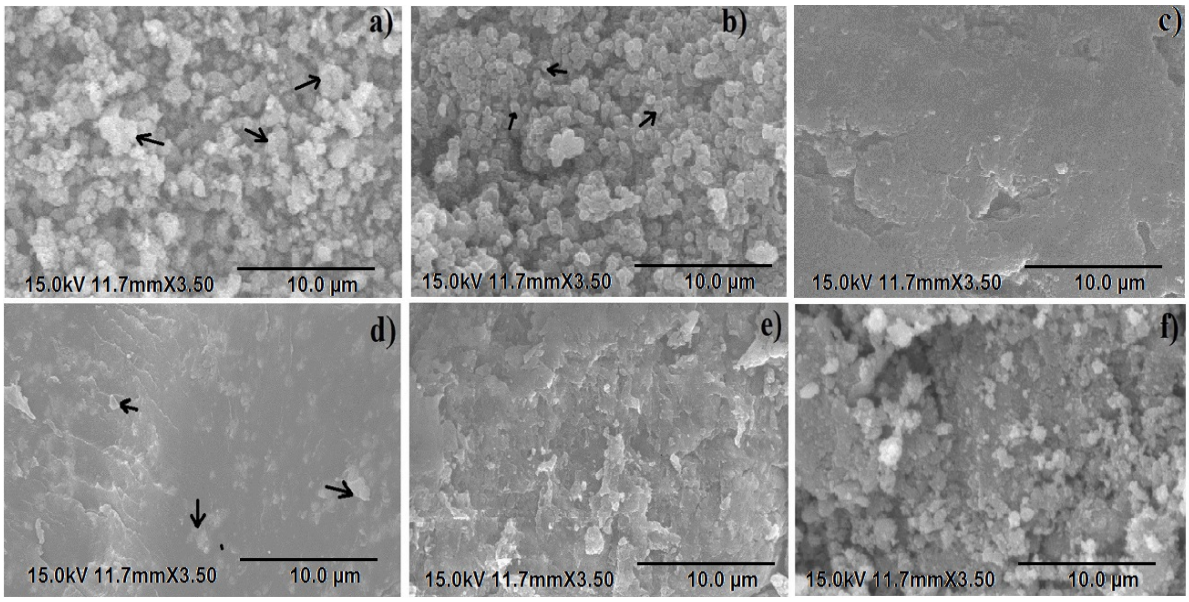


**Figure 3.3.2** SEM images of (a) UTi, (b) CMT, (c) SPC, (d)ATC, (e) SPC/4 (f) CMT/4

CTAB modified $TiO_2$ nanoparticles (b) became less agglomerated compared to those of unmodified $TiO_2$ (a) due to presence of long hydrocarbon chains of CTAB which prevented them from agglomeration. Jiang et al. [8] studied the morphology of CTAB modified Ni nanoparticles and observed that modification with CTAB resulted in irregular sphere like structures which were less aggregated compared to only nickel nanoparticles. Arsenic sorbed starch/$TiO_2$ (d) composite appeared little bit rough compared to arsenic free starch/$TiO_2$ (c) composites. This might be due to sorbed arsenic on the composite structure. The surface of arsenic desorbed composite (e) was more rough compared to starch/$TiO_2$ composite (c). This might be attributed to disintegration of the surface of the composite caused by repeated washing with acid

during sorption-desorption treatment. Similarly, shape of CTAB modifed/$TiO_2$ nanoparticles (f) became irregular and rough due to the acid treatment.

*3.3.1.1.3 EDX Study*

Figure 3.3.3 (a-e) show the EDX spectra of UTi, CTAB, CMT, SPC, Arsenic treated CMT (AMT) and Arsenic treated composite (ATC), respectively. EDX spectra of UTi (a) and CTAB (b) showed the presence of their corresponding elements in their structure. Spectrum (c) indicated incorporation of bromine, carbon and nitrogen to CTAB modified $TiO_2$ particles. This confirmed successful modification of $TiO_2$ nanoparticles by CTAB.

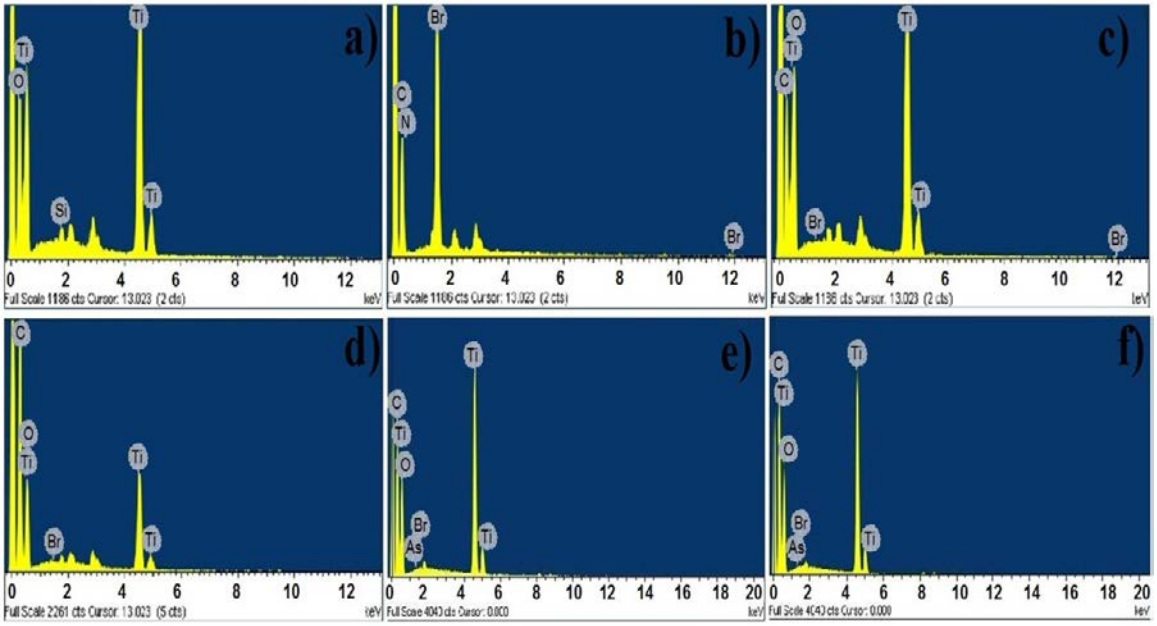


**Figure 3.3.3** EDX spectra of (a), UTi,(b) CTAB, (c), CMT,(d) SPC, (e) AMT and (f) ATC

The relative composition of carbon and oxygen was more in starch coated modified $TiO_2$ composites (d) compared to CTAB modified $TiO_2$ (c), suggesting participation of starch polymer into the system. Presence of arsenic in the spectra of both arsenic adsorbed CMT and SPC confirmed successful sorption of As(V) onto the systems. This further supported the findings of FT-IR data as discussed earlier (c).

*3.3.1.1.4 Thermogravimetric Analysis*

Thermograms for Starch, UMT, CMT and SPC are shown in Figure 3.3.4 (A). All the four samples exhibited their own distinctive TGA curves. The initial weight loss

observed in starch (a) and SPC (d) at around 100 °C was due to evaporation of small amount of moisture present in the samples.

The TGA curve for CMT [{Figure 3.3.4 A(c)}] showed some weight loss in the temperature range ~ 220 °C - 320 °C; UTi (b) had hardly shown any weight loss in that region. The weight loss in CMT was due to the incorporated CTAB on the surface of $TiO_2$ nanoparticles. Coating of CMT with Starch in SPC showed much more weight loss as compared to CMT. But at the same time, weight loss was less than the pristine polymer. This indicated that interaction had taken place between CMT and starch and starch was successfully coated over the surface of CMT. On the basis of weight loss, using equation 2.1, the percent $TiO_2$ loaded was found to be aprox. 25 %.

Since no two separate degradation patterns were observed for the TGA curve of Starch coated CMT nanoparticles (SPC), it indicated that the mixing of Starch and CMT nanoparticles did not form a blend. Rather, starch properly interacted with CMT nanoparticles.

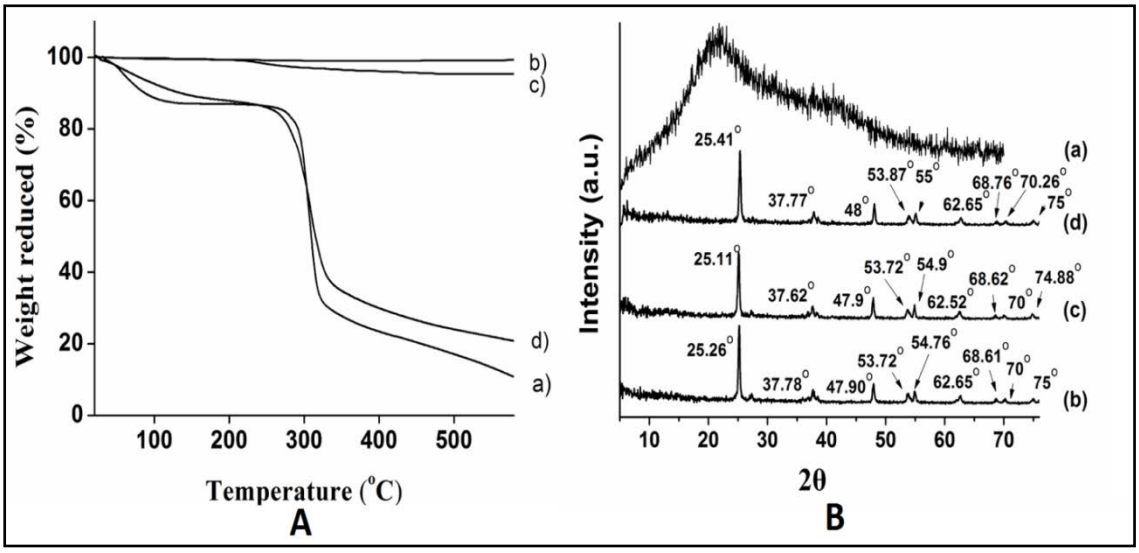


**Figure 3.3.4** A-TGA curves for (a) Starch, (b) UTi, (c) CMT,(d) SPC and B-XRD spectra of (a) Starch, (b) UTi, (c) CMT, (d)SPC

*3.3.1.1.5 XRD Study*

XRD spectra of UTi, CMT and SPC are shown in Figure 3.3.4 (B). The XRD patterns of UTi (b) exhibited strong diffraction peaks at approximately $2\theta=25^o$ (101), $37^o$ (111), $47^o$ (210), $53^o$ (211) and $55^o$ (220). The peaks occurred due to the crystalline portion of

$TiO_2$. Similar findings for $TiO_2$ were reported earlier [9, 10]. The diffraction peak at around 21° was for crystallinity of starch.

In the diffractogram of CMT (c) and SPC (d), no remarkable change in either peak positions/or peak intensity for $TiO_2$ crystals were observed. This suggested that the starch coating process did not result in any phase change of $TiO_2$ particles.

### *3.3.1.2 Batch Adsorption Experiment*

#### *3.3.1.2.1 Comparison of effectiveness of UTi, CMT and SPC*

Effectivity of UTi, starch, CMT and SPC materials towards As(V) removal from contaminated water was done. A targeted solution of 0.4 mg/L and material dose of 2 g/L was taken under consideration. Starch alone didn't produce any significant result. UTi, CMT and SPC showed good results as shown in Figure 3.3.5.

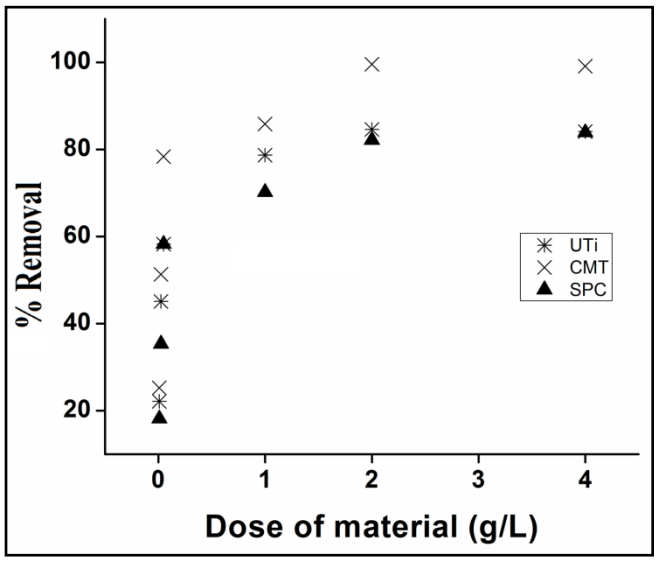


**Figure 3.3.5** Efficacy of UTi, CMT and SPC for As(V) removal

CTAB modified $TiO_2$ particles (CMT) exhibited better removal efficiency than unmodified $TiO_2$ particles (UTi) and brought down the arsenic concentration below 10 µg/L. CTAB prevented the aggregation of UTi particles and thus exposing more surfaces for interaction with arsenate ions in solution. But part of CMT entered into aqueous phase during the experiment causing a significant loss of the materials. This could be reduced by coating with crosslinked starch (SPC). Hence, both CMT and SPC were used in the subsequent experiments.

#### *3.3.1.2.2 Effect of Material Dosage on Removal Efficiency of As(V)*

The effect of material dose was studied by treating a laboratory prepared Arsenic(V) solution of known concentration with varying doses of CMT and SPC for about 5 h. Results are shown in Figure 3.3.6. Percent removal of As(V) was plotted as a function of material dosage. On increasing material dosage of CMT and SPC, percent removal of As(V) was observed to be increased.

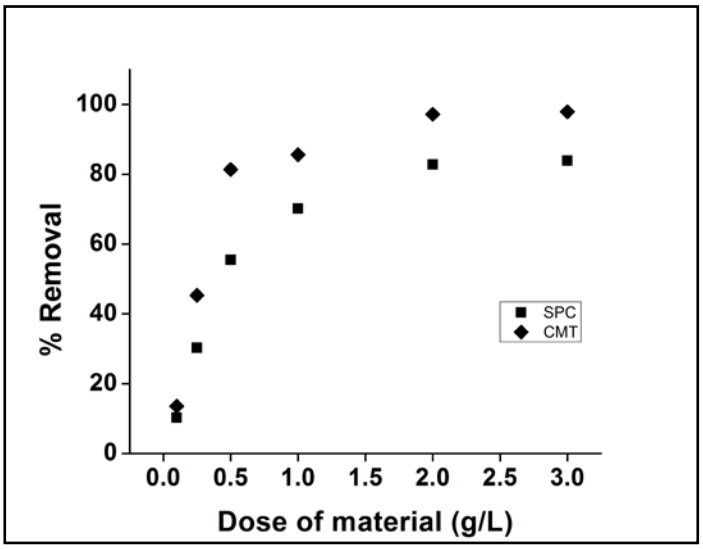


**Figure 3.3.6** Effect of material dose on As(V) removal

For a solution of concentration 0.4 mg/L, a dose of 2 g/L of CMT was sufficient to bring down the As(V) concentration below 10 µg/L. No prominent change was observed with the increase of material dosage thereafter. Therefore, the material dose was fixed at 2g/L for further study. Figure 3.3.6 showed that CMT had better efficiency compared to SPC towards As(V) removal. But reusability of CMT is a major problem as discussed later, whereas, starch coating is a good alternative.

*3.3.1.2.3 Influence of Agitation Time on As(V) Removal*

Figure 3.3.7 shows the effect of agitation time on percent removal of As(V) ion. From the figure, it was observed that with increase in treatment time, percent removal of As(V) increased, reached maximum (99% for CMT and 83 % for SPC) after 90 min treatment and after that remained almost constant throughout the time period studied. This might be due to the quick achievement of equilibrium between the arsenic adsorbed on the surface of sorbent and arsenic present in solution. Therefore, the agitation time was kept fixed at 90 min for the subsequent batch experiments.

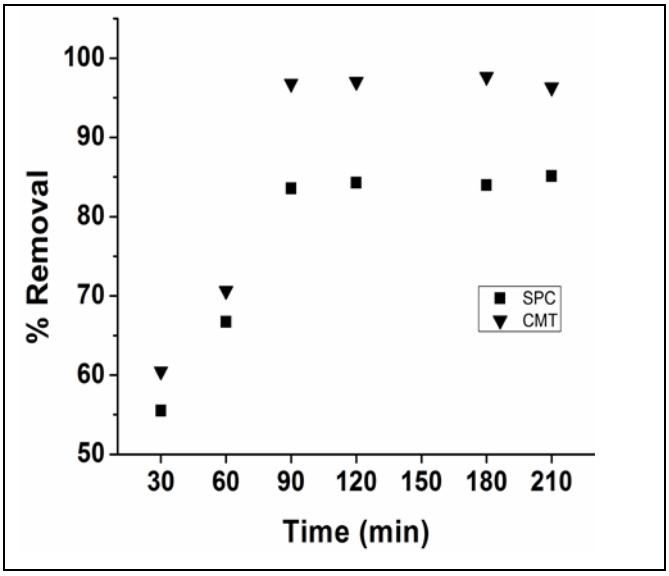


**Figure 3.3.7** Effect of treatment time on removal of As(V)

*3.3.1.2.4 Effect of Initial As(V) Concentration on Removal Efficiency*

The effect of initial Arsenic (V) ion concentration was studied in the concentration range 0.1 to 0.7 mg/L. Material dose and agitation time were kept fixed as optimized before. Figure 3.3.8 shows the effect of initial As(V) concentration on % removal of the ion. With the increase in metal ion concentration, the amount of metal ion uptake per unit weight of adsorbent (mg/g) had also increased.

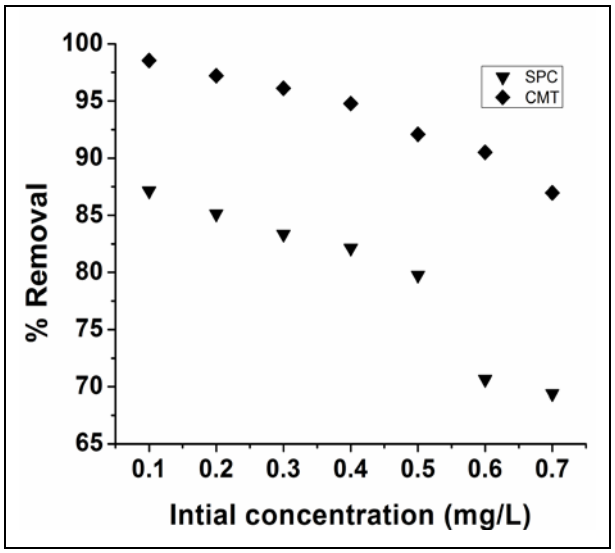


**Figure 3.3.8** Effect of initial ion concentration on removal rate of As(V)

It was observed that the percent removal of As(V) decreased with the increase in initial metal ion concentration. This might be attributed to the delayed establishment of equilibrium between the adsorbent sites and the As(V) ions due to increase in initial As(V) concentrations. The saturation of sorbent sites with the increase in initial ion concentration might also be the reason for diminished removal rate.

### *3.3.1.3 Kinetics of Adsorption*

Figure 3.3.9 (A) & (B) shows the variation of adsorbed amount (mg/g) of arsenate ions over time for different initial ion concentrations for SPC and CMT, respectively.

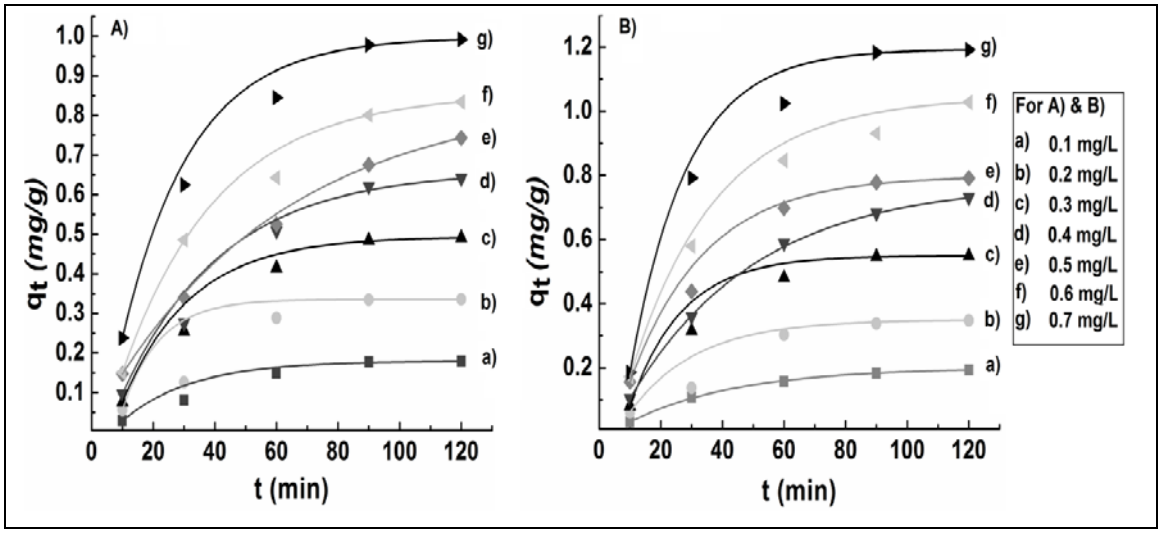


**Figure 3.3.9** $q_t$ vs t curve for sorption of As(V) for (A) SPC and (B) CMT

Additional plots of log ($q_e$-$q_t$) vs t, for the SPC and CMT gives straight lines from which different pseudo first order kinetic parameters were evaluated (Table 3.3.1).

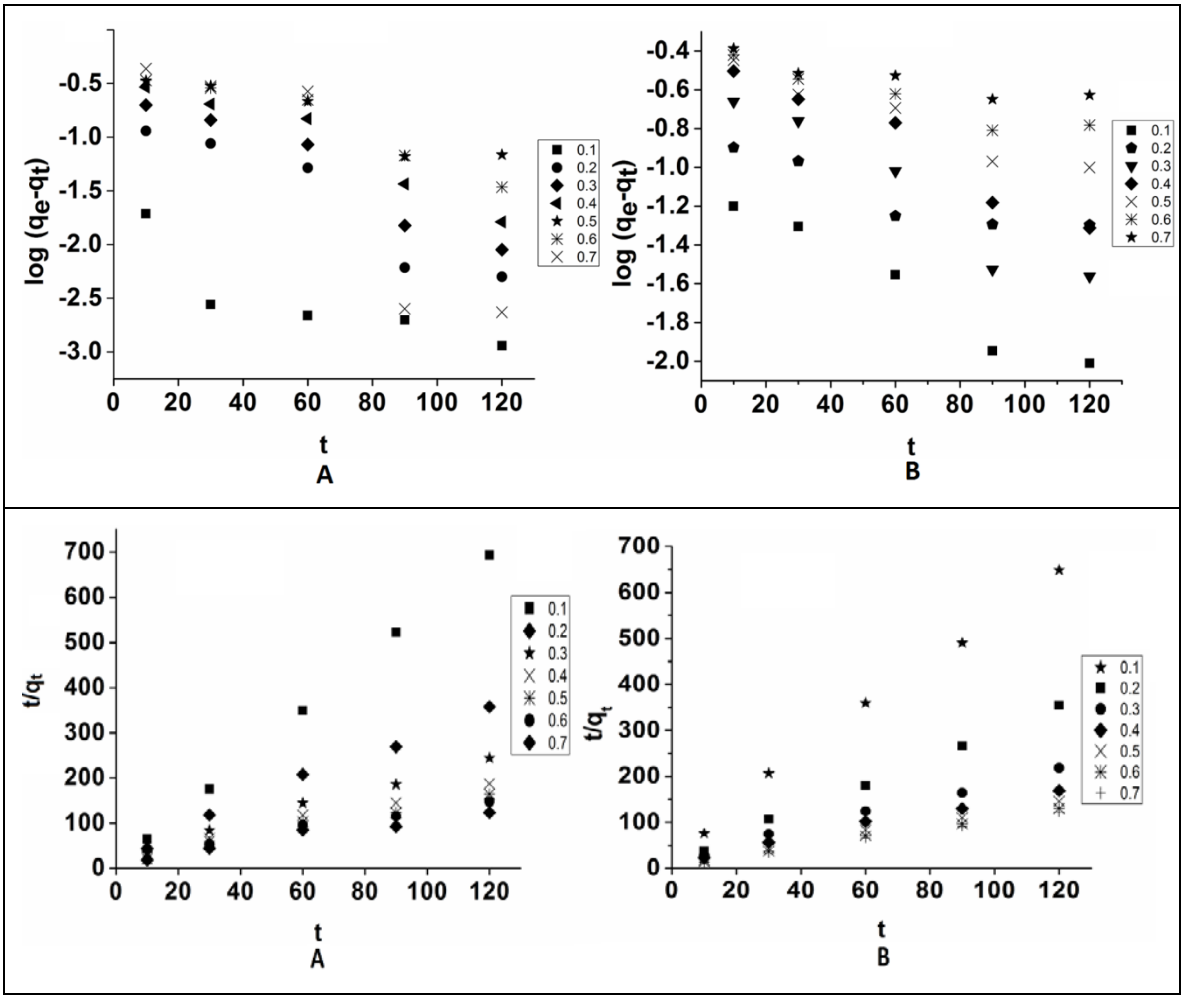


**Figure 3.3.10** First order (A-B) and second order (C-D) kinetic models for sorption of As(V) on SPC and CMT

**Table 3.3.1** First order Kinetic parameters for As(V) sorption

| $C_o$ (mg/L) | **M (g) | CMT | | | SPC | | |
|---|---|---|---|---|---|---|---|
| | | $K_{ad}$ (min$^{-1}$) | $q_e$(mg/g) | $R^2$ | $K_{ad}$ (min$^{-1}$) | $q_e$ (mg/g) | $R^2$ |
| 0.1 | 2 | 1.86 X10$^{-02}$ | 0.142 | 0.949 | 2.05 X10$^{-02}$ | 0.108 | 0.606 |
| 0.2 | 2 | 9.17 X10$^{-03}$ | 0.202 | 0.780 | 3.22 X10$^{-02}$ | 0.127 | 0.882 |
| 0.3 | 2 | 2.12X10$^{-02}$ | 0.335 | 0.923 | 3.05 X10$^{-02}$ | 0.298 | 0.932 |
| 0.4 | 2 | 1.78 X 10$^{-02}$ | 0.450 | 0.953 | 2.70 X10$^{-02}$ | 0.324 | 0.935 |
| 0.5 | 2 | 1.19 X 10$^{-02}$ | 0.487 | 0.924 | 1.69 X10$^{-02}$ | 0.455 | 0.851 |

| | | | | | | | |
|---|---|---|---|---|---|---|---|
| 0.6 | 2 | 8.04 X $10^{-03}$ | 0.528 | 0.869 | 2.18 X$10^{-02}$ | 0.483 | 0.909 |
| 0.7 | 2 | 4.93 X $10^{-03}$ | 0.630 | 0.773 | 5.51 X$10^{-02}$ | 0.541 | 0.768 |

*$C_o$: Initial concentration of As(V) solution

**M: Mass of CMT and SPC (adsorbent)

Similarly, different pseudo second order kinetics parameters were determined from the linear plot of $t/q_t$ vs $t$ {Figure 3.3.10 (A) and (B)}. The correlation coefficients ($R^2$) were computed and all the values are shown in Table 3.3.2. The $q_e$ values were found to increase with increase in initial As(V) concentrations. The curve for pseudo second order kinetics exhibited higher correlation co-efficient compared to pseudo first order model.

**Table 3.3.2** Second order kinetic parameters at different initial As(V) concentrations

| | | CMT | | | | SPC | | | |
|---|---|---|---|---|---|---|---|---|---|
| **#$C_\circ$ (mg/L)** | **##Mass (g)** | $q_e$ (mg/g) | K (g/mg min) | H (mg/g min) | $R^2$ | $q_e$ (mg/g) | K (g/mg min) | H (mg/g min) | $R^2$ |
| 0.1 | 2 | 0.196 | 0.633 | 0.025 | 0.995 | 0.174 | 6.221 | 0.189 | 0.999 |
| 0.2 | 2 | 0.354 | 0.568 | 0.071 | 0.998 | 0.362 | 0.271 | 0.035 | 0.990 |
| 0.3 | 2 | 0.597 | 0.154 | 0.055 | 0.992 | 0.538 | 0.148 | 0.043 | 0.988 |
| 0.4 | 2 | 0.767 | 0.112 | 0.066 | 0.988 | 0.707 | 0.094 | 0.047 | 0.980 |
| 0.5 | 2 | 0.868 | 0.148 | 0.112 | 0.995 | 0.809 | 0.085 | 0.056 | 0.971 |
| 0.6 | 2 | 0.962 | 0.197 | 0.182 | 0.997 | 0.889 | 0.076 | 0.059 | 0.968 |
| 0.7 | 2 | 1.010 | 0.297 | 0.304 | 0.998 | 1.091 | 0.052 | 0.062 | 0.945 |

# $C_o$: Initial concentration of As(V) solution

##Mass of CMT and SPC (adsorbent)

### *3.3.1.4 Adsorption Isotherm*

Figure 3.3.11 (a) & (b) shows the growth of adsorbed amount (mg/g) at equilibrium over the surface of SPC and CMT, respectively against increase in equilibrium concentrations. To establish the influence of As(V) concentration on the adsorption process, the equilibrium data had been analyzed by linear forms of Freundlich, Langmuir and Temkin model and are shown in Table 3.3.3.

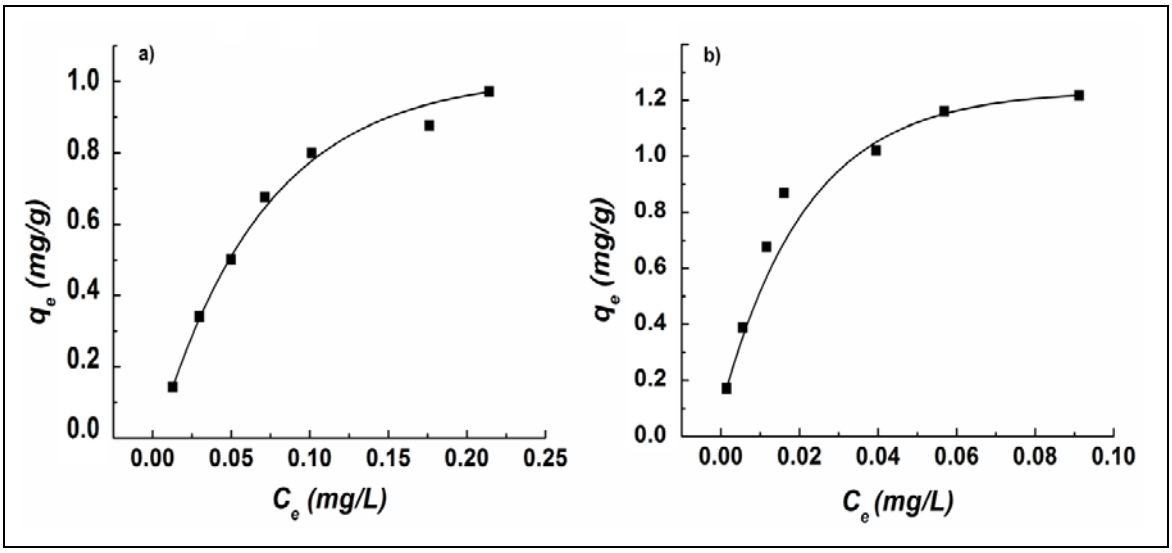


**Figure 3.3.11** $q_e$ vs $C_e$ curves for sorption of As(V) on a) SPC and b) CMT

The Langmuir parameters, viz. $q_m$, b and $R^2$ values were found to be 1.024 mg/g, $1.31X10^2$ and 0.989, respectively for SPC and 1.423 mg/g, 10.82 and 0.998, respectively for CMT. From Table 3.3.3, it was found that sorption was favorable for both the material as $R_L$ values (0.019 for SPC and 0.187 for CMT) occurred between 0 and 1 for each case. Also, $q_e$ vs $C_e$ showed linearity of the graph.

Freundlich parameters, $R^2$ and N values as shown in table 3.3.3, also indicated good fitting of sorption data with the model. The Temkin parameters were also derived and the co-relation coefficient ($R^2$~0.987, & 0.984) values showed that Temkin model could well explain the sorption pattern.

**Table 3.3.3** Sorption parameters of different isotherm models

| Model | Parameter | SPC | CMT |
|---|---|---|---|
| **Langmuir** | $q_m$(mg/g) | 1.024 | 1.423 |

| | | | |
|---|---|---|---|
| | b (L/mg) | 131 | 10.82 |
| | $R^2$ | 0.989 | 0.998 |
| | $R_L$ | 0.019 | 0.187 |
| **Freundlich** | $K_f$ (mg/g) | 2.854 | 2.751 |
| | N | 2.557 | 1.666 |
| | $R^2$ | 0.931 | 0.944 |
| **Temkin** | $A_T$ (L/g) | $1.28 \times 10^3$ | $1.28 \times 10^2$ |
| | B (J g/mg$^2$) | $1.13 \times 10^4$ | $8.62 \times 10^3$ |
| | $R^2$ | 0.987 | 0.974 |

It was observed that $R^2$ values for all the models showed good co-relations of data. Thus, the sorption could be reasonably explained by all the models under consideration. The preferential order for sorption, among these models is as follows- Langmuir >Temkin >Freundlich. High positive value of Temkin constant $b_T$ signifies that the changing energy during the adsorption is positive, that means it is an exothermic process.

A comparative study of the efficiency of the materials with some reported materials is presented in Table 3.3.4 suspension of $TiO_2$ was found to be good adsorbent for As(III) and As(V). But the sopriton was dependent on pH, depening upon the arsenic speciation [11]. A hydrous titanium dioxide nanoparticle was also reported to show very high adsorption capacity as presented in the table. The material was successfully utilized in laboratory prepared as well as naturally contaminated arsenic water [12]. But, in both the cases, neither author has mentioned anything about the reusability nor leaching of the sorbent material thus limiting the practical applicabitliy of the material. Materials under present investigation showed very good results (although very low initial arsenic concentrations were taken relative to the compared reports) and cyclic run was also carried out for several times.

**Table 3.3.4** Comparison of efficiency with other established material

| Material | Arsenic species | $q_e$ (mg/g) | Remark |
|---|---|---|---|
| $TiO_2$ suspension [11] | As(V), As(III) | - | Efficeiny was pH dependent |
| Hydrous titanium dioxide [12] | As(III) | 83.9 | Regeration is missing |
| SPC | As(V) | 1.024 | Reclyable, works at normnal pH |
| CMT | As(V) | 1.423 | |

### *3.3.1.5 Resusability Test*

Regeneration experiments were carried out four times for both CMT and SPC. Each time the treated samples were treated with 0.1 M HCl solution for desorption of the adsorbed As(V). The results are shown in Figure 3.3.12 (a). As observed from the figure, CMT showed better As(V) removal efficiency than SPC under identical conditions.

The weight loss (%) after each time of reuse was also calculated for both CMT and SPC. It was found that the percent weight loss (%) of SPC was less [{Figure 3.3.12 (b)}] as compared to CMT. This implied successful stabilization of CMT particles inside the starch matrix resulting in a decreased leaching rate. Use of crosslinking agent also might have some contribution for observing lower weight loss in the case of SPC.

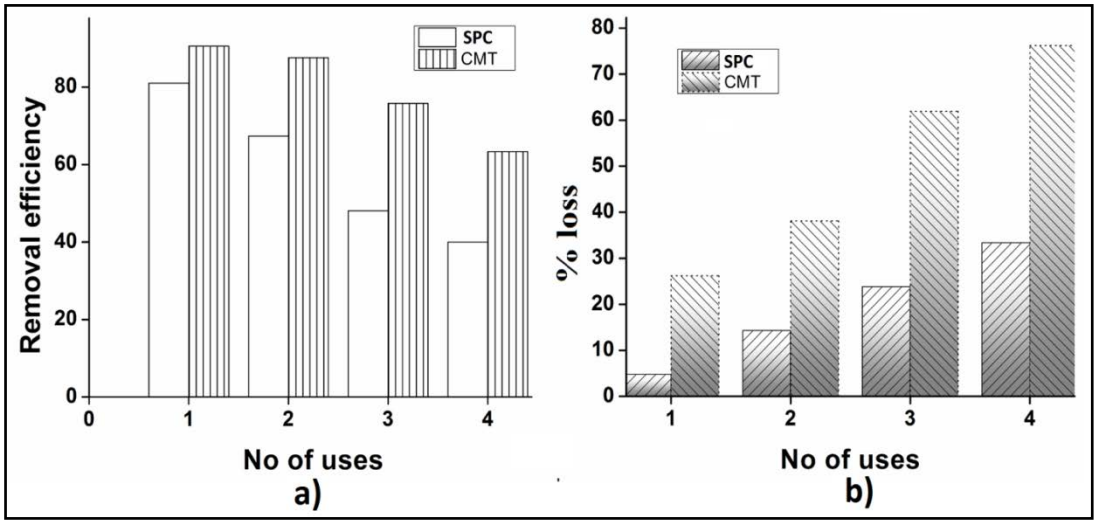


**Figure 3.3.12** Comparison of a) reusability, b) weight left for CMT and SPC after reuse

### *3.3.1.6 Effect of Competition Ions on Removal Rate*

The effect of competition ions, viz. phosphate and sulphate on arsenate removal rate by CMT in synthetic water was investigated. Figure 3.3.13 shows the variation of sorption rate of arsenate ions with elevated concentration of phosphate and sulphate ions. The experiments were carried out with prepared solutions containing arsenate/phosphate and arsenate/sulphate ions at neutral pH. The change in removal rate was monitored with elevated concentration of phosphate and sulphate ions in two separate experiments.

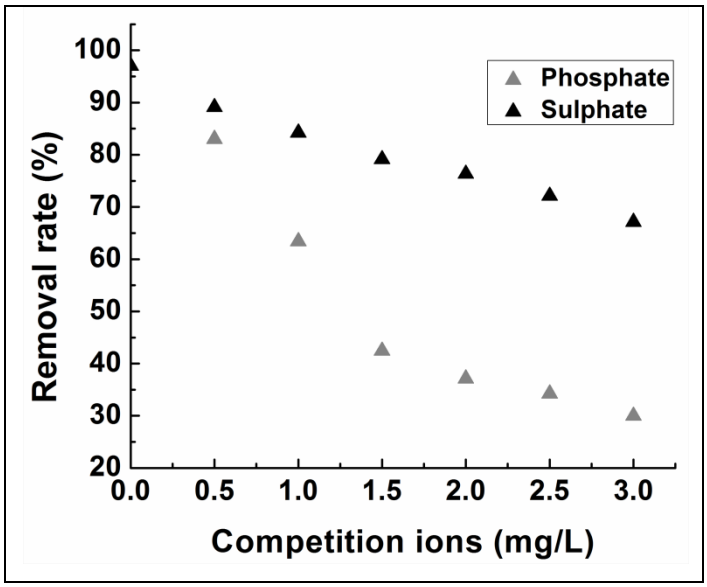


**Figure 3.3.13** Effect of $PO_4^{3-}$ and $SO_4^{2-}$ on Removal of As(V) by SPC

With the increase in their respective concentrations, both phosphate and sulphate ions were found to notably reduce the removal rate of arsenate. This might be due to the similarity in chemistry of As(V) with phosphate and sulphate in aqueous solution at neutral pH. The effect of phosphate ion was more pronounced compared to that of sulphate ion. The resemblance of ionization constants and ionic structure of phosphate with arsenate was responsible for this anomaly [13].

## 3.4 Designing a New Hybrid of Starch, OMMT clay and Iron-oxyhydroxide for Arsenite Adsorption: A Mechanistic Approach

This part of the study demonstrated the state of art material based on amminated starch, oxyhydroxide of iron and OMMT clay and its performance in remediation of hazardous trivalent arsenic [As(III)] from water.

One of the cutting edge technologies developed by researchers to remove arsenic or other heavy metals from water is Fe(III) based sorbents. They have strong affinity and selectivity towards arsenic species, which include magnetite, siderite, hematite amorphous hydrated Fe(III) oxide, ferrihydrite, etc. [14]. Iron oxyhydroxide is one of the iron (III) compound which has outstanding capability to adsorb both As(III) and As(V) species [15, 16]. Cumbal and Sengupta have reported very good removal effciency of Arsenic over Polymer-Supported Hydrated Iron(III) Oxide Nanoparticles. The hybrid sorbent that utilizes the Donnan membrane effect of the host material for sorption enhancement was reported to be the first of that kind [16]. Acitivated carbon with iron oxyhydroxide was found to be efficient adsorber of arsenic, but soprtion capacity was not so high [15]. In a study Tresintsi et al. have established the significant role played by ion exchange due to $SO_4^{2-}$ ions present at the surface of iron oxyhydroxide (prepared from $FeSO_4$), in acidic medium along with formation of monodentate and bidentate inner sphere complexes for sorption of As(V). On the other hand Sorption of As(III) was explained as due to Lewis acid-base ligand-exchange reaction preferably onto non-ionized surface functional groups on basis of performance of the material with different arsenic concentrations. Along with very high adsorption capacity it could bring down the residual arsenic below 10 mg/L and maintaining its superiority in column tests compared to number of commercial granular materials [17].

On the other hand, arsenic mitigation by clay minerals and their modified forms are also well reported [18]. But clay minerals are more effective in the case of heavy metals which are positively charged only. Surfactant modification converts clay surface from negatively charged to a positively charged one, and thus organoclay becomes a potential sorbent of negatively charged arsenic species from aqueous solution also.

However, to avoid free release of nanoparticles to the environment (which may pose another potential threat to human health) and prevent their agglomeration, stabilization of the nanomaterials by dispersing them on host materials such as granular activated carbon, cellulose and polymeric materials, etc. is necessary. Use of these nanomaterials together may further improve the sorption ability along with their

stability under experimental conditions [19]. Starch in its pristine form may not be suitable for immobilization of the nanomaterials. Amination of starch enhances its binding ability which also contributes to arsenic sorption. Grafting with Glycidyl methacrylate may be an efficient technique to introduce amine functionality through ethylene diamine to starch backbone.

Therefore, the present work aimed at preparing a nanocomposite of clay and amminated starch stabilized with oxyhydroxide and evaluating its efficiency for successful remediation of trivalent arsenic from aqueous solution. A model describing the sorption mechanism was also demonstrated on the basis of Density Functional theory

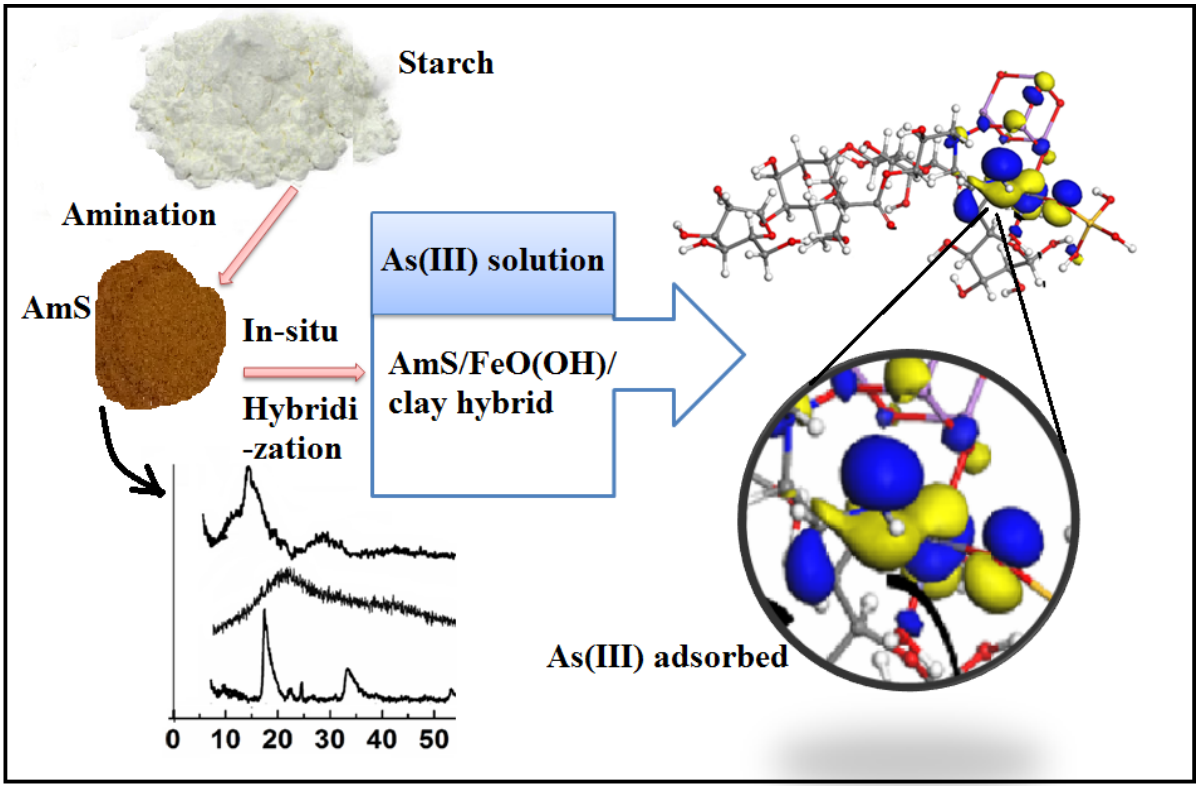


**Scheme 3.4.1** Iron oxyhydroxide crosslinked starch-clay nanocomposite, preparation and application in arsenic remediation

### 3.4.1 Results and Discussion

#### *3.4.1.1 Characterization*

*3.4.1.1.1. FTIR Analysis*

Figure 3.4.1 (a-g) represent the FTIR spectra of starch, St-g-GMA, AmS, nanoclay (OMMT), SIC, SICC and ATC, respectively. Bands near 3380-3450 $cm^{-1}$ and

**Table 3.4.0** Composition of different sorbent materials

| Sample | AmS | FeOOH | SIC | Clay |
|---|---|---|---|---|
| SIC | 100 | 114 | - | - |
| SICC/5 | - | - | 100 | 5 |
| SICC/10 | - | - | 100 | 10 |
| SICC/20 | - | - | 100 | 20 |

2930 $cm^{-1}$ occurred in most of the cases were due to –OH and $–CH_2$ stretching vibration, respectively. In case of starch (a) band at 3410 $cm^{-1}$ corresponding to –OH stretching was a broad one indicating the existence of large number hydrogen bonding among the hydroxyl groups. Band near 1656 $cm^{-1}$ was due to –OH bending mode of vibration. The two bands in the region 1170 and 1004 $cm^{-1}$ could be assigned to C-O bond stretching of C-O-H group [5].

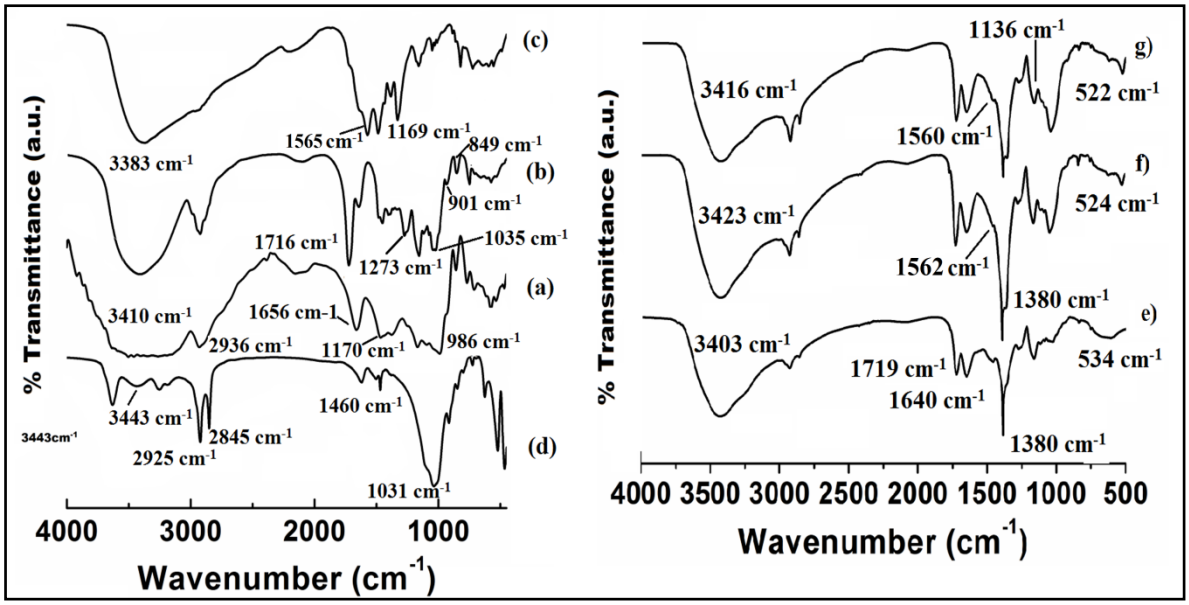


**Figure 3.4.1** FTIR spectra of (a) starch, (b)St-g-GMA, (c) AmS, (d) nanoclay(OMMT), (e) SIC, (f) SICC and (g) ATC

Grafting with GMA (b) resulted into sharpening of the band due to –OH stretching. This might be due to break down of many hydrogen bonded sites during the grafting process. Also, the grafting was accompanied by formation new bands near 1716 $cm^{-1}$ and1035 $cm^{-1}$which could be assigned for C=O and C-O stretching mode of vibrations, respectively, of newly inserted ester groups into the system. The characteristic band around 1273 $cm^{-1}$ was due to epoxy group [20]. The strong broad band appeared at 3383 $cm^{-1}$ (curve c) after amination was mainly due to the -NH stretching vibration (overlapped by OH). The new peaks at 1565 $cm^{-1}$ for the -NH bending vibration, and at 1169 $cm^{-1}$ for the -CN stretching vibration had also supported the existence of amine groups on AmS [21]. Again disappearance of band near 1273 $cm^{-1}$ after amination was due to open up of the epoxy ring during EDA binding to St-g-GMA moiety. In the IR spectrum of OMMT (d), bands appeared at 3443 $cm^{-1}$, 2925

$cm^{-1}$ and 2845 $cm^{-1}$ and 1460 $cm^{-1}$ were for O-H stretching, C-H stretchingand N-H stretching, respectively [22].

Incorporation of oxyhydroxide moiety into the aminated starch to produce SIC (curve e) showed two bands near 1640 $cm^{-1}$ and 1380 $cm^{-1}$ due to the stretching of -COOFe group. Another band appeared at 534 $cm^{-1}$ was due to stretching vibration of Fe-O [21]. Moreover, the shifting of band corresponding to hydroxyl group slightly towards lower wavenumber and decreased in intensity of amine group indicated probable involvement of those groups in binding process.

After incorporation of OMMT clay to produce SICC (curve-f), intensity of bands corresponding to hydroxyl and amine were further decreased which were initially present in both the component materials, clay and SIC, respectively. Also a new band near 1031 $cm^{-1}$ appeared in SICC which could be attributed due to Si-O bond of the clay. The curve-(g) shows the spectrum of arsenic treated SICC nanocomposite. The decrease in intensity and slight shifting of bands near 1560 $cm^{-1}$ and 1136 $cm^{-1}$ after treatment with As(III) indicted the probable interaction of it at surface of sorbent material [23].

The initial structures of the complexes were modeled on the basis of experimentally derived structural information. The DFT optimized geometries of the reactants arsenate oxide, arsenate hydroxide, GMA and starch (Figure 3.4.2 a-d), St-g-GMA, AmS, SICC{Figure 3.4.2 (e-g)} and the linkage of cross-linked compounds with arsenates are shown in Figure 3.4.2 (h) and (i). The vibrational frequencies derived from the DFT optimized geometries are shown in Table 3.4.1 and were found to be in good agreement with the experimental results. The geometrical parameters showing the interaction of oxides of arsenic with those of complex are shown in Figure 3.4.2.

**Table 3.4.1** Experimental and theoretical infrared spectral data for the optimized complexes, ν is the vibrational frequency in $cm^{-1}$

| Assignment | | Frequency ($cm^{-1}$) | Assignment | | Frequency ($cm^{-1}$) |
|---|---|---|---|---|---|
| **GMA_*1(c)*** | | | **SICC_*1(g)*** | | |
| ν(C-O) *epoxy* | Exp. | 1275.0-1255 | ν(As-O) | Exp. | 522.0 |
| | Calc. | 1280.9 | | Calc. | 642.9 |
| ν(C=C) *aliphatic* | Exp. | 1620.0–1680.0 | ν(Fe-O) | Exp. | 524.0 |
| | Calc. | 1670.3 | | Calc. | 580.5 |
| **St-g-GMA_*1(e)*** | | | **SICC-** | | |

| | | | | | |
|---|---|---|---|---|---|
| | | | **$As_4O_6$_*1(h)*** | | |
| ν(C-O) *epoxy* | Exp. | 1272.0 | ν(N-H) *amine* | Exp. | 1560.0 |
| | Calc. | 1282.0 | | Calc. | 1523.4 |
| $\nu(C=C)_{aliphatic}$ | Exp. | -- | ν(O-H) *Fe-water* | Exp. | 1630.0 |
| | Calc. | -- | | Calc. | 1694.1 |
| ν(C-O) *ester* | Exp. | 1035.0 | ν(As-O) | Exp. | 522.0 |
| | Calc. | 1035.2 | | Calc. | 591.8.0 |
| ν(C=O) *carbonyl* | Exp. | 1716.0 | ν(Fe-O) | Exp. | 524 |
| | Calc. | 1762.3 | | Calc. | 530.4 |
| **AmS_*1(f)*** | | | **SICC-$AsO_3H_3$_*1(i)*** | | |
| ν(C-O) *epoxy* | Exp. | 840.0–950.0 | ν(N-H) *amine* | Exp. | 1562.0 |
| | Calc. | -- | | Calc. | 1581.8 |
| ν(C-O) *ether* | Exp. | 1035.0 | ν(O-H) *Fe-water* | Exp. | 1630.0 |
| | Calc. | 1027.6 | | Calc. | 1636.9 |
| ν(N-H) *amine* | Exp. | 1565.0 | ν(As-O) | Exp. | 522.0 |
| | Calc. | 1572.9 | | Calc. | 598.5 |
| ν(C-N) *amine* | Exp. | 1163.0 | ν(Fe-O) | Exp. | 524 |
| | Calc. | 1163.3 | | Calc. | 549.2 |
| **SICC_*1(g)*** | | | | | |
| ν(N-H) *amine* | Exp. | 1562.0 | | | |
| | Calc. | 1599.6 | | | |
| ν(O-H) *Fe-water* | Exp. | 1630.0 | | | |
| | Calc. | 1643.2 | | | |

**Table 3.4.2** Values of geometrical parameters (Å) having *d* as bond length.

| Geometric parameters | Values | Geometric parameters | Values |
|---|---|---|---|
| **GMA_*1(c)*** | | **SICC_*1(g)*** | |
| $d_{C—O}$ | 1.437–1.441[a] | $d_{N—H}$ | 1.018–1.028[d] |
| $d_{C—O}$ | 1.367–1.447[b] | $d_{C—N}$ | 1.419–1.426[d] |
| $d_{C=O}$ | 1.220 | $d_{O—H}$ | 0.995–1.012[e] |
| $d_{C=C}$ | 1.340 | $d_{Fe—O}$ | 1.834–2.027 |
| **St-g-GMA_*1(e)*** | | $d_{Fe—N}$ | 1.768 |
| $d_{C—O}$ | 1. 347–1.446[a] | **SICC-$As_4O_6$_1(h)** | |
| $d_{C—O}$ | 1.353–1.455[b] | $d_{N—H}$ | 1.025–1.038 |
| $d_{C=O}$ | 1.221 | $d_{C—N}$ | 1.428–1.464 |
| $d_{C—C}$ | 1.519 | $d_{O—H}$ | 0.983–1.016 |
| **AmS_*1(f)*** | | $d_{Fe—O}$ | 1.833–2.016 |
| $d_{C—O}$ | 1.347–1.446[b] | $d_{Fe—N}$ | 1.761 |
| $d_{C—O}$ | 1.429[c] | **SICC-$AsO_3H_3$_1(i)** | |
| $d_{N—H}$ | 1.020–1.022 | $d_{N—H}$ | 1.029–1.030 |
| $d_{C—N}$ | 1.457–1.463 | $d_{C—N}$ | 1.404–1.441 |
| | | $d_{O—H}$ | 0.987–1.020 |
| | | $d_{Fe—O}$ | 1.838–2.013 |
| | | $d_{Fe—N}$ | 1.756 |

[a]: CO bond length of epoxy group

[b]: CO bond length ofC-O-C group
[c]: CO bond length changes as epoxide group opened up to form C-OH and C-H
[d]: NH and CN bonds of amine group
[e]: OH bond lengths of $H_2O$ of the octahedral Fe-atom

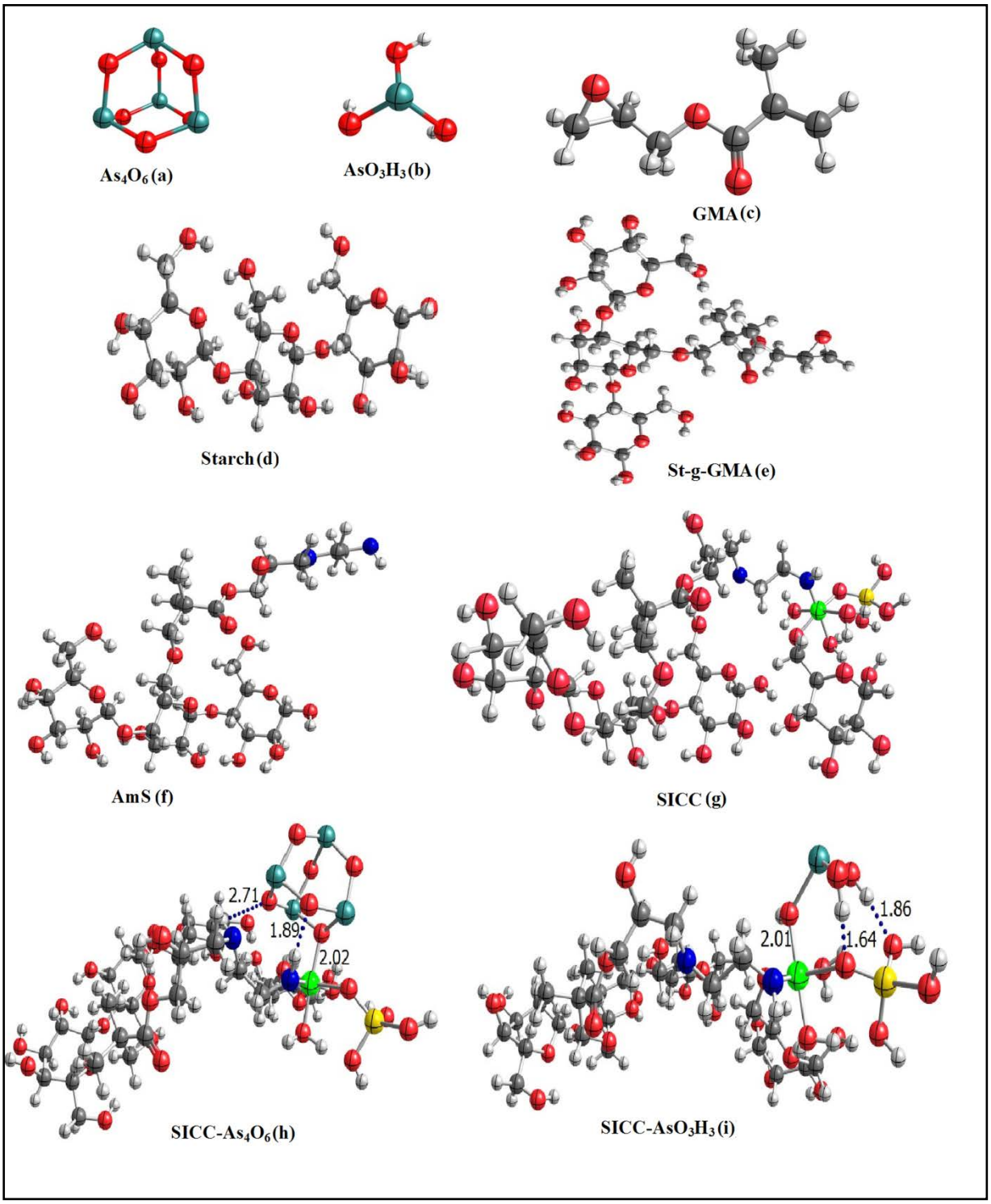


**Figure 3.4.2** Optimized geometries for different reactants and complexes.

For complex SICC-$As_4O_6$ (h) which was formed by the sorption of $As_4O_6$ (a) on SICC (g), the N-H and C-N bond was found to be elongated after arsenic sorption, whereas, the length for other groups like O-H, Fe-O and Fe-N, remain unchanged (table 3.4.2). This was further confirmed by the decrease in vibrational frequencies (from Table 3.4.1) of N-H and C-N bonds after arsenic binding, as less energy is required for vibration of a weak bond. The solid and dotted lines represent the formation of bonding between the atoms. Confirming that the sorption of As(III) has caused some changes in the geometry of the complex for those atoms in which direct interaction has taken place.

For complex SICC-$AsO_3H_3$ (i), formed by sorption of $AsO_3H_3$ (b) on SICC 1(g), there is elongation in the bond lengths of N-H and Fe-O groups, however, shortening of bond is taking place for groups: C-N, O-H and Fe-N. This is also in agreement with the decrease in vibrational frequency for N-H and Fe-O groups, i.e. a weak bond could be vibrated by a lower amount of energy. Also bond properties (bond length, vibrational frequecies) derived from the optimized geometries for arsenic adsorbed materials were found in the chemisorption range.

*3.4.1.1.2. Thermogravimetric Analysis*

The thermograms for St-g-GMA, AmS, SIC and SICC (10% clay loading) are shown in the figure below. The initial weight loss observed in St-g-GMA (a) at around

100 $^oC$ was due to evaporation of small amount of water present in the sample. It was stable upto 300 $^oC$. This indicated an improvement in thermal stability due to the grafting. Thereafter, a continuous weight loss occurred above this temperature till 440 $^oC$ where a weight loss of about 90% occurred. This might be due to the presence of some low molecular weight compounds or due to the presence of some unreacted monomer in it.

The aminated starch (AmS) showed a continuous weight loss (b) from the beginning upto 440 $^oC$ due to decomposition of the uncrosslinked biopolymer. For SIC (c), the initial weight loss at 100$^oC$ was due to the presence of moisture.The major degradation took place from 190 $^oC$ and ultimately a weight loss of about 70% occurred at 500 °C. The TGA curve of the SICC with varying amount of nanoclay loading (5%, 10% and 20%) are shown in Figure 3.4.3 (d,e & f). With increase in amount of MMT,

thermal stability was found to increase up to the loading of 10 % MMT, then thermal stability decreased again. This could be due to agglomeration of nanoclay within the matrix as a result of clay overloading. Enhanced thermal properties on loading with clay indicated that quite good interactions were taking place among the components in molecular level.

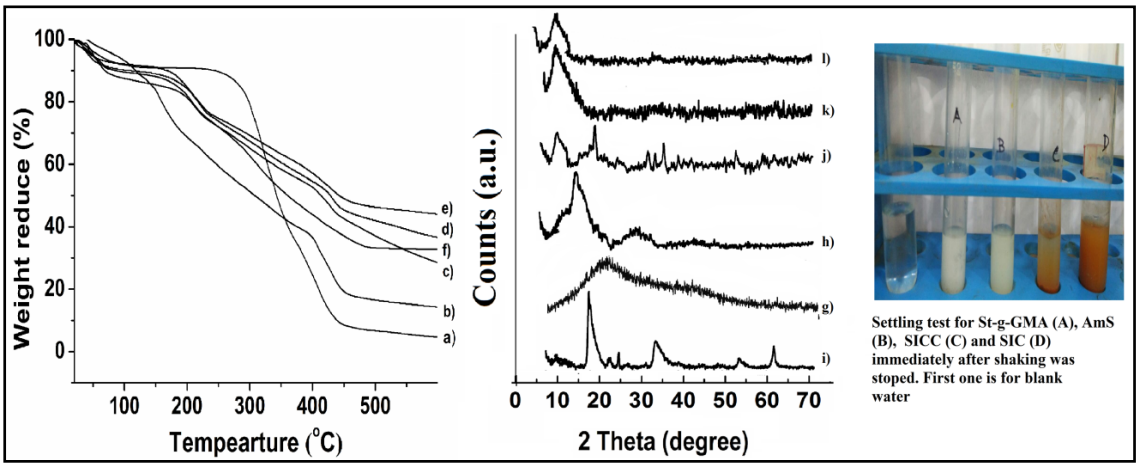


**Figure 3.4.3** TGA curves of (a) St-g-GMA, (b) AmS, (c) SIC, (d) SICC/5 e) SICC/10, f) SICC/20 and XRD spectra for g) starch (h) Ams, (i) OMMT, (j) iron oxyhydroxide (k) SIC and (l) SICC/10.

*3.4.1.1.3. XRD Study*

The characteristic peak for starch biopolymer was found to appear at $2\theta=23^{o}$ [24]. Grafting with GMA resulted into disappearance of the peak at $2\theta=23^{o}$ of starch indicating loss in crystallinity of it due to side chain grafted structure and appearance of two new peaks appeared at $2\theta=17$ and $30^{o}$. The appearance of these peaks might be due to rearrangement of poly Glycidyl methacrylate unit formed during the grafting process [25]. In the spectrum for iron oxyhydroxide (curve-j), characteristic peaks appeared at $2\theta=20.5$, 34, 36.4, 40.2, 50.2, 52, 59.3 and $61.4^{o}$ confirming the successful formation of oxyhydroxide [26]. When oxyhydroxide was incorporated into grafted starch, the intensity of characteristic peaks of the former was greatly reduced due to loss in crystallinity. In the XRD pattern of OMMT (curve-i) characteristic peaks could be seen at $2\theta=20^{o}$ and $37^{o}$ [27 28]. In SICC (curve-l), the disappearance of the characteristic peaks of OMMT indicated that either the clay layers became fully exfoliated or delaminated.

*3.4.1.1.4 SEM/EDX Analysis*

Figure 3.4.4 (a-e) shows the SEM images of St-g-GMA, AmS, SIC, SICC and ATC, respectively. Starch particles after being grafted were visibly separated from one another and agglomeration did not take place. In the aminated starch (b) little bit agglomeration of particles took place which might be attributed to the formation of more hydrogen bonding introduced into the system via amine functionality.

The micrograph of SIC (c) shows the formation of more agglomerated structures. The agglomeration of particles occurred due to the crosslinking through oxyhydroxide moieties and some voids were also generated at the surface. In the final nanocomposite (curve-d), the surface appeared smoother and voids were partially filled as compared to that of SIC (curve-c) due to the presence of clay particles. Incorporation of nanoclay was responsible for such observations. Again, careful notice of surface morphology of the As(III) treated nanocomposite showed some small particles present on the surface and the latter became comparatively smoother. This might be an indication of successful adsorption of As(III).

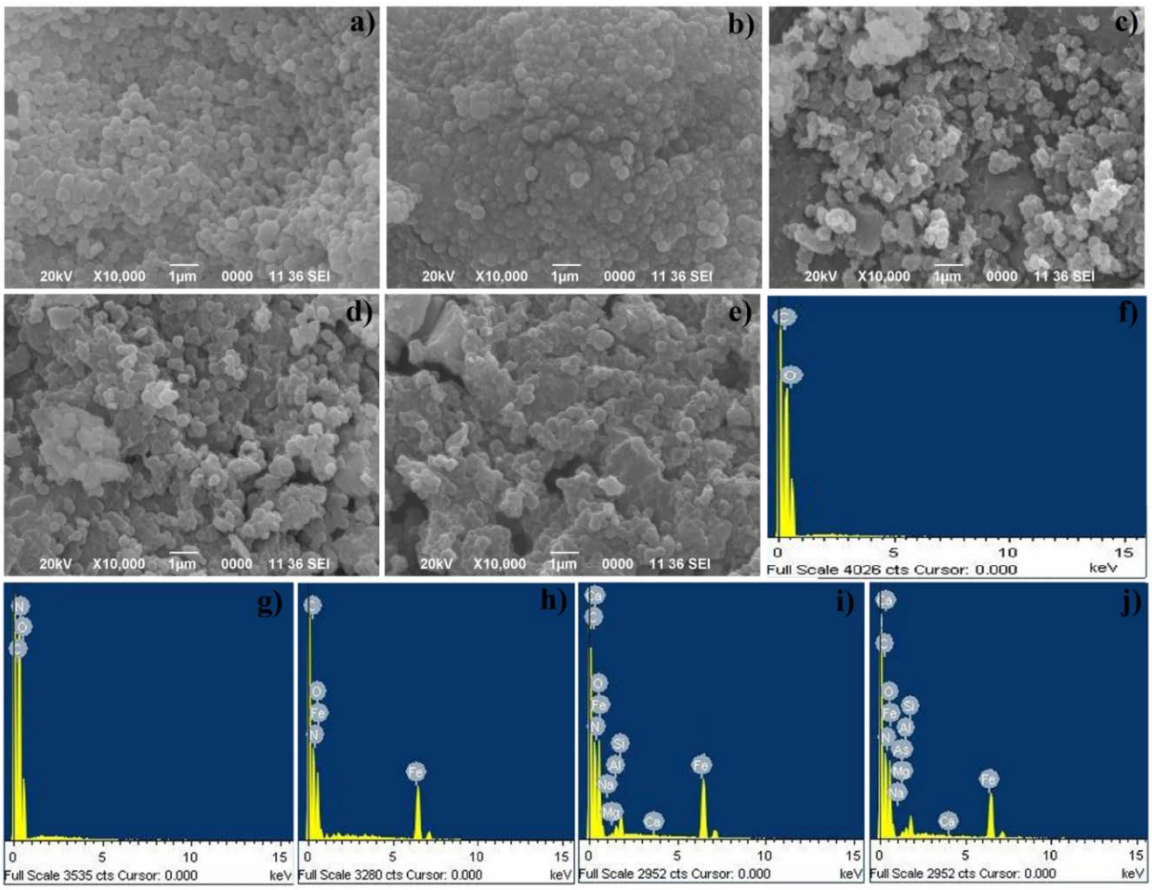


**Figure 3.4.4** (a-e) SEM images and (f-j) EDX spectra of St-g-GMA, AmS, SIC, SICC and ATC

Figure 3.4.4 (f-j) represents the EDX spectra of St-g-GMA, AmS, SIC, SICC and ATC, respectively. From the EDX spectrum of St-g-GMA, only the presence of carbon and oxygen was detected. The elemental compositions after reacting with ethylene diamine as represented by Figure 3.4.4 (g), included nitrogen along with oxygen and carbon. Presence of nitrogen along with other elements present in St-g-GMA indicated that amine functionality was successfully introduced into the system. Spectrum of SIC (h) showed additional elemental iron, which could be due to the incorporation of oxyhydroxide. Presence of iron, silicon, aluminium, sodium and magnesium in the EDX spectrum of SICC was due to OMMT (nanoclay). In the last spectrum (curve j) the presence of arsenic was observed indicating sorption of As(III) on the surface of the material.

### *3.4.1.2 Evaluation of Efficiency of Prepared Materials for As(III) Remediation*

*3.4.1.2.1 Comparison of Efficiency of Different Materials*

The different materials were tested with an As(III) solution containing 4 mg/L to evaluate their efficacy for As(III) remediation and the settling time of the materials after treatment was monitored. It was found that the removal efficiency of Oxyhydroxide and SIC was quite good as shown in table 3.4.3, which enhanced further on incorporation of clay into the system. Also, the increase in clay loading enhanced the removal rate except for 20% clay loading. The discrepancy in the later case might be due to less availability of active clay surface because of their agglomeration. The removal rate of As(III) from its solution by oxyhydroxide was significant but the solution remained turbid for a long time due to the presence of some suspended particles. Clay alone merely showed any As(III) removal. But its incorporation into SIC enhanced the removal rate due to synergistic influence of the component materials and as a result of which the sorption sites in the component materials might get exposed of. On the basis of these observations SICC with 10% clay loading was considered for further investigations. Initially a high concentration (4 mg/L) of As(III) was taken to find out the most efficient material so that it can be implemented in subsequent applications.

**Table 3.4.3** Performance of different materials in As(III) remediation

| Material | BT (mg/L) | AT (mg/L) | Removal rate (%) | Solution colour after treatment |
|---|---|---|---|---|
| Starch | 4 | - | Not significant | - |
| Clay | 4 | - | Not significant | - |
| Iron Oxyhydroxide | 4 | 0.521 | 87 | Turbid |
| SIC | 4 | 0.499 | 87.5 | Clear |
| SICC/5 | 4 | 0.251 | 93.7 | Clear |
| SICC/10 | 4 | 0.162 | 96.0 | Clear |
| SICC/20 | 4 | 0.122 | 91.0 | Clear |

*BT: Before treatment

*AT: After treatment

*3.4.1.2.2. Effect of Material Dose on Removal Rate*

Influence of material dose on removal efficiency of trivalent arsenic was studied by using material doses in the range 0.25-3 g/L. The initial concentration of solution and the treatment time were kept as 0.5 mg/L As(III) and 2 h, respectively. From the

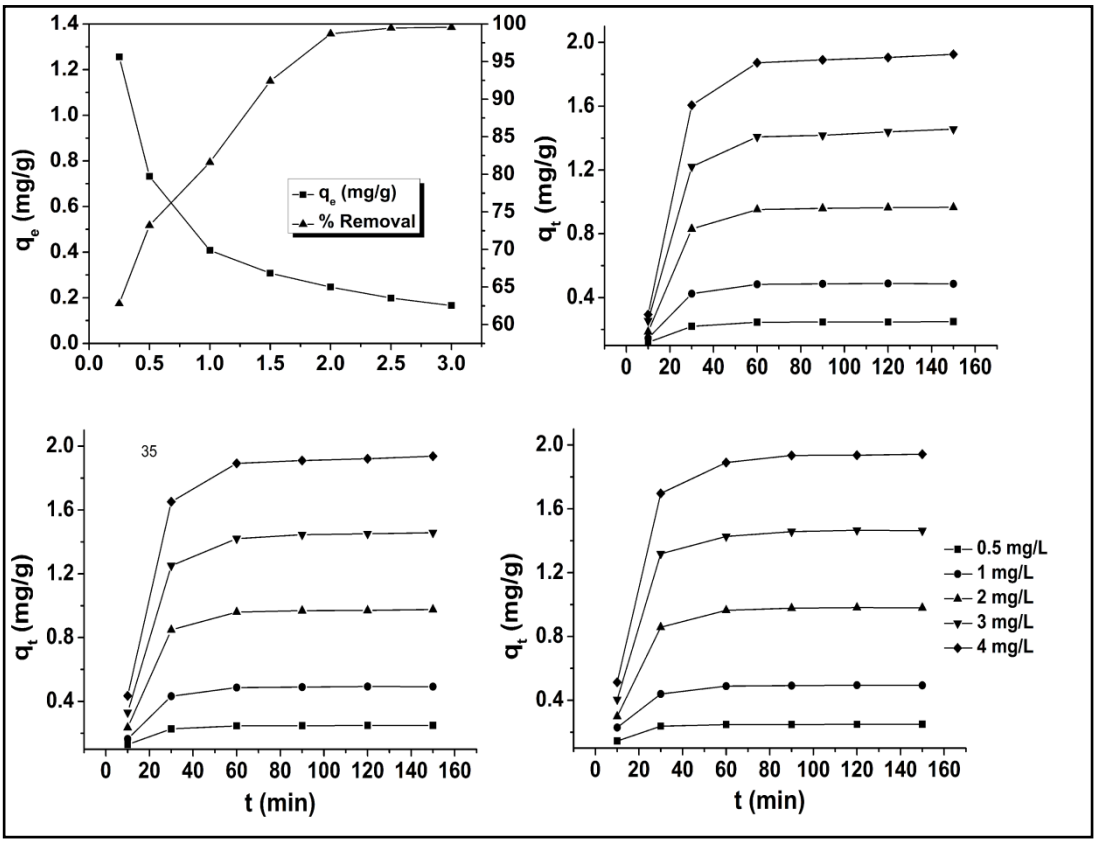


**Figure 3.4.5** Effect of material dose (a) treatment time and initial arsenic concentration at 303, 308 and 313 K (b-d) on removal efficiency of As(III)

Figure 3.4.5, it could be seen that the removal rate of arsenite increased with the increase in material dose and a material dose of 2 g/L could bring down the As(III) concentration below 10 µg/L. The increase in removal rate with the increase in the amount of material dose was due to availability of more sorption sites. But after certain material dose, the concentration gradient of As(III) between adsorbed surface of the material and that in solution sufficiently decreased and thus, no further prominent removal was observed.

*3.4.1.2.3. Effect of Treatment Time and Initial Ion Concentration*

Figure 3.4.5 (b-d) showed the effect of treatment time and initial As(III) concentration on removal efficiency of the SICC material at three different temperatures viz. 303, 308 and 313 K, respectively. For each temperature of study, the sorption rate increased initially with the treatment time, but beyond 60 min of

treatment, there was hardly any further increase in removal rate. This could be due to achievement of equilibrium between the As(III) in solution and at the surface of the adsorbent. Again, the sorption capacity of the material was found to increase with the increase in initial ion concentration. This might be due to the increase in concentration gradient between the As(III) ions present in the solution and that at the surface of the adsorbent and thus, equilibrium was shifted more towards adsorbed side.

*3.4.1.2.4 Effect of Temperature*

The sorption capacity of the material at equilibrium increased on increasing the temperature [Figure 3.4.5 (b-d)]. Increase in sorption amount with increase in temperature indicated endothermic nature of the sorption. Again, increase in temperature can enhance sorption rate only when its nature is chemical. If it is only due to weak forces, then increase in temperature will increase randomness at interface resulting into increase in rate of desorption. The increasing sorption at high temperature might be due to the enlargement of pore size, which increased the active surface for sorption, enhanced mobility of the metal ions from the bulk of the solution towards adsorbent surface and thereby enhanced penetration within the material structure by overcoming the rate of intraparticle diffusion [29].

***3.4.1.3 Thermodynamics and Activation Energy Calculations***

The thermodynamic data obtained for the sorption of trivalent arsenic on SICC are presented in table 3.4.4, for Gibbs free energy, enthalpy and entropy along with activation energy data.

**Table 3.4.4** Activation energy and thermodynamic parameters for sorption of As(III)

| T (K) | $E_a$ ($kJmol^{-1}$) | $K_c$ | $R^2$ | $\Delta G°$ ($kJmol^{-1}$) | $\Delta H°$ ($kJmol^{-1}$) | $\Delta S°$ ($JK^{-1}mol^{-1}$) |
|---|---|---|---|---|---|---|
| 303 | | 87.23 | | -11.25 | | |
| 308 | 59.16 | 125.2 | 0.964 | -12.38 | 42.48 | 177.6 |
| 313 | | 149.4 | | -13.40 | | |

From the table, it was noted that the changes in Gibbs free energy values were negative for all those temperatures under interest indicating the feasibility of the

process. The increase in magnitude for the calculated values with temperature indicated that adsorption became more favorable as temperatures increased which implied an endothermic process. Similar results were reported by Cantu et al. [30] in the sorption of Cr(III) and Cr(VI) over $Mn_3O_4$ nanomaterial.

The endothermic nature of sorption was further supported by the positive apparent $\Delta H°$ value (+42.48). Moreover, high value of $\Delta H°$ (>40 kJ/mol) might be an indication of chemisorption. Again, an increase in entropy at equilibrium was observed during the sorption process (+177.6). This might be due to the increase in randomness at the solid-liquid interface during the adsorption process [31]. Also, very high $\Delta S$ for sorption of As(III) over SICC indicated that certain materials were loosed during sorption. This kind of behavior might be due to the occurrence of ion-exchange during sorption. In present study, exchange of ions might occurred because of the presence of incorporated clay in the system.

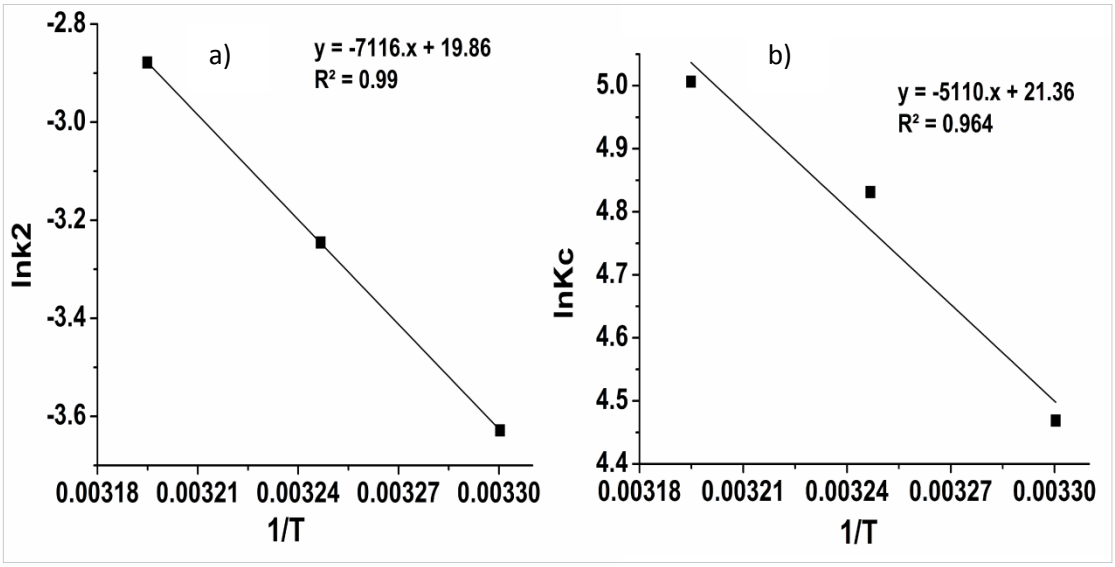


**Figure 3.4.6** a) Arrhenius plot and b) Thermodynamic plot of sorption of As(III) on SICC

The activation energy of sorption of As(III) over SICC was found to be 59.16 kJ/mol. Chemisorption is very specific in nature and activation energy for chemisorption is of similar magnitude as that of heat of chemical reaction [32]. The high activation energy in sorption thus indicated that the sorption was predominantly chemical in nature. Activation energy of similar magnitude during the binding of Cd(III) to Zero valent iron was reported by Boparai et al. [33].

### *3.4.1.4 Kinetics of Adsorption*

The kinetic study was also performed for the three temperatures. Figure 3.4.7 (b-d) represent the variation of $q_t$ (mg/g) of arsenic over time for five different initial arsenic ion concentrations in the range of 0.5-4 mg/L. For each temperature, $q_t$ values were found to increase with the increase in the initial arsenic concentrations. This might be due to high concentration gradient of arsenic at the interface of sorbent and solution. The plots of log ($q_e$-$q_t$) vs t and $t/q_t$ vs t as per equation (2) and (3) gave straight lines from which the different kinetic parameters for pseudo first order and pseudo second order were evaluated and given in Table 3.4.5.

**Table 3.4.5** Parameters of different kinetic models on sorption of As(III)

| Adsorption condition | $q_e$, exp (mg/g) | Pseudo-first-order model | | | Pseudo-second-order model | | | |
|---|---|---|---|---|---|---|---|---|
| | | $k_1$ ($min^{-1}$) | $q_e$, cal (mg/g) | $R^2$ | $k_2$ g/mg/min | $q_e$, cal (mg/g) | $R^2$ | H |
| **Conc[a]/mgL$^{-1}$** | | | | | | | | |
| 0.5 | 0.254 | 0.025 | 0.074 | 0.758 | 0.465 | 0.26 | 0.997 | 0.032 |
| 1.0 | 0.488 | 0.034 | 0.154 | 0.699 | 0.110 | 0.56 | 0.984 | 0.034 |
| 2.0 | 0.968 | 0.029 | 0.353 | 0.763 | 0.026 | 1.11 | 0.902 | 0.039 |
| 3.0 | 1.450 | 0.031 | 0.820 | 0.893 | 0.015 | 1.69 | 0.943 | 0.052 |
| 4.0 | 1.934 | 0.034 | 1.061 | 0.880 | 0.008 | 2.26 | 0.942 | 0.060 |
| **Temp[b]/K** | | | | | | | | |
| 303 | 0.968 | 0.029 | 0.353 | 0.763 | 0.026 | 1.11 | 0.902 | 0.039 |
| 308 | 0.976 | 0.031 | 0.382 | 0.783 | 0.039 | 1.16 | 0.954 | 0.053 |
| 313 | 0.980 | 0.038 | 0.458 | 0.862 | 0.056 | 1.22 | 0.995 | 0.069 |

[a] Conditions: temp. 30 $^oC$, material dose 2 g/L
[b] Conditions: concentration 2g/L, material dose 2 g/L

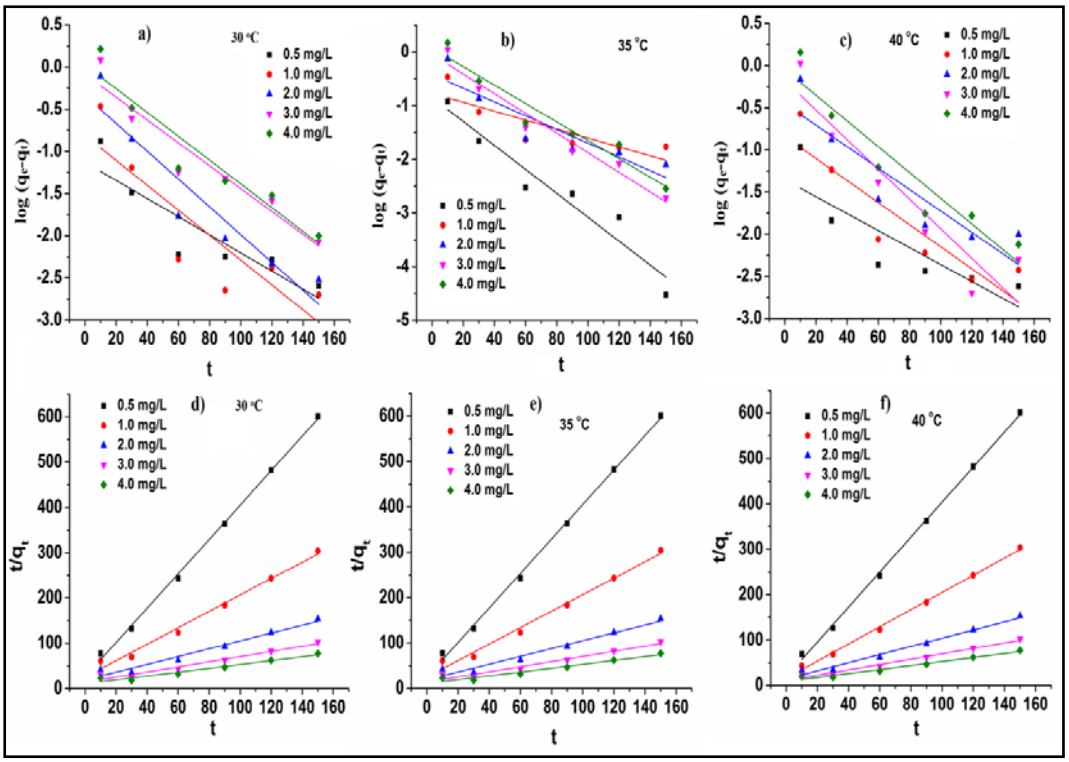


**Figure 3.4.7** First order (a-c) and second order (d-f) kinetic models for sorption of arsenic at 30, 35 and 35 °C

The correlation coefficients ($R^2$) were computed for the all models and the values are shown in Table 3.4.5. The curve for pseudo second order kinetics exhibited higher correlation co-efficient compared to the other models. Also, the $q_e$ values calculated from the second order kinetic model was more closure to the experimental values. Thus, the sorption pattern followed a second order kinetic model more preferably. Also, the linear increase in second order rate constant with increase in temperature indicated endothermic nature of sorption of As(III) over SICC.

*3.2.7. Adsorption isotherm*

Figure 3.4.8 shows the growth of adsorbed amount of arsenic (mg/g) at equilibrium over the surface of SICC against increase in equilibrium concentrations. To establish the influence of arsenic concentration on the adsorption process, the equilibrium data was analyzed by linear forms of Langmuir and Freundlich models using equations (4) and (5), respectively and are shown in table 3.4.6.

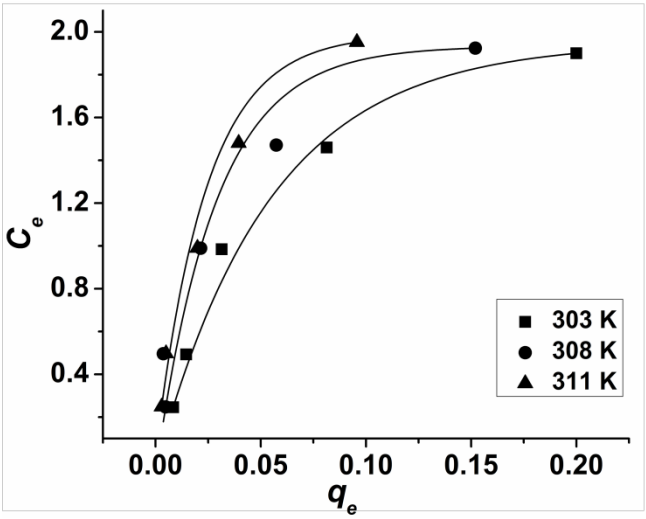


**Figure 3.4.8** Ce vs qe plot of sorption of As(III) on SICC at three different temperatures

$R_L$ value (0.081 at 303 K) showed the suitability of Langmuir model for the sorption. Also, $q_e$ vs $C_e$ showed linearity of the graph (Figure 3.4.8). Freundlich parameters, $R^2$ and n values, as shown in table 3.4.6, also indicated good fitting of sorption data with the model.

**Table 3.4.6** Isotherm constants and correlation coefficients for sorption of As(III)

| T/K | Langmuir parameters | | | Freundlich parameters | | |
|---|---|---|---|---|---|---|
| | $q_m$ (mg/g) | $R_L$ | $R^2$ | $K_F$ (mg/g) | N | $R^2$ |
| 303 | 2.04 | 0.081 | 0.973 | 6.37 | 1.59 | 0.896 |
| 308 | 2.29 | 0.133 | 0.977 | 5.54 | 1.92 | 0.925 |
| 313 | 2.43 | 0.095 | 0.991 | 8.52 | 1.76 | 0.961 |

$R^2$ values for both Langmuir and Freundlich models showed good co-relations of data and sorption could be reasonably explained by the models under consideration. $R^2$ values for Langmuir model was higher than those of Freundlich model. Thus, the preferential order for sorption, among these models is as follows- Langmuir >

Freundlich. This confirmed that the sorption was predominantly due to chemical interaction.

## References

[1] Gupta, K. K., Singh, N. L., Pandey, A., Shukla, S. K., Upadayay, S. N., Mishra, V. and Mishra, P. K. Effect of anatase/rutile $TiO_2$ phase composition on arsenic adsorption. *Journal of Dispersion Science and Technology*, 34:1043-1052, 2013.

[2] Deka, B. K. and Maji, T. K. Effect of $TiO_2$ and nanoclay on the properties of wood polymer nanocomposite. Composites Part A: *Applied Science and Manufacturing*, 42:2117-2125, 2011.

[3] Xu, Z., Li, Q., Gao, S. and Shang, J. K. As (III) removal by hydrous titanium dioxide prepared from one-step hydrolysis of aqueous $TiCl_4$ solution. *Water Research*, 44:5713-5721, 2010.

[4] Kung, K. H. S. and Hayes, K. F. Fourier transform infrared spectroscopic study of the adsorption of cetyltrimethylammonium bromide and cetylpyridinium chloride on silica. *Langmuir*, 9:263-267, 1993.

[5] Kousalya, G. N., Gandhi, M. R. and Meenakshi, S. Sorption of chromium (VI) using modified forms of chitosan beads. *International Journal of Biological Macromolecules*, 47:308-315, 2010.

[6] Sham, E. L., Aranda, M. A., Farfan-Torres, E. M., Gottifredi, J. C., Martinez-Lara, M. and Bruque, S. Zirconium titanate from sol–gel synthesis: thermal decomposition and quantitative phase analysis. *Journal of Solid State Chemistry*, 139:225-232, 1998.

[7] Jiang, Z. Xie, J. Jiang, D. Wei X. and Chen, M. Modifiers-assisted formation of nickel nanoparticles and their catalytic application top-nitrophenol reduction. *CrystEngComm*, 15:560-569, 2013.

[8] Juang, R. S. and Shiau, R. C. Metal removal from aqueous solutions using chitosan-enhanced membrane filtration. *Journal of Membrane Science*, 165:159-167, 2000.

[9] Wang, H., Liu, P., Cheng, X., Shui, A. and Zeng, L. Effect of surfactants on synthesis of TiO 2 nano-particles by homogeneous precipitation method. *Powder Technology*, 188:52-54, 2008.

[10] Chakravarty, S., Dureja, V., Bhattacharyya, G., Maity, S. and Bhattacharjee, S. Removal of arsenic from groundwater using low cost ferruginous manganese ore. *Water Research*, 36:625-632, 2002.

[11] Dutta, P. K., Ray, A. K., Sharma, V. K. and Millero, F. J. Adsorption of arsenate and arsenite on titanium dioxide suspensions. *Journal of Colloid and Interface Science*, 278:270-275, 2004.

[12] Xu, Z., Li, Q., Gao, S. and Shang, J. K. As (III) removal by hydrous titanium dioxide prepared from one-step hydrolysis of aqueous $TiCl_4$ solution. W*ater Research*, 44:5713-5721, 2010.

[13] Guan, X., Du, J., Meng, X., Sun, Y., Sun, B. and Hu, Q. Application of titanium dioxide in arsenic removal from water: a review. *Journal of Hazardous Materials*, 215:1-16, 2012.

[14] Catalano, J. G., Luo, Y. and Otemuyiwa, B. Effect of aqueous Fe (II) on arsenate sorption on goethite and hematite. *Environmental Science & Technology*, 45:8826-8833, 2011.

[15] Vitela-Rodriguez, A. V. and Rangel-Mendez, J. R. Arsenic removal by modified activated carbons with iron hydro (oxide) nanoparticles. *Journal of Environmental Management*, 114:225-231, 2013.

[16] Cumbal, L. and SenGupta, A. K. Arsenic removal using polymer-supported hydrated iron (III) oxide nanoparticles: role of Donnan membrane effect. *Environmental Science & Technology*, 39:6508-6515, 2005.

[17] Tresintsi, S., Simeonidis, K., Vourlias, G., Stavropoulos, G. and Mitrakas, M. Kilogram-scale synthesis of iron oxy-hydroxides with improved arsenic removal capacity: Study of Fe (II) oxidation–precipitation parameters. Water research, 46:5255-5267, 2012.

[17] Srinivasan, R. Advances in application of natural clay and its composites in removal of biological, organic, and inorganic contaminants from drinking water. *Advances in Materials Science and Engineering*, 2011, 2011.

[18] Hasan, S., Ghosh, A., Race, K., Schreiber Jr, R. and Prelas, M. Dispersion of FeOOH on Chitosan Matrix for Simultaneous Removal of As (III) and As (V) from Drinking Water. *Separation Science and Technology*, 49:2863-2877, 2014.

[19] Hedin, J., Östlund, Å. and Nydén, M. UV induced cross-linking of starch modified with glycidyl methacrylate. *Carbohydrate Polymers*, 79:606-613, 2010.

[20] Saikia, C., Das, M. K., Ramteke, A. and Maji, T. K. Evaluation of folic acid tagged aminated starch/ZnO coated iron oxide nanoparticles as targeted curcumin delivery system. *Carbohydrate Polymers*, 157:391-399, 2017.

[21] Hairaldin, S. Z., Wan Yunus, W. M. Z. and Ibrahim, N. A. Effect addition of octadecylamine modified clay (ODA-MMT) to polylactide/polycaprolactone (PLA/PCL) blend. *In Advanced Materials Research*, 364:317-321, 2012.

[22] Wang, X., Guo, Y., Yang, L., Han, M., Zhao, J. and Cheng, X. Nanomaterials as sorbents to remove heavy metal ions in wastewater treatment. *Journal of Environmental and Analytical Toxicolo*, 2:1000154, 2012.

[23] Xie, G., Shang, X., Liu, R., Hu, J. and Liao, S. Synthesis and characterization of a novel amino modified starch and its adsorption properties for Cd (II) ions from aqueous solution. *Carbohydrate Polymers*, 84:430-438, 2011.

[24] Yan, X., Li, M., Long, J., Zhang, X., Wei, H., He, Q. and Guo, Z. Highly Monodisperse Sub-microspherical Poly (glycidyl methacrylate) Nanocomposites with Highly Stabilized Gold Nanoparticles. *Macromolecular Chemistry and Physics*, 215:1098-1106, 2014.

[25] Zhu, W., Nan, Y., Huang, T. and Wu, F. The mechanism, thermodynamic and kinetic characteristics of the microbial reduction of goethite mediated by anthraquinone-2-sulfonate. *Geomicrobiology Journal*, 30:928-940, 2013.

[26] Pamplona, T. F., Amoni, B. D. C., Alencar, A. E. V. D., Lima, A. P. D., Ricardo, N. M., Soares, J. B. and Soares, S. D. A. Asphalt binders modified by SBS and SBS/nanoclays: effect on rheological properties. *Journal of the Brazilian Chemical Society*, 23:639-647, 2012.

[27] Das, G., Kalita, R. D., Gogoi, P., Buragohain, A. K. and Karak, N. Antibacterial activities of copper nanoparticle-decorated organically modified montmorillonite/epoxy nanocomposites. *Applied Clay Science*, 90:18-26, 2014.

[28] Aksu, Z. andd Kabasakal, E. Batch adsorption of 2, 4-dichlorophenoxy-acetic acid (2, 4-D) from aqueous solution by granular activated carbon. *Separation and Purification Technology*, 35:223-240, 2004.

[29] Cantu, Y., Remes, A., Reyna, A., Martinez, D., Villarreal, J., Ramos, H. and Parsons, J. G. Thermodynamics, kinetics, and activation energy studies of the orption of chromium (III) and chromium (VI) to a $Mn_3O_4$ nanomaterial. *Chemical Engineering Journal*, 254:374-383, 2014.

[30] Wang, L., Zhang, J., Zhao, R., Li, C., Li, Y. and Zhang, C. Adsorption of basic dyes on activated carbon prepared from Polygonum orientale Linn: equilibrium, kinetic and thermodynamic studies. *Desalination*, 254:68-74, 2010.

[31] Kumar, U. Thermodynamics of the adsorption of Cd (II) from aqueous solution on NCRH cylinder. *International Journal of Environmental Science and Development*, 2:334, 2011.

[32] Boparai, H. K., Joseph, M. and O'Carroll, D. M. Kinetics and thermodynamics of cadmium ion removal by adsorption onto nano zerovalent iron particles. *Journal of Hazardous Materials*, 186:458-465, 2011.

**Section C: Plant Biomass based materials in arsenic remediation**

Phytoremediation of contaminated water by different aquatic plants is a very useful tool for wastewater treatment. It has much significance in the developing countries, as these plants are found abundantly in nature and can provide a simple, effective and yet cheap method for removing heavy metals and other contaminants from water. Water hyacinth (*E. crassipes*) is an aquatic weed having the capability of assimilating large quantities of trace elements and heavy metals [1, 2]. Two materials derived from dried biomass of water hyacinth root powder are demonstrated here for successful utilization in arsenic uptake as follows-

## 3.5 Bioremediation of Arsenic from Water with Citric Acid Crosslinked Water Hyacinth (*E. crassipes*) Root Powder

Water hyacinth (*E. crassipes*), in its living form or dried biomass of its different parts have been established as good adsorbent for water treatment. It is made up of mainly cellulosic and lignocellulosic components. Dried biomass of different parts of this aquatic weed in their unmodified/modified form has been explored as sorbent for different toxic metal ions including arsenic [3, 4, 5].

Non-living, dried roots of *E. crassipes* efficiently remove different arsenic species from contaminated water [6]. But the major concern of using water hyacinth root powder is turbidity and flavor that persist after treatment. Stabilization with different crosslinking agents like glutaraldehyde, citric acid, etc., may help to overcome this difficulty. Citric acid is non toxic, abundant and very cheap material which can be used in this purpose. Citric acid has been used successfully as crosslinking agent for different bio-polymers as well as synthetic polymers used in diverse area of applications [7, 8]. In this purpose, $TiO_2$ can be used as catalyst for crosslinking reaction with citric acid which has the ability to further enhance the arsenic remediation process [9, 10].

Present study aims to prepare a citric acid crosslinked water hyacinth root powder and to investigate its effect on removal of total inorganic arsenic and the turbidity from contaminated water. Effect of different parameters on efficacy of arsenic removal has been studied and optimized.

### 3.5.1 Results and Discussion

Samples were prepared as coded in Table 3.5.1. The wt (%) of root powder was kept constant while those of citric acid and titanium dioxide were varied. The weight % of various components in preparing the sorbent material along with the respective codes are listed in Table 3.5.1.

**Table 3.5.1** Composition of the sorbent materials

| Sample | Root powder[a] | Citric acid[b] | $TiO_2$ |
|---|---|---|---|
| WHRP | 100 | - | - |
| RP | 100 | 5 | - |
| RP/1CA | 100 | 1 | 0.6 |
| RP/5CA | 100 | 5 | 0.6 |
| RP/10CA | 100 | 10 | 0.6 |

[a] 8 g of root powder was assumed as 100 g

[b] the amount of citric acid with respect to root powder

#### *3.5.1.1 Characterization*

*3.5.1.1.1 FT-IR Analysis*

FT-IR spectra of Water Hyacinth root powder (RP), physical blend (CARB) of citric acid and root, citric acid crosslinked root (RP) and Arsenic adsorbed citric acid crosslinked root (As/RP) are shown in Figure 3.5.1

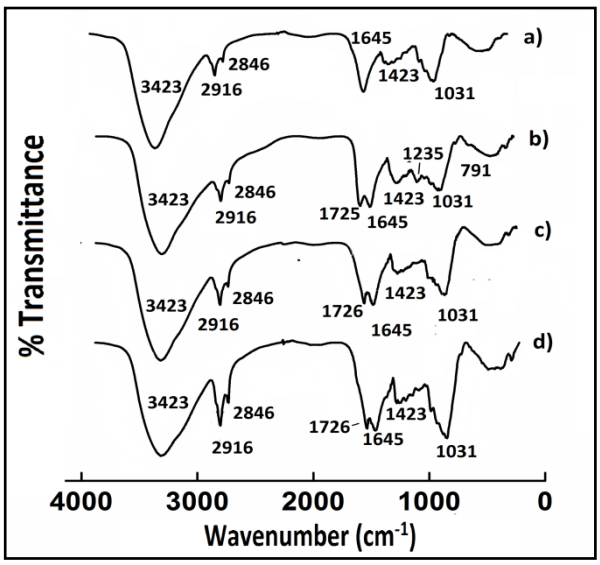


**Figure 3.5.1** FTIR spectra of (a) RP (b) CARB (c) RP (d) As/RP

In all the spectra, the absorption bands at 2916, 2846, 1423 cm-$^{1}$ were assigned to asymmetric, symmetric and scissoring modes of $–CH_2$ stretching in methylene chains, respectively and band near 3423 cm$^{-1}$ is due to OH group [11]. Characteristic bands near 791 cm$^{-1}$, 1031 cm$^{-1}$, were due to oxide bonds of metal. Band at 1423cm$^{-1}$ may be due to phenolic OH group. There are some additional peaks at 1725 cm$^{-1}$, 1645 cm$^{-1}$ and 1235 cm$^{-1}$ in citric acid root blend (curve-b). This might be due to the C=O stretching vibration of carboxylic group [12]. Presence of these bands with weak intensity in the crosslinked sample indicated the formation of successful crosslinking in root powder.

The intensity of the peaks appeared at 1031 cm$^{-1}$ and 1645 cm$^{-1}$ increased in arsenic adsorbed crosslinked root powder (curve-d), suggesting possible binding of arsenic onto the surface of crosslinked root powder.

*3.5.1.1.2 TGA Analysis*

Thermograms of citric acid crosslinked root (RP), citric acid root blend (CARB) and root (WHRP) is shown in Figure 3.5.2. In all the thermograms, the initial weight loss at around 100 °C was due to evaporation of moisture. The major weight loss occurred in the range 230-360 °C. The weight loss was more in the RP (c) than crosslinked CARP (a). The value for the CARB (b) powder was in between WHRP and RP. The percentage of char was more in CARP compared to either CARB or WHRP. This indicated an improvement in the thermal stability due to crosslinking.

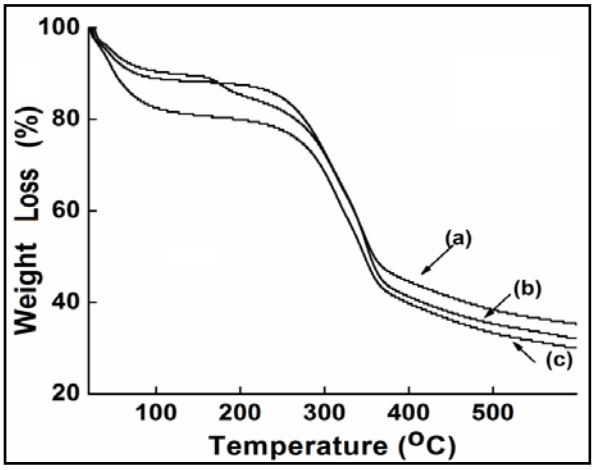


**Figure 3.5.2** Thermal degradation pattern of (a) RP, (b) CARB and (c) WHRP

*3.5.1.1.3 SEM-EDX Study*

SEM image of arsenic adsorbed RP (As/RP) appeared rough (Figure 3.5.3 b) compared to that of image for RP (Figure 3.5.3 a). The roughness might be due to

adhesion of arsenic on to the surface RP. The roughness was found less (c-d) in both the arsenic desorbed samples after one cycle (As/1/RP) and after fourth cycle (As/4/RP). Futher, the EDX spectrum of RP {Figure 3.5.3 (e)} shows the presence of metals like calcium, iron, aluminium, silicon, etc. [5]. The presence of arsenic along with other metals in the EDX spectrum of arsenic adsorbed RP (f) indicated the succesful adsorption of arsenic on to the surface of RP.

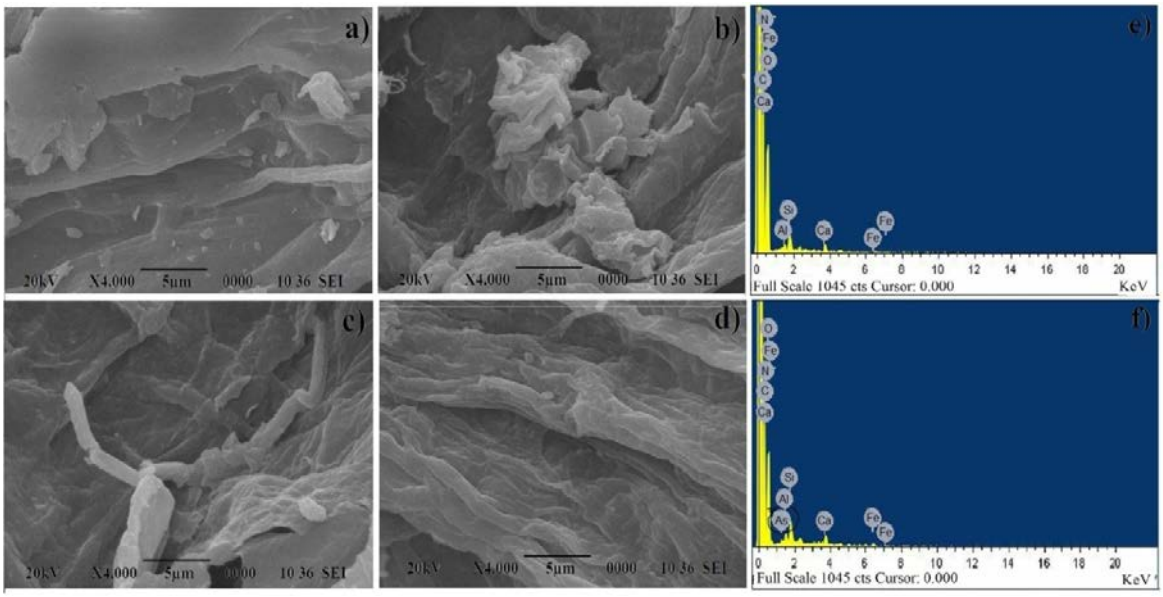


**Figure 3.5.3** SEM images of a) RP, b) As/RP, c) As/1/RP and d) As/4/RP, EDX spectra of e) RP and f) As/RP

### *3.5.1.2 Effect of Citric Acid Crosslinking on Arsenic Removal by RP*

The main purpose of crosslinking was to enhance reusability of the material and to decrease turbidity produced after treatment of arsenic containing water with RP.

#### *3.5.1.2.1 Effect of Crosslinking on Turbidity*

These materials were tested for a targeted arsenic [50:50 As(III):As(V)] solution containing 0.4 mg/L of Arsenic for 5 h. After the treatment, solutions were allowed to settle down and the supernatants were centrifuged and filtered. Each aliquot was divided into two parts; one is kept for arsenic analysis by AAS and other for turbidity analysis with the help of Nephalometer. For most of the earlier cases, initially efficiency was tried to evaluate for As(V) [since As(III) is difficult to remove and most of the time requires pre-oxidation step]. Once it was found sufficiently good, it will be tried to implement for As(III). The turbidity results are shown in the table below-

**Table 3.5.2** Effect of cross linking on turbidity

| Material | Arsenic left (mg/g) | NTU before treatment | NTU after treatment |
|---|---|---|---|
| WHRP | 0.011 | 0.25 | 24.5 |
| RP/1CA | 0.010 | 0.25 | 23.4 |
| RP/5CA | 0.011 | 0.25 | 8.35 |
| RP/10CA | 0.010 | 0.25 | 2.74 |

From the table, it was observed that after treatment of arsenic water with RP, a huge amount of turbidity was left in the aliquot as judged by NTU value. Similar was the case for the material crosslinked with 1 % (w/w) CA. When the amount of CA was increased to 5% (w/w) the turbidity decreased significantly.

Further increase of percentage of CA in the sample from 5 to 10% decreased the turbidity level to 2.74 which was quite low [turbidity of drinking water should not be more than 5 NTU, and should ideally be below 1 NTU, (WHO standard), 1NTU (E.U standard)] [6]. Turbidity of the treated water might arise due to the presence of some soluble parts like soluble proteins, fine suspended particles, etc. which didn't get separated by simple method. After citric acid crosslinking some of these materials may get stabilized, via binding through different functional moiety present at their backbone.

*3.5.1.2.2 Effect of Material dose on Removal Efficiency*

From Figure 3.5.4 (A), it was observed that for an initial arsenic concentration of 0.4 mg/L, the removal efficiency increased gradually with the increase in material dose. A dose of 5 g/L of solution was found to be sufficient for bringing down the solution concentration below 10 µg/L, which is the recommended limit of arsenic in drinking water [14]. Beyond that dose, the removal efficiency was not so much significant. Therefore, a material dose of 5 g/L was taken for further study. With the increase in material dose, the number of active functional/or binding/and surface sites increases and hence the sorption increases. Influence of further increase in material dose was not so significant. It might be due to the presence of very small amount of arsenic ions in solution which instantly attain equilibrium with the adsorbed arsenic ions present on the surface of the material.

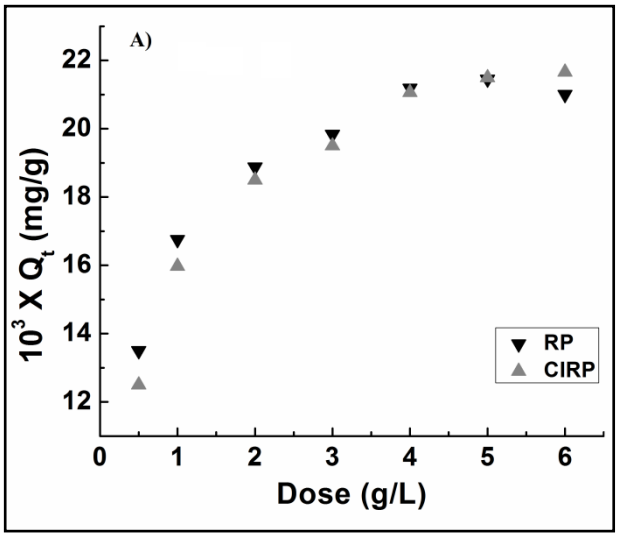


**Figure 3.5.4** Effect of material dose (A), treatment time (B) and initial ion concentration (C) on Removal efficiency of Arsenic

Comparative study of removal efficiency showed that after cross liking with citric acid, removal efficiency of RP didn't show any significant change (Table 3.5.1). Also, previous study showed the usefulness of citric acid crosslinking in turbidity removal. Thus, citric acid crosslinked RP can be preferably used in arsenic removal as compared to the unmodified RP. Citric acid might influence the sorption rate of the material by oxidizing As(III) in solution to As(V), the later being easier to remove [7]. But in the present case, citric acid was used only as a crosslinking agent and the crosslinked product was washed several times with de-ionized water. Therefore, it was unlikely that free citric acid would remain in the crosslinked material. Hence, the precipitation of As(V), if occurs, in presence of iron would be negligible. Thus, on the basis of observation in terms of turbidity as well as arsenic removal efficiency, sample RP/10CA was selected for subsequent experiments.

*3.5.1.2.3 Effect of Treatment Time on Removal Efficiency*

With the increase in agitation time, the equilibrium adsorption capacity of the material increased upto a certain time (210 min), beyond that it remained almost constant. Increase in agitation time allowed more functional sites to bind with arsenic ions. But sorption being a reversible process, after certain time equilibrium was established between adsorbed arsenic on material and the arsenic present in the solution.

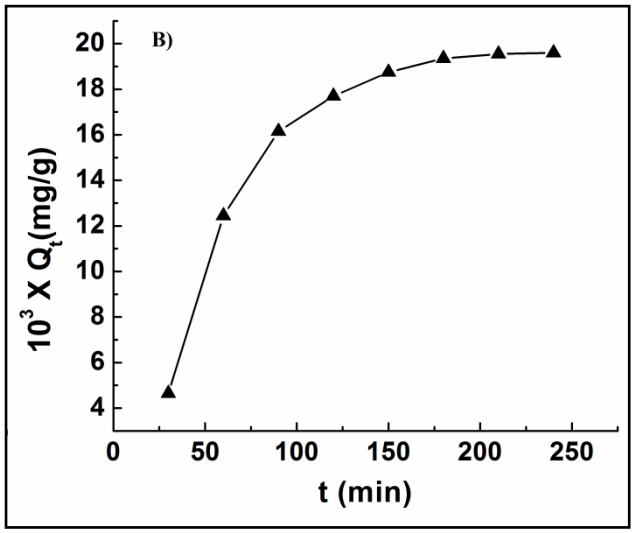


**Figure 3.5.5** Effect of treatment time on removal of As(V)

*3.5.1.2.4 Effect of Initial Ion Concentration*

The effect of initial ion concentration on adsorption capacity/removal rate of arsenic was studied in the concentration range of 0.2-0.7 mg/L for a material dose of 5 g/L for 210 min. Figure 3.5.6 shows the variation of adsorption capacity/removal rate of arsenic with change in initial arsenic concentration. It was observed that the equilibrium sorption capacity (mg/g) was increased with the increase in initial arsenic concentrations while percent removal decreased. The increase in sorption capacity was due to increase in concentration gradient of arsenic at interface of adsorbent and arsenic solution. Again, due to increase in arsenic concentration, equilibrium between arsenic ion present in solution and the adsorbent surface was delayed. As a consequence, removal rate was decreased. Hence, increase in treatment time might increase the removal percent furthermore.

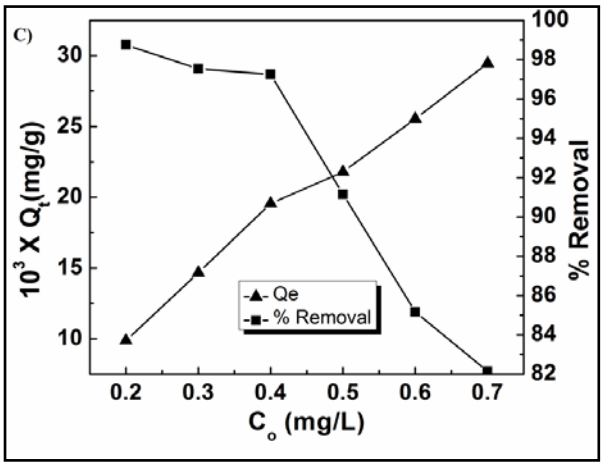


**Figure 3.5.6** Effect of initial ion concentration on removal rate and removal capacity

*3.5.1.2.5 Effect of pH on Removal Efficiency*

Arsenate ions exist in different oxidation states viz. $H_3AsO_4$, $H_2AsO_4^-$, $HAsO_4^{2-}$ and $AsO_4^{3-}$ at different pH conditions of 2.0, 2.0-7.0, 7.0-12.0, and ›12.0, respectively. On the other hand As(III) mostly exist as uncharged species $H_3AsO_3$ in acidic and slightly alkaline medium, $H_2AsO_3^-$ $HAsO_3^{2-}$ and $AsO_3^{3-}$ in the pH ranges ~8.5-12, 12-13.7 and beyond that respectively (as per pH-Eh diagram). The effect of pH on removal rate of arsenic from water was investigated for different initial pH in the range from 1-12 (Figure 3.5.7). The sorption capacity was found to decrease with the increase in pH. The point of zero charge (pzc) for RP/10CA (~6.72) was determined and found to be approximately 6.72. Thus, below pH=6.72 the material surface was positively charged. The increase in removal capacity at low pH indicated electrostatic type of interactions between the sorbent and arsenic in water. On the other hand, at pH>6.72 the surface of the material became negatively charged resulting into a decreased removal capacity due to electrostatic repulsion.

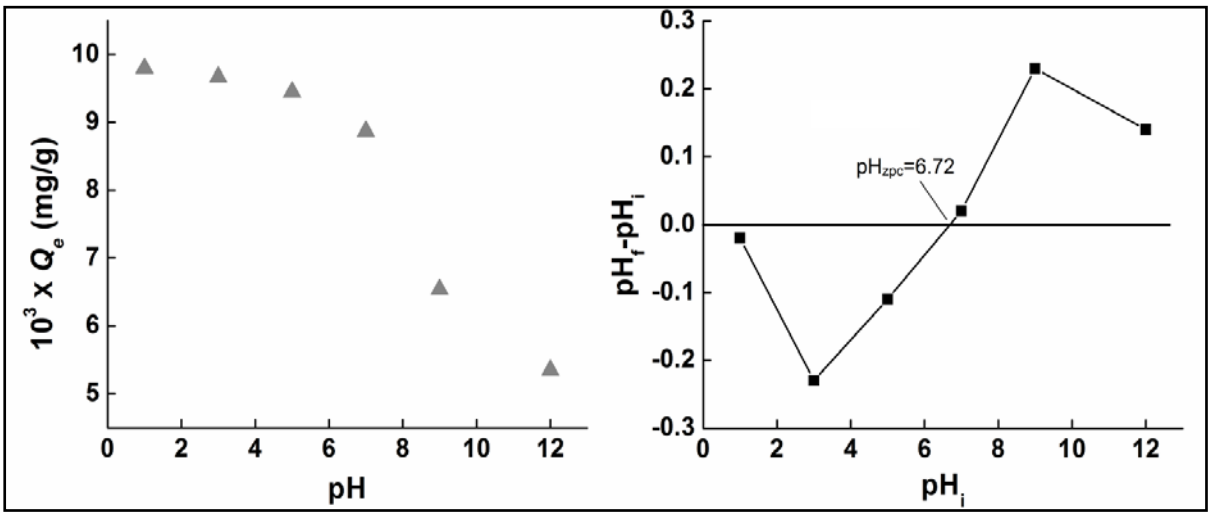


**Figure 3.5.7** Effect of pH on removal efficiency and ΔpH vs pH for zero point charge.

### *3.5.1.3 Kinetics of Adsorption*

Figure 3.5.8 (A) represents the variation of $Q_t$ (mg/g) of arsenic over time for three different initial arsenic ion concentrations viz. 0.3, 0.5 and 0.7 mg/L. The $Q_t$ values were found to increase with increase in initial arsenic concentrations. This might be due to high concentration gradient of arsenic at the interface of sorbent and solution. The plots of log ($Q_e$-$Q_t$) vs t and t/$Q_t$ vs t as per equation (2) and (3) gave straight lines

from which the different kinetic parameters for pseudo first order and pseudo second order were evaluated and given in Table 3.5.2.

In Figure 3.5.8 (B) multilinear curve for each concentration was observed which indicated that intraparticle diffusion played an important role in the sorption process although it was only the rate controlling step. The first portion of the curve was due to the boundary layer diffusion while the second portion was due to gradual adsorption process where intraparticle diffusion was the rate limiting step. First and second portion for each curve, as mentioned are represented by the boundary values between 9-10 along x-axis. Results given in table 3.5.2 showed that rate constant for the second step ($k_{i2}$) was smaller than that in first step ($k_{i1}$) suggesting that the intraparticle diffusion was the rate determining step [11].

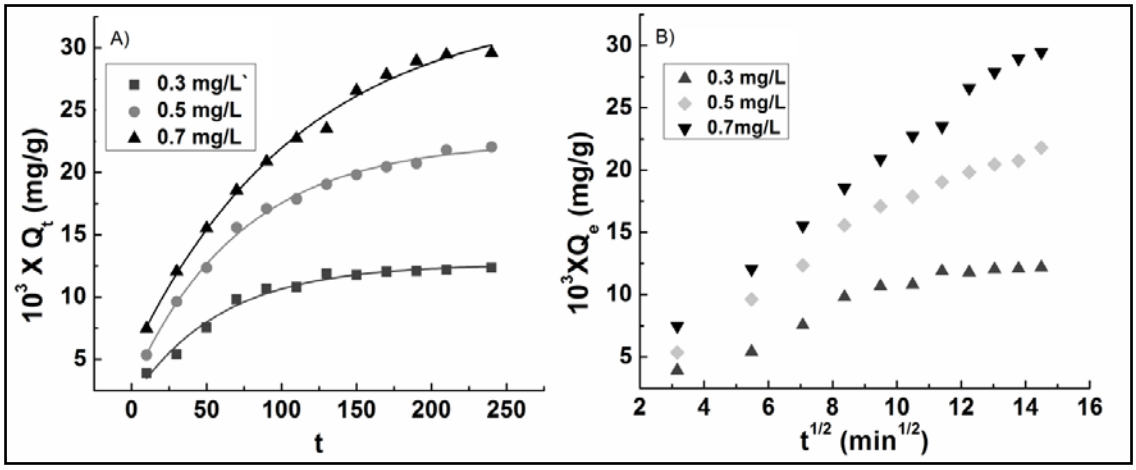


**Figure 3.5.8** Kinetics of sorption of arsenic on RP/10CA

The correlation coefficients ($R^2$) were computed for all models and values are shown in Table 3.5.2. The curve for pseudo second order kinetics exhibited higher correlation co-efficient (>0.98) compared to other models indicating the preference for a monolayer chemisorptions pattern.

Srivastava et al. [5] have performed similar experiments with root powder only and reported very good adsorption capacity of dried powder for As(III) remediation. The study mainly focused on different kinetic parameters evaluated on the basis of numbers of kinetic models. It was not clearly mentioned about the optimum dose, time or other parameters influencing the sorption in the study. Moreover, in present study, material was modified with cross linker, which was actually improving the stability and hence decreasing the turbidity of aqueous solution. Those factors were missing in their study.

**Table 3.5.3** Parameters for different kinetic models for sorption of Arsenic on RP/10CA

| $C_o$ (mg/L) | $10^3$x $Qe$ (exp) | First order kinetic model | | | Second order kinetic model | | | | Intra particle-diffusion model | | | | | |
|---|---|---|---|---|---|---|---|---|---|---|---|---|---|---|
| | | $K_1$ x $10^{-4}$ ($min^{-1}$) | $10^3$ x $Qe$ (mg/g) | $R^2$ | $K_2$ g$mg^{-1}min^{-1}$ | $10^3$x $Q_e$ (Cal) (mg/g) | $h$x$10^{-4}$ | $R^2$ | $10^{-4}$ x $Ki_1$ $gmg^{-1}min^{-1/2}$ | Cx$10^{-4}$ | $R^2$ | $Ki_2$ x $10^{-4}$ $gmg^{-1}min^{-1/2}$ | C x$10^{-3}$ | $R^2$ |
| 0.3 | 14.6 | 4.54 | 142 | 0.973 | 2.01 | 14.3 | 4.11 | 0.989 | 4.54 | -0.76 | 0.927 | 0.507 | 7.8 | 0.893 |
| 0.5 | 21.8 | 21.8 | 194 | 0.914 | 0.76 | 26.5 | 5.32 | 0.995 | 7.57 | -8.75 | 0.992 | 3.17 | 8.43 | 0.985 |
| 0.7 | 29.5 | 29.4 | 264 | 0.863 | 0.42 | 37.4 | 5.93 | 0.986 | 7.96 | 6.10 | 0.997 | 2.17 | 4.37 | 0.979 |

### *3.5.1.4 Adsorption Isotherm*

Figure 3.5.9 shows the growth of adsorbed amount of arsenic (mg/g) at equilibrium over the surface CA/10RP against increase in equilibrium concentrations. To establish the influence of arsenic concentration on the adsorption process, the equilibrium data was analyzed by linear forms of Langmuir and Freundlcih models and are shown in table 3.5.4

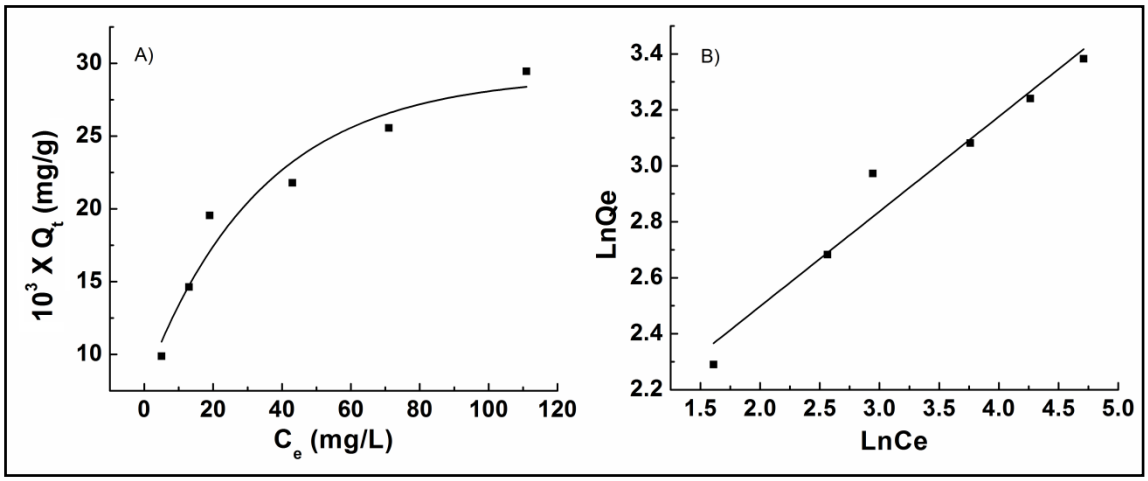


**Figure 3.5.9** Time evolution of $Q_e$ vs t and B) Freundlich isotherm model for sorption of arsenic on RP/10CI

**Table 3.5.4** Various isotherm models and related parameters

| Model | Parameters | |
|---|---|---|
| Langmuir | $Q_0$ (mg/g) | 0.028 |
| | B | 103.7 |
| | $R_L$ | 0.014 |
| | $R^2$ | 0.966 |
| Freundlich | $k_f$ (mg/g) | 6.17 |
| | N | 2.94 |
| | $R^2$ | 0.930 |

$R_L$ value (0.014) showed the suitability of Langmuir model for the sorption. Also $Q_e$ vs $C_e$ showed linearity of the graph (Figure 3.5.9). Freundlich parameters $R^2$ and n values as shown in table 3.5.4 also indicated good fitting of sorption data with the model.

$R^2$ values for both Langmuir and Freundlich models showed good co-relations of data and sorption could be reasonably explained by the models under consideration. $R^2$ values for Langmuir model was higher than that of Freundlich model. Thus, the preferential order for sorption, among these models is as follows- Langmuir > Freundlich.

### *3.5.1.5 Reusability Test*

Desorption of arsenic was carried out with 0.05 M HCl solutions followed by washing with Milli Q water until it became neutral. The weight loss (%) after each cyclic run for both RP and RP/10CA is shown in Figure 3.5.10 (A). It was observed that the weight loss (%) of material was significantly low ($p < 0.05$, after fourth run) for RP/10CA as compared to RP. Figure 3.5.10 (B) shows the percent removal rate of RP/10CA and RP after each cyclic run. The removal rate was same for both the samples for the first run but the rate was found to decrease significantly for RP compared to RP/10CA in the subsequent cyclic runs ($p < 0.05$, after fourth run).

This might be due to the more loss in RP compared to RP/10CA. During the acid treatment the RP may lose some of its structural moiety which took part in arsenic binding process. But in case of RP/10CA the loss of structural moiety might be due to the network structure provided by crosslinking.

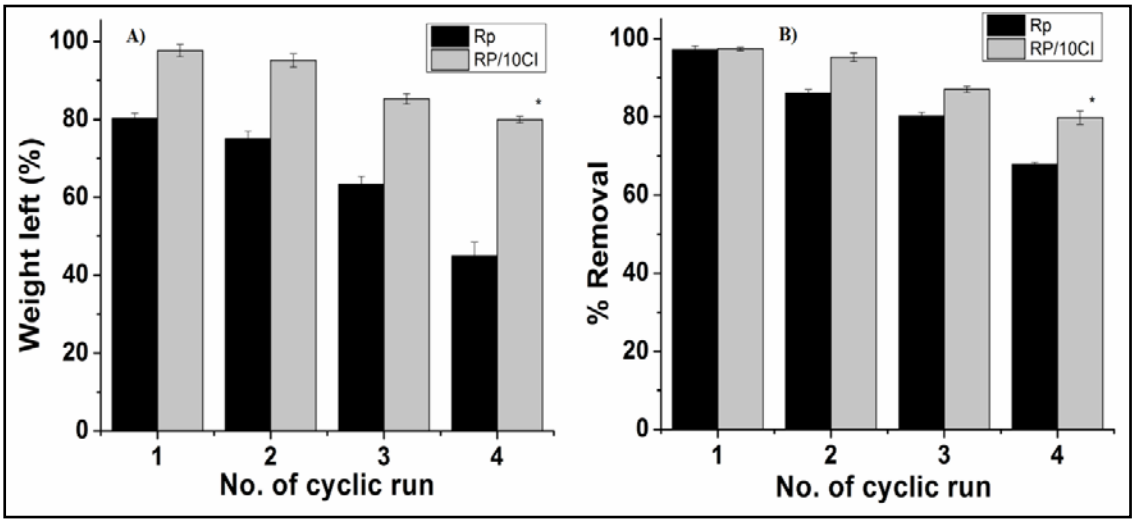


**Figure 3.5.10** Reusability test for sorption of arsenic on RP and RP/10CI

## 3.6 Synergistic effect of *E. crassipes* Biomass/Chitosan for As(III) Remediation: A Mechanistic Approach

This part describes the synergistic effect and mechanistic steps of sorption of As(III) over a new composite system prepared by amalgamating dried *E. crassipes* root powder with chitosan.

Chitosan biopolymer has been identified as an efficient scavenger for different arsenic species from water [16]. Despite the excellent properties of chitosan, such as bio-compatibility, bio-degradability, high sorption efficiency and ease of modifications as compared to synthetic polymers it is costlier and no longer remained cost effective for water treatment purpose. But its excellent sorption properties encourage researchers to employ it in this area, adopting certain measurements to reduce cost [17].

Different biomasses which mainly comprise of cellulosic material having more or less similar structure to that of chitosan may be usable in combination with chitosan to make it cost effective without affecting the sorption efficiency. Jiufang et al. [18] have prepared a cellulose-chitosan gel complex via intermolecular inclusion interaction which has self healing ability. The turbidity and leaching due to biomass can be minimized by coating the powder with polymeric material. This may not only remove the turbidity but also prevent the agglomeration and thus, may enhance its efficacy.

Keeping these in view, the present study has been undertaken. This study aims to prepare a composite of root powder with chitosan biopolymer stabilized by glutaraldehyde crosslinker and utilized the advantages of both the materials to develop a combined system having superior property and cheap in nature. A model describing different interactions during the preparation of chitosan-WHRP-glutaraldehyde composite and its binding with arsenic is presented with the help of density functional theory (DFT) and verified experimentally with FTIR.

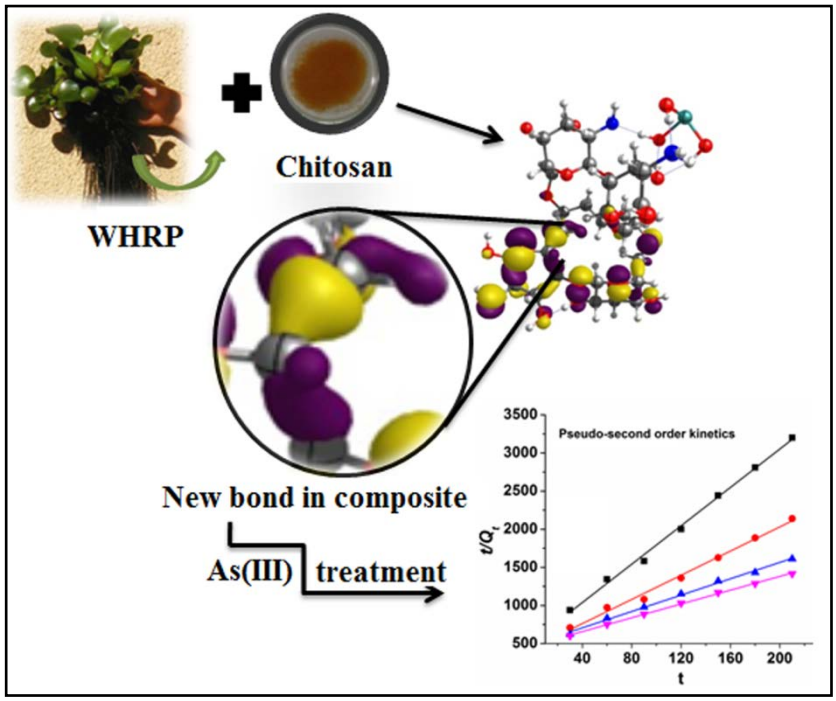


**Scheme 3.6.1** Preparation of CIRP and interactions among the components and its final use

### 3.6.1 Results and Discussion

#### *3.6.1.1 Characterisation*

*3.6.1.1.1 FT- IR Analysis*

Figure 3.6.1 (A) represents the FT-IR spectra of CT (a), WHRP (b), CTRB (c), CTRP (d) and CTRP-As (e), respectively. The characteristics absorption bands shown by all the spectra near 3435 $cm^{-1}$ and 2929 $cm^{-1}$ were due to O-H, N-H stretching, and due to $CH_2$ stretching vibrations [11, 19]. The intense band near 1642 $cm^{-1}$ might be assigned to deformation mode of $NH_2$ in CT or due to the bending vibration resulting from H-O-H intermolecular linkages. Band at 1411 $cm^{-1}$ was due to the scissoring modes of $–CH_2$ stretching in methylene chains and at 1031 $cm^{-1}$ was characteristic of C-O stretching from carbohydrate. These data are in accordance with those obtained from literature [12, 20]. Similarly, in the physical blend of CT and WHRP (curve-c), increase in intensity near 1642 $cm^{-1}$ might be due to increase in the amount of –OH functionality. Another important band around 1164 $cm^{-1}$ due to C-N stretching was observed in the spectrum of chitosan and all other materials containing CT.

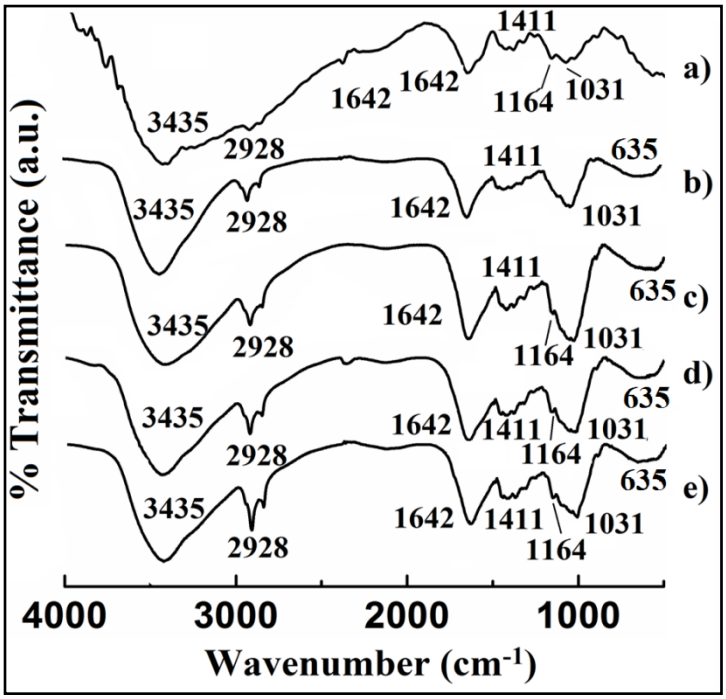


**Figure 3.6.1** FT-IR spectra of a) CT, b)WHRP, c) CTRB, d) CT:RP/1:2 and e) CT:RP/1:2-As

Change in intensity of this peak [Figure 3.6.1(A)] (e)] along with that of 1642 $cm^{-1}$ (may be due to the formation of N-C=O bond during cross linking) confirmed the formation of new chemical bond of glutaraldehyde with different polymeric moieties. No characteristic band appeared in the spectrum for aldehydic group utilized in the crosslinking process.

The intensity of the peaks appeared at 1031 $cm^{-1}$ and around 636 $cm^{-1}$ increased after arsenic sorption on to the material but that of 1642 $cm^{-1}$ decreased during the process (curve-e). Those intensity measurements were carried out with respect to the $–CH_2$ stretching frequency. This suggested the possible binding of arsenic onto the surface of crosslinked root powder. The decrease in intensity near1642 $cm^{-1}$ was due to utilization of $NH_2$ groups in the binding process. In contrary, increase in intensities in the former cases was due to the contribution of newly formed O-As bond during the sorption. This indicated successful sorption of arsenic on the composite material.

**Table 3.6.1** Experimental and theoretical infrared spectral data for the optimized complexes, ν is the vibrational frequency in $cm^{-1}$

| Assignment | | Frequency ($cm^{-1}$) | Assignment | | Frequency ($cm^{-1}$) |
|---|---|---|---|---|---|
| ***Complex 1(d)*** | | | ***Complex 1(e)*** | | |
| ν(C-O) *stretching* | Exp.[a] | 1060-1175 | ν(C-O) *stretching* | Exp. | 1060-1175 |
| | Calc. | 1078.8 | | Calc. | 1062.1 |
| ν(O-H) *bending* | Exp.[b] | 1375-1400 | ν(O-H) *bending* | Exp. | 1375-1400 |
| | Calc. | 1391.5 | | Calc. | 1394.2 |
| ***Complex 1(f)*** | | | ν(N-H) *stretching* | Exp. | 3400-3500 |
| ν(C-O) *stretching* | Exp. | 1060-1175 | | Calc. | 3430.1 |
| | Calc. | 1067.7 | ν(N-H) *bending* | Exp. | 1400-1600 |
| ν(O-H) *bending* | Exp. | 1375-1400 | | Calc. | 1626.3 |
| | Calc. | 1393.8 | ***Complex 1(g)*** | | |
| ν(N-H) *stretching* | Exp.[c] | 3400-3500 | ν(C-O) *stretching* | Exp. | 1060-1175 |
| | Calc. | 3447.7 | | Calc. | 1071.1 |
| ν(N-H) *bending* | Exp.[d] | 1400-1600 | ν(O-H) *bending* | Exp. | 1375-1400 |
| | Calc. | 1632.8 | | Calc. | 1396.8 |
| ν(As-O) *stretching* | Exp.[e] | 530-700 | ν(As-O) *stretching* | Exp. | 530-700 |
| | Calc. | 627.5 | | Calc. | 726.2 |

DFT calculations were carried out in order to further confirmed structure and study electronic properties of the novel As/chitosan-cellulose complex. The DFT optimized geometry of As(III), cross-linked polymeric materials and their binding with the former

are shown in Figure 3.6.2. The vibrational frequencies obtained from the optimized geometries are shown in Table 3.6.1 which was found to be in accordance with the experimental results. The hydrogen bond energies for adsorption of As(III)-hydroxide on the chitosan-cellulose complex was found to be 39.16 kcal.mol$^{-1}$ suggesting the bond to be strong and mostly covalent in nature. Whereas, for the adsorption of $As_4O_6$ on cellulose-cellulose complex, energy of the hydrogen bond was found to be 8.34 kcal.mol$^{-1}$, indicating that the bond formed is moderate in strength and electrostatic in nature. Hard-soft acid base interaction might have played some significant role in determining the bond energies.

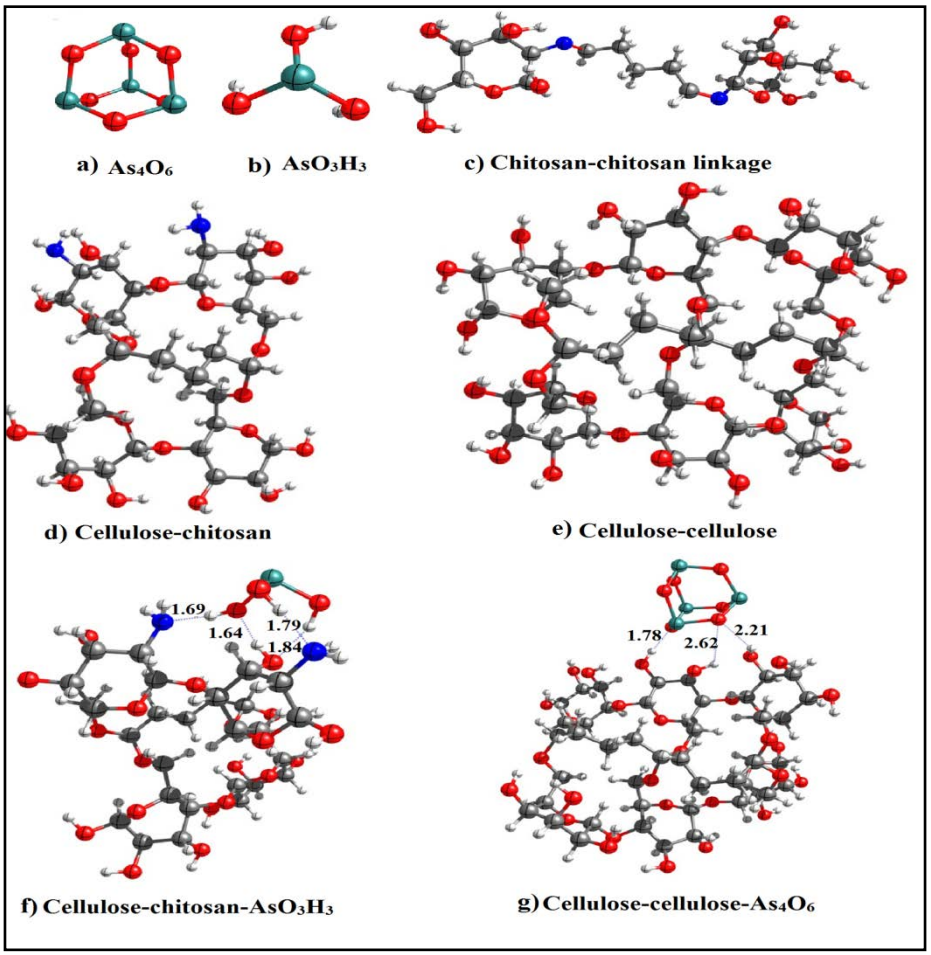


**Figure 3.6.2** Optimized geometries for different reactants and complexes formed with the polymers

The geometric parameters of final optimized structures are tabulated in table 3.6.2. The structures with their bond lengths marked are shown in Figure 3.6.2 (a-g). From table 3.6.2 it was observed that the complex *(f)* which was formed by sorption of

*(b)* on *(d)*, the O-H$^a$ bond near to the $NH_2$ group shortened after arsenic sorption, whereas, the length for other OH$^b$ bond remain unchanged. The N-H bond also shortened whereas, lengthening of C-N bond took place compared to the untreated polymeric system. The As-O as well as AsO-H bonds got elongated in complex *(f)*. This confirmed that the sorption of As(III) caused some changes in geometry of the complex, particularly, in those atoms where direct interactions occurred.

For complex *(g)*, which was formed by sorption of *(a)* on *(e)*, the O-H$^a$ bonds of the polymer which formed hydrogen bonding with the $As_4O_6$ cluster was lengthened but other bonds away from the cluster remained unchanged. Similar lengths in case of O-C-O were found for the pure as well as the adsorbed complex. Lengthening of As-O$^e$ bond of the lower ring of $As_4O_6$ was observed, other As-O$^f$ bonds away from the polymer remain unchanged.

**Table 3.6.2** Table showing the geometrical parameters where *d* is bond length in Å.

| Geometric parameters | Values | Geometric parameters | Values |
|---|---|---|---|
| ***Complex (d)*** | | ***Complex (f)*** | |
| $d_{O-H}$ | 1.035-1.040$^a$ | $d_{O-H}$ | 1.008$^a$ |
| | 0.986-0.995$^b$ | | 0.970-0.985$^b$ |
| $d_{N-H}$ | 1.024-1.048 | $d_{N-H}$ | 1.022-1.023 |
| $d_{C-N}$ | 1.452-1.454 | $d_{C-N}$ | 1.460-1.468 |
| $d_{C-O}$ | 1.400-1.448 | $d_{C-O}$ | 1.422-1.437 |
| ***Complex (b)*** | | $d_{As-O}$ | 1.831-1.881 |
| $d_{As-O}$ | 1.838-1.858 | $d_{AsO-H}$ | 0.993-1.020 |
| $d_{AsO-H}$ | 0.975-0.978 | $d_{AsOH\cdots NH}$ | 1.688-1.794 |
| | | $d_{OH\cdots OHAs}$ | 1.693-1.837 |
| ***Complex (e)*** | | ***Complex (g)*** | |

| | | | |
|---|---|---|---|
| $d_{O-H}$ | 0.970-0.985 | $d_{O-H}$ | 0.981-0.992[c] |
| | | | 0.975-0.986[d] |
| $d_{C-O}$ | 1.396-1.445 | $d_{C-O}$ | 1.387-1.452 |
| ***Complex (a)*** | | $d_{As-O}$ | 1.856-1.859[e] |
| $d_{As-O}$ | 1.850-1.851 | | 1.842-1.850[f] |
| | | $d_{OH\cdots OAs}$ | 2.210-2.617 |
| | | $d_{As\cdots OH}$ | 2.860 |

*3.6.1.1.2 TGA Analysis*

Thermograms of CT, WHRP, CARB and CTRP were shown in Figure 3.6.3. In all the thermograms, the initial weight loss at around 100 ˚C was due to evaporation of moisture. The major weight loss occurred in the range 230-360 ˚C. The weight loss was least for the composite followed by chitosan and WHRP. It was highest for the blend.

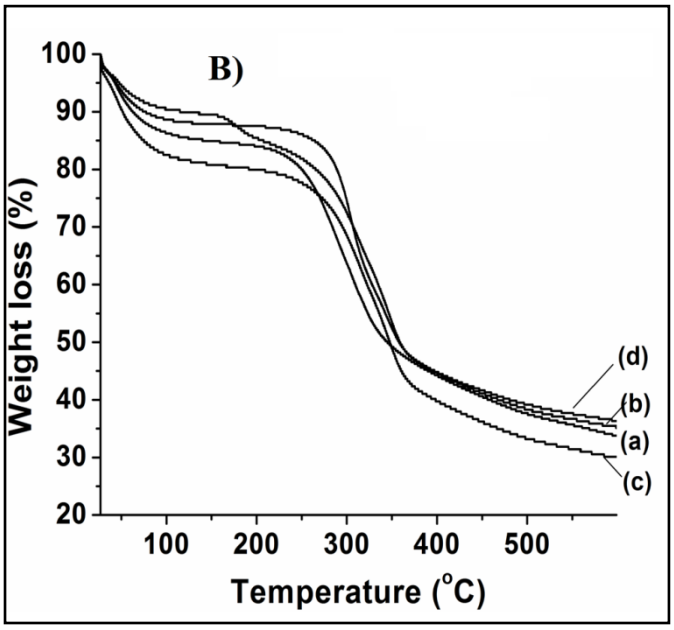


**Figure 3.6.3** TGA thermograms of a) CT b)WHRP c) CTRB d) CT:RP/1:2

Percentage of char was more in CTRP compared to CARB, CT or WHRP. For the physical blend, the degradation temperature was shifted to low temperature as compared to the individual materials. Cellulose and chitosan contain large amount of

intra-and intermolecular hydrogen bonds in their structure [21]. These intra and intermolecular hydrogen bonds may be weakened during the physical blending and as a result degradation took place at lower temperature. Similar explanations were given by Cai and Kim [22], when experimented with different variations of chitosan w.r.t. cellulose. In contrast to this, the two materials when crosslinked with glutaraldehyde showed significant improvement in thermal stability due to functioning of extensive chemical bonding among different polymeric chains.

*3.6.1.1.3 SEM-EDX Analysis*

Figure 3.6.4 C (a-d) represents the SEM images of CT, WHRP, CTRP and arsenic adsorbed CTRP composite, respectively. In the micrograph for CT (a), a non porous, smooth surface was observed having numbers of crystallites which resembles to those of results reported by Kumar and koh [23]. In contrast to this, SEM image of the WHRP showed numbers of fibriller crystallites. These structures were mainly due to the cellulosic component of the WHRP. But in the combined system, further changes in the surface morphology was observed as compared to the WHRP. Although some irregularity in the structure was observed after incorporation of WHRP in CT, the new structure showed very good interaction among component materials which was further supported by the degradation pattern in TGA study.

The surface of arsenic adsorbed CTRP composite (d) appeared smooth which might be due to sorption of arsenic on the material.

EDX spectrum of CTRP [spectrum-e] showed the presence of carbon, nitrogen and oxygen which are the major elements of glucose and glucose amine of chitosan and cellulose of the components of the composite material. Along with those, metals like calcium, iron, etc., were also observed which may be attributed to WHRP unit [24]. The presence of arsenic along with other metals in the EDX spectrum of CTRP-As [spectrum-f] indicated succesful adsorption of arsenic on the surface of the composite system.

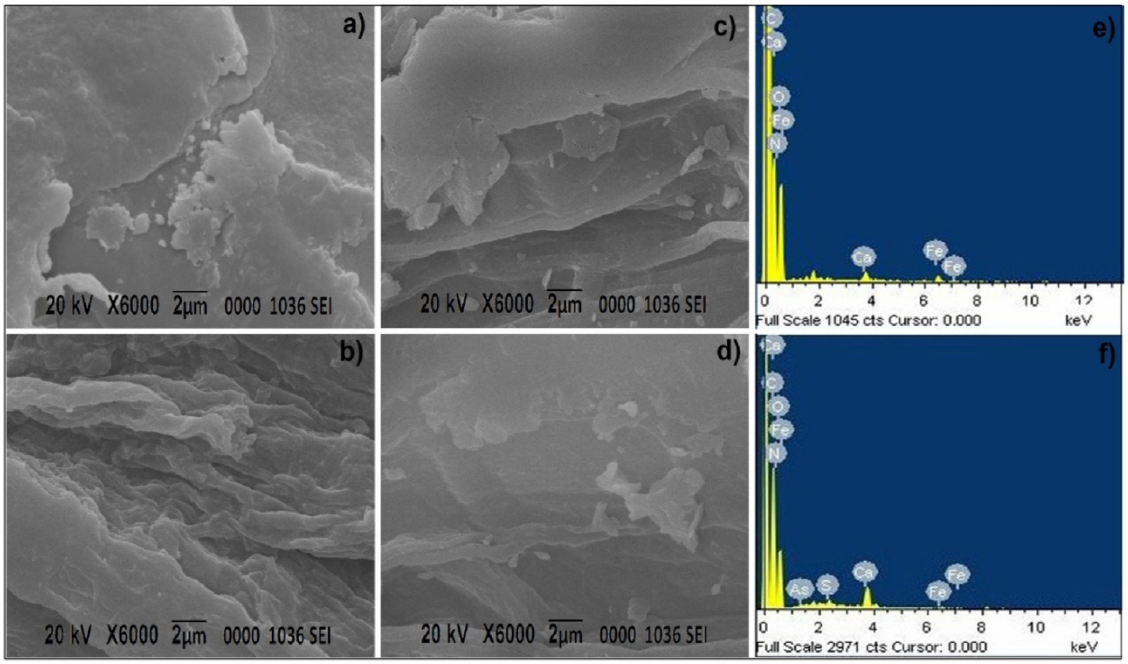


**Figure 3.6.4** SEM images of a) CT b) WHRP c) CTRP d) CTRP-As and EDX spectra of e) CTRP f) CTRP-As

### *3.6.1.2 Batch Adsorption Experiment*

#### *3.6.1.2.1 Effect of Material Dose and Composition on Removal Efficiency*

To study the effect of dose and composition on removal rate of arsenic, the arsenic solution (0.4 mg/L) was treated with different doses of material and stirred at about 160 rpm for 5 h. The test was carried out for different materials having different compositions of chitosan and WHRP viz. CT:RP/1:0, CT:RP/0:1, CT:RP/1:4, CT:RP/1:2, CT:RP/1:1, respectively, and material dose was varied from 1-6 g/L. The removal rate increased with increase in material dose and sorption capacities of different materials were found to be different as shown in [Figure 3.6.5]. The sorption efficiency was highest for glutaraldehyde crosslinked chitosan and least for the WHRP. The overall removal rate of CT:RP/1:2 and CT:RP/1:1 were comparable to that of chitosan alone. The turbidity of the solution that persists after treatment with CT/RP was negligible (~1.6 NTU) compared to that of WHRP alone (25NTU). Also, the composite materials showed similar removal efficiency as that of chitosan, although the amount of chitosan in the former is significantly less. Similarly, to get similar efficacy, the amount of composites required was very less compared to that of WHRP alone.

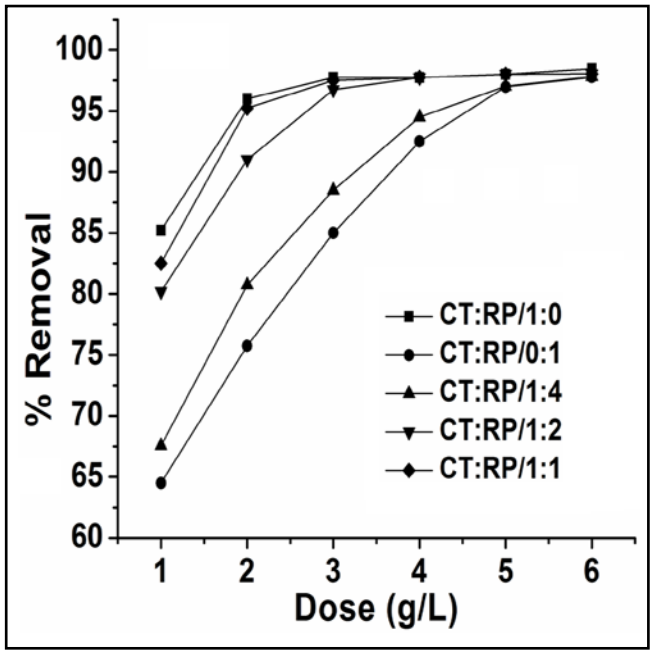


**Figure 3.6.5** Effect of a) material dose on removal rate of arsenic.

The enhanced efficacy of the composite system was due to synergistic effect of both the polymeric materials i.e., chitosan and WHRP present in the composite. During mixing of the two polymeric materials a number of inter and intramolecular H-bonding sites might get broken resulting into formation of a number of free active sites for sorption. The amount of material required for maximum removal of arsenic (arsenic solution under investigation) was found to be 3 g/L. By considering efficiency, turbidity due to the material and cost, the CT:RP/1:2 composite was selected for subsequent investigations.

A dose of 3 g/L of the chosen material found to be sufficient for bringing down the solution concentration below 10 µg/L. Beyond that dose, the removal efficiency was not so much significant. Therefore, a material dose of 3 g/L was taken for further study. With the increase in material dose, the number of active functional/or binding/and surface sites increased and hence the sorption increased. Influence of further increase in material dose was not so significant. Because of the presence of very small amount of As(III) ions in solution which might instantly attain equilibrium with the adsorbed As(III) ions present on the surface of the material.

*3.6.1.2.2 Effect of Treatment Time on Removal Efficiency*

Figure 3.6.6 shows the effect of treatment time on removal efficiency of As(III) (in the range of 30-240 min). 100 mL of As(III) solutions (0.4 mg/L) were taken in eight conical flasks each containing 3g of CT:RP/1:2 per liter of solution. These mixtures were allowed to agitate at a speed of 160 rpm and each of the conical flasks was taken out from the shaker at a regular interval of half an hour. The supernatants were centrifuged, filtered and aliquots were analyzed for As(III).

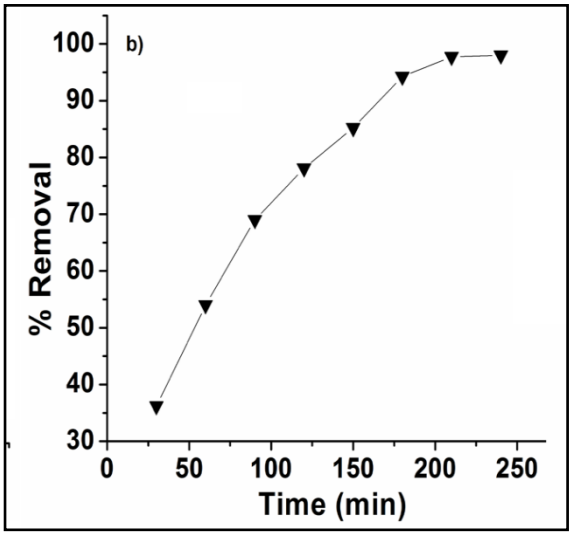


**Figure 3.6.6** Effect of treatment time on removal rate of Arsenic

With the increase in agitation time, the equilibrium adsorption capacity of the material increased upto a certain time (210 min) beyond that it remained almost constant. Increase in agitation time allowed more functional sites to bind with As(III) ions. But sorption being a reversible process, after certain time, equilibrium was established between adsorbed arsenic on the material and arsenic present in solution.

*3.6.1.2.3 Effect of Initial Ion Concentration*

Effect of initial ion concentration on adsorption capacity/removal rate of arsenic was studied in the concentration range of 0.2-0.5 mg/L for a material dose of 3g/L for 210 min. Figure 3.6.7 shows the variation of adsorption capacity/removal rate of arsenic with change in initial arsenic concentration. It was observed that the equilibrium sorption capacity (mg/g) was increased with the increase in initial arsenic concentrations while percent removal decreased. The increase in sorption capacity was due to increase in concentration gradient of arsenic at interface of adsorbent and arsenic solution which resulted stronger adsorption driving force in the concentrated solution. At lower concentration, ration of available active sites of sorbent surface and arsenic

concentration is high; hence sorption becomes independent of initial ion concentration. It means that active sites adsorb most of the arsenic species in solution. At higher concentration the active sites to arsenic ration is less, decreasing removal percent. Moreover, due to increase in arsenic concentration, the equilibrium between arsenic ion present in solution and adsorbent surface was delayed

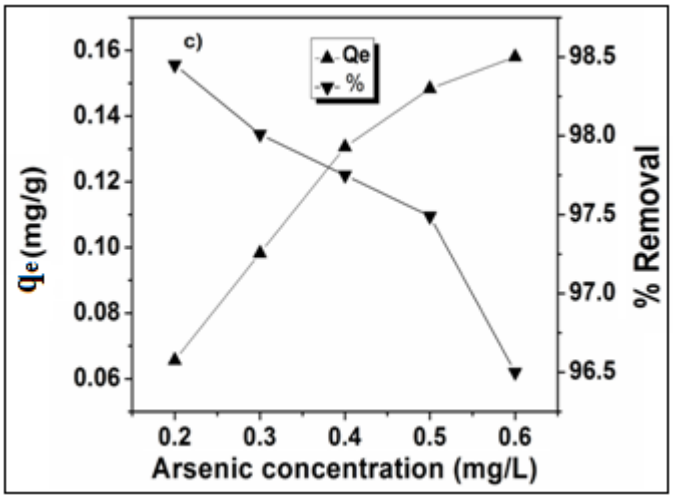


**Figure 3.6.7** Effect of initial ion concentration on removal rate and removal capacity of arsenic

### *3.6.1.3 Kinetics of Adsorption*

Figure 3.6.8 (A) represents the variation of $q_t$ (mg/g) of arsenic over time for four different initial arsenic ion concentrations viz. 0.2, 0.3, 0.4 and 0.5 mg/L. The $q_t$ values were found to increase with increase in initial arsenic concentrations. This might be due to high concentration gradient of arsenic at the interface of sorbent and solution. The plots of $\log(q_e - q_t)$ vs t and $t/ q_t$ vs t as per equation (2) and (3) gave straight lines from which the different kinetic parameters for pseudo first order and pseudo second order were evaluated and given in Table 3.6.3.

The correlation coefficients ($R^2$) were computed for the all models and values are shown in Table 3.6.3. The curve for pseudo second order kinetics exhibited higher correlation co-efficient (~0.99) compared to the other models indicating the preference for a monolayer chemisorptions pattern.

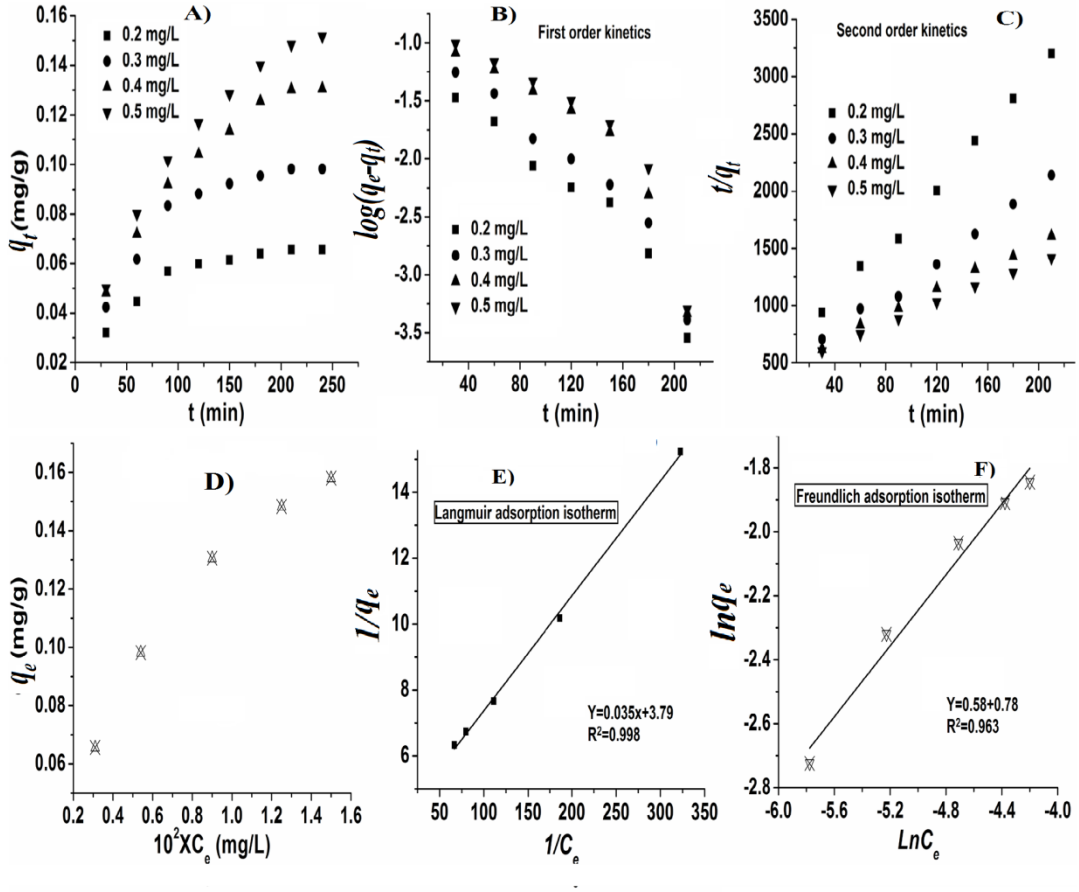


**Figure 3.6.8** (a-c) $Q_t$ vs t curve and kinetic models, (d-f) Isotherm models for sorption of As(III) on CT:RP/1:2

**Table 3.6.3** Parameters for different kinetic models for sorption of Arsenic on CT:RP/1:2

| $C_o$ (mg/L) | First order kinetic model | | | | Second order kinetic model | | | |
|---|---|---|---|---|---|---|---|---|
| | $Q_e$ *(exp)* *mg/g* | $K_1$ x $10^{-2}$ ($min^{-1}$) | $Q_e$ (mg/g) | $R^2$ | $K_2$ x $10^{-2}$ $gmg^{-1}min^{-1}$ | $Q_e$ *(Cal)* (mg/g) | $hx10^{-3}$ | $R^2$ |
| 0.2 | 0.066 | 2.41 | 0.087 | 0.926 | 29.7 | 0.079 | 1.87 | 0.995 |
| 0.3 | 0.098 | 2.47 | 0.156 | 0.920 | 14.2 | 0.126 | 2.25 | 0.991 |
| 0.4 | 0.131 | 2.53 | 0.319 | 0.808 | 5.86 | 0.186 | 2.04 | 0.995 |
| 0.5 | 0.143 | 2.49 | 0.371 | 0.769 | 4.30 | 0.221 | 2.10 | 0.998 |

### *3.6.1.4 Adsorption Isotherm*

Figure 3.6.9 D) shows the growth of adsorbed amount ($q_e$) of arsenic (mg/g) at equilibrium over the surface CA/10RP against increase in equilibrium concentrations ($C_e$). To establish the influence of arsenic concentration on the adsorption process, the equilibrium data was analyzed by linear forms of Langmuir and Freundlich models and are shown in table 3.6.4.

$R_L$ value (0.64) showed the suitability of Langmuir model for the sorption. Also, $q_e$ vs $C_e$ showed linearity of the graph. Freundlich parameters $R^2$ and n values as shown in table 3.6.4 also indicated good fitting of sorption data with the model.

**Table 3.6.4** Values of different isotherm parameters for sorption of Arsenic

| Isotherm models | Parameters | Value |
|---|---|---|
| Langmuir | $Q_\circ$ (mg/g) | 7.11 |
| | B | 4.03 |
| | $R_L$ | 0.64 |
| | $R^2$ | 0.998 |
| Freundlich | $k_f$ (mg/g) | 1.69 |
| | N | 1.80 |
| | $R^2$ | 0.963 |

$R^2$ values for both Langmuir and Freundlich models showed good co-relations of the data and the sorption could be reasonably explained by the models under consideration. $R^2$ values for Langmuir model was higher than that of Freundlich model. Thus, the preferential order for sorption for the applied models is as follows- Langmuir > Freundlich.

**References**

[1] Ibrahim, H. S., Ammar, N. S., Soylak, M. and Ibrahim, M. Removal of Cd(II) and Pb(II) from aqueous solution using dried water hyacinth as a biosorbent. *Spectrochimica Acta Part A: Molecular and Biomolecular Spectroscopy*, 96: 413-420, 2012.

[2] Tiwari, S., Dixit, S. and Verma, N. An Effective Means of Biofiltration of Heavy Metal Contaminated Water Bodies Using Aquatic Weed Eichhornia *crassipes. Environmental Monitoring and Assessment*, 129:253-256, 2007.

[3] Elfeky, S. A., Imam, H. and Alsherbini, A. A. Bio-absorption of Ni and Cd on Eichhornia crassipes root thin film. *Environmental Science Pollution Research*, 20:8220-8226, 2013.

[4] Verma, V. K., Tewari, S. and Rai, J. P. N. Ion exchange during heavy metal bio-sorption from aqueous solution by dried biomass of macrophytes. *Bioresource Technology*, 99:1932-1938, 2008.

[5] Srivastava, A. and Gopal, P. Kinetic Study of Arsenite Adsorption onto Dried Hyacinth Root Powder. *Research Journal of Chemical Sciences*, 5:41-48, 2015.

[6] Shaban, W., Rmalli, A., Harrington, C. F., Ayub M. and Haris, P. I. A biomaterial based approach for arsenic removal from water. *Journal of Environmental Monitoring*, 7:279-282, 2005.

[7] Reddya, N., and Yang, Y. Citric acid cross-linking of starch films. *Food Chemistry*, 118:702-711, 2010.

[8] Menzel, C., Olsson, E., Plivelic, T. S., Andersson, R., Johansson, C. and Kuktaite, R. Molecular structure of citric acid cross-linked starch films. *Carbohydrate Polymer*, 96:270-276, 2013.

[9] Okeil, A. A. Citric Acid Crosslinking of Cellulose Using $TiO_2$ Catalyst by Pad-Dry-Cure Method. *Polymer-Plastics Technology and Engineering*, 47:174-179: 2008.

[10] Xu, Z., Li, Q., Gao, S. and Shang, J. K. As(III) removal by hydrous titanium dioxide prepared from one-step hydrolysis of aqueous $TiCl_4$ solution. *Water Research*, 44:5713-5721, 2010.

[11] Zheng, J.-C., Feng, H.-M., Lam, M. H.-W., Lam, P. K.-S., Ding, Y.-W. and Yu, H.-Q. Removal of Cu(II) in aqueous media by biosorption using water hyacinth roots as a biosorbent material. *Journal of Hazardous Material*, 171:780-785, 2009.

[12] Southichak, B., Nakano, K., Nomura, M., Chiba, N. and Nishimura, O. Phragmites aus-tralis: a novel biosorbent for the removal of heavy metals from aqueous solution. *Water Research*, 40:2295-2302, 2006.

[13] Water, S. and World Health Organization, (2006). Guidelines for drinking-water quality [electronic resource]: incorporating first addendum. Vol. 1, Recommendations. Wegelin, M., Gechter, D., Hug, S., Mahmud, A. & Motaleb, A. (2000). SORAS-a simple arsenic removal process. In WEDC CONFERENCE, 26, 255-258.

[14] Kumar, M. and Puri, A. A review of permissible limits of drinking water. *Indian Journal of Occupational and Environmental Medicine*, 16:40, 2012.

[15] Wegelin, M., Gechter, D., Hug, S., Mahmud, A. and Motaleb, A. SORAS-a simple arsenic removal process. In WEDC CONFERENCE, 26:255-258, 2000.

[16] M.R. Gandhi, N. Viswanathan, S. Meenakshi, Preparation and application of alumina/chitosan biocomposite, *International Journal of Biological Macromolecule*, 47:146-154, 2010.

[17] Sashiwa, H. and Aiba, S. I. Chemically modified chitin and chitosan as biomaterials. *Progress in Polymer Science*, 29:887-908, 2004.

[18] Duan, J., Han, C., Liu, L., Jiang, J., Li, J., Li, Y. and Guan, C. Binding cellulose and chitosan via intermolecular inclusion interaction: synthesis and characterisation of gel. *Journal of Spectroscopy*, 2015, 2015.

[19] Iman, M., Bania, K. K. and Maji, T. K. Green jute-based cross-linked soy flour nanocomposites reinforced with cellulose whiskers and nanoclay. *Industrial & Engineering Chemistry Research*, 52:6969-6983, 2013.

[20] Nayak, P. S. and Singh, B. K. Instrumental characterization of clay by XRF, XRD and FTIR. *Bulletin of Materials Science*, 30:235-238, 2007.

[21] Prashanth, K. H. and Tharanathan, R. N. Chitin/chitosan: modifications and their unlimited application potential—an overview. *Trends in Food Science & Technology*, 18:117-131, 2007.

[22] Cai, Z. and Kim, J. Characterization and electromechanical performance of cellulose–chitosan blend electro-active paper. *Smart Materials and Structures*, 17:035028, 2008.

[23] Kumar, S. and Koh, J. Physiochemical, optical and biological activity of chitosan-chromone derivative for biomedical applications. *International Journal of Molecular Sciences*, 13:6102-6116, 2012.

[24] Srivastava, S., Agrawal, S. B. and Mondal, M. K. A review on progress of heavy metal removal using adsorbents of microbial and plant origin. *Environmental Science and Pollution Research*, 22:15386-15415, 2015.